STUDY OF THE SEISMIC BEHAVIOR OF STEEL PLATE SHEAR WALLS WITH COUPLING THROUGH ANALYSIS AND TESTING OF A SMALL-SCALE MODEL

BY

ALVARO A. QUINONEZ

THESIS

Submitted in partial fulfillment of the requirements
for the degree of Master of Science in Civil Engineering
in the Graduate College of the
University of Illinois at Urbana-Champaign, 2013

Urbana, Illinois

Adviser:

Assistant Professor Larry A. Fahnestock

ABSTRACT

As part of a multi-institutional study of seismic analysis, behavior, design and performance of the steel plate shear wall with coupling (SPSW-WC) system, an integrated analytical, numerical, and experimental study was conducted on a small-scale, three-story SPSW-WC specimen. The small-scale specimen's design was based on the scaling down of one of the large-scale specimens that will be tested as part of the SPSW-WC program at the University of Illinois. The concepts of dimensional analysis and similitude were used to scale down the large-scale specimen. Analytical and numerical models were used to estimate the small-scale specimen's ultimate strength and study its behavior under lateral loads. The experimental study consisted of a cyclic displacement loading test on the small-scale specimen. The system's behavior was stable for much of the test, and the specimen was able to undergo large roof displacements. The analytical, numerical, and experimental results are presented and discussed.

ACKNOWLEDGEMENTS

I am very grateful for the invaluable research, academic, and career advice offered to me by my advisor Dr. Larry A. Fahnestock during the course of my master's program. I am also thankful for the opportunity he offered me to work on this research project. He is a great mentor and teacher, and I have gained much knowledge from his experience.

I thank my parents for all their love and support throughout my journey in graduate school. I could always count on them for advice during the tough times. The strong values they have instilled in me have helped me to achieve the academic, research, and career goals that I have set for myself, and they will continue to do so in the future.

The friends I made at the University of Illinois helped to make graduate school an exciting experience. I enjoyed our exchange of ideas as well as the downtime we spent together outside of the classroom, laboratory, and office.

I thank my research partner Daniel J. Borello for sharing his experience and knowledge, as well as for his help and input during the small-scale experiment. I also thank the team of enthusiastic undergraduate students who worked to instrument the small-scale specimen.

The personnel and students working at the Network for Earthquake Engineering Simulation facility at the University of Illinois also deserve recognition. They were a great source of help during the time spent preparing for testing in the laboratory. I also thank the great staff at the Newmark Structural Engineering Laboratory for all of their help in fabricating the small-scale specimen and other components of the project I worked on. In particular, I want to express my gratitude to Tim Prunkard, Darold Marrow, and Don Marrow for all the time spent going over fabrication drawings and for their invaluable advice.

Thanks also go to the project collaborators at the University of Washington: Dr. Jeffrey W. Berman, Dr. Laura Lowes, and graduate students Patricia Clayton, Mohammad Malakoutian, and David Webster.

Finally, I am very grateful for the funding I received through the National Science Foundation Graduate Research Fellowship. This material is based upon work supported by the National Science Foundation under Grant No. DGE-1144245.

Any findings and conclusions in this thesis are those of the author and do not reflect the views of the National Science Foundation.

TABLE OF CONTENTS

CHAPTER 1

INTRODUCTION

1.1 Steel Plate Shear Walls

Steel plate shear walls (SPW) are an effective lateral force resisting system used to resist wind or earthquake loads on buildings. SPWs have been used in the United States, Japan, Canada, and Mexico (Bruneau and Sabelli 2006). Of particular interest is their performance under seismic loads. As shown in Figure 1.1, a SPW consists of columns—referred to as Vertical Boundary Elements (VBE)—and beams—referred to as Horizontal Boundary Elements (HBEs). As their names imply, VBEs and HBEs are boundary elements for slender steel web (infill) plates. The web plates are typically welded to the surrounding HBEs and VBEs. In a building, SPWs are placed in one or multiple bays over the building's height (Bruneau and Sabelli 2006). The beam-to-column connections may be simple connections (which lack the stiffness to prevent relative rotation between the HBE and VBE at the joint), or moment-resisting connections (also known as fully-restrained connections, which are assumed to have sufficient stiffness such that relative rotation between boundary elements at a joint is prevented) (Bruneau and Sabelli 2006).

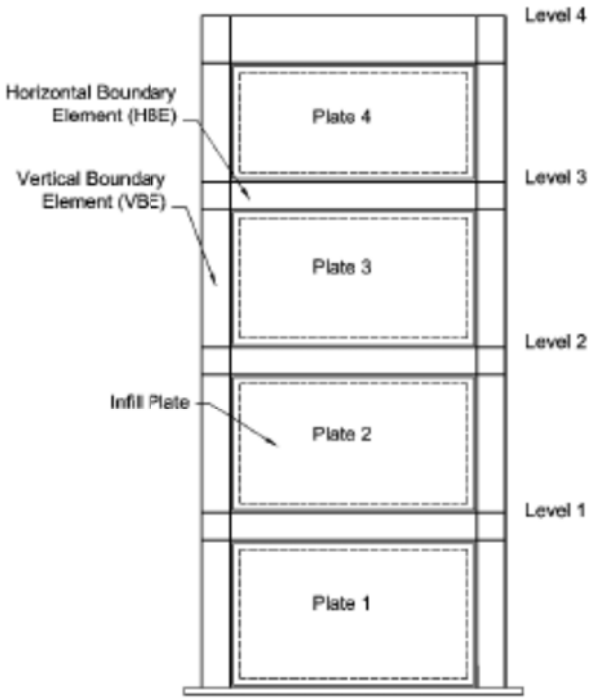

Figure 1.1 SPW Configuration (Bruneau et al. 2005)

Some of the main SPW configurations are presented in Figure 1.2. The main configurations are (Bruneau and Sabelli 2006):

- The conventional configuration with unstiffened and slender steel web plates and a low web plate shear buckling strength. Post-buckling tension field action is used to help resist lateral forces.
- Composite and non-composite systems with stiffened web plates. Composite systems may use a concrete filled tube on one or both sides of the web plates in addition to horizontal and vertical web plate stiffeners. Non-composite systems only use web plate stiffeners. Partially or fully stiffened web plates provide greater shear buckling strength. Partially stiffened web plates help resist lateral forces through a combination of shear buckling strength and post-buckling tension-field action. Fully stiffened web plates help resist lateral forces using only their shear buckling strength.

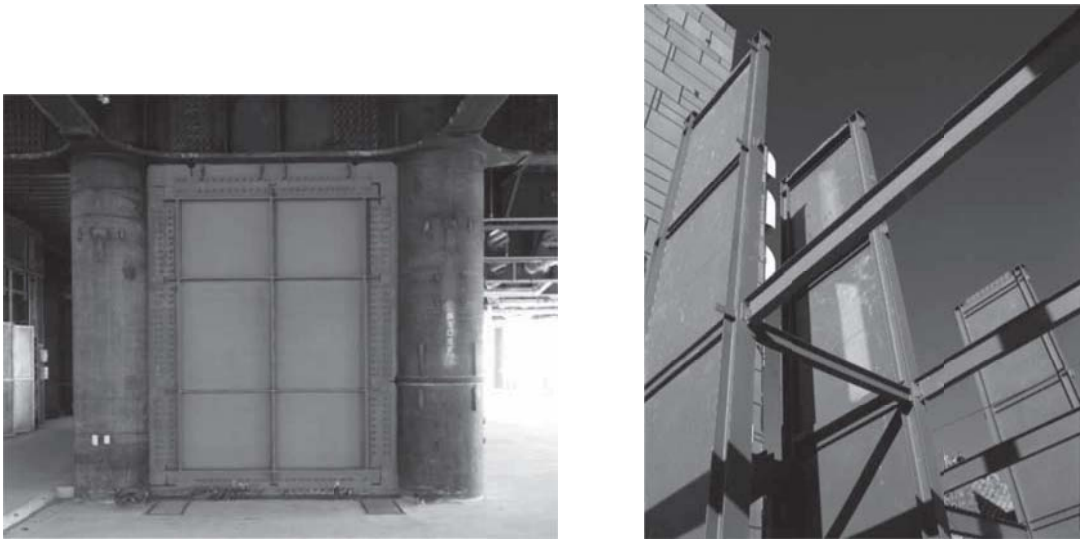

(a) **(b)**

Figure 1.2 (a) Composite SPW with Vertical and Horizontal Web Plate Stiffeners, (b) SPW with Unstiffened Web Plates (Bruneau and Sabelli 2006)

Stiffening the web plates does not significantly increase the strength or stiffness of the SPW, and it may increase construction costs as well as wall thickness (Bruneau and Sabelli 2006). Partly because of these drawbacks, the general practice in the United States has been to design SPWs with unstiffened, slender web plates.

1.2 Special Plate Shear Walls

The Special Plate Shear Wall (SPSW) is based on the SPW configuration with slender and unstiffened web plates. Moment-resisting connections between the boundary elements are used (Bruneau et al. 2005). Provisions for the design of SPSWs were introduced in the United States in the 2005 American Institute of Steel Construction (AISC) Seismic Provisions for Structural Steel Buildings and the 2005 American Society of Civil Engineers (ASCE) 7-05 Minimum Design Loads for Buildings and Other Structures.

Before the 1980s, SPSW were designed for the limit state of out-of-plane buckling of the web plates (Bruneau et al. 2005). Thus, designers heavily stiffened the web plates, which caused the SPSW to lose its competitive cost relative to reinforced concrete shear walls (Bruneau et al. 2005). However, SPSW research conducted in Canada during the 1980s and in the United States during the 1990s demonstrated the benefits to system strength, ductility, and energy dissipation resulting from the use of unstiffened and slender web plates (Bruneau et al. 2005).

1.3 Benefits of Special Plate Shear Walls

SPSWs have several advantages compared to reinforced concrete shear walls and other steel lateral force resisting systems. The advantages are evident in required building floor-plan area, constructability, and cost (Bruneau and Sabelli 2006):

- Compared to a reinforced concrete shear wall, SPSW maximizes the use of the floor-plan area because of its relatively smaller thickness.
- SPSWs may help to significantly reduce a building's weight and construction time relative to reinforced concrete shear walls.
- Relative to steel braced frames, SPSWs can be designed to provide an equal amount of strength and stiffness, while using an amount of floor-plan area that is equivalent or less.

SPSWs provide robust seismic performance under moderate and severe seismic loads due to their significant strength, stiffness, and ductility (Bruneau and Sabelli 2006):

- The post-buckling strength resulting from tension field action in the web plates provides significant strength to the system.

- Rigid HBE-to-VBE connections help to increase the system's stiffness.
- Web plate ductility helps the system to dissipate energy under severe seismic loads.

1.4 Steel Plate Shear Wall with Coupling

The Steel Plate Shear Wall with Coupling (SPSW-WC) is a natural extension of the SPSW configuration. As shown in Figure 1.3, this configuration consists of two SPSWs placed adjacent to each other and linked at the floor levels by coupling beams (CB). The VBEs of each wall pier are categorized as an internal VBE (IVBE) or external VBE (EVBE) because of the different demands on each VBE, which allow a designer to specify structural shapes of different sizes for the IVBE and EVBE.

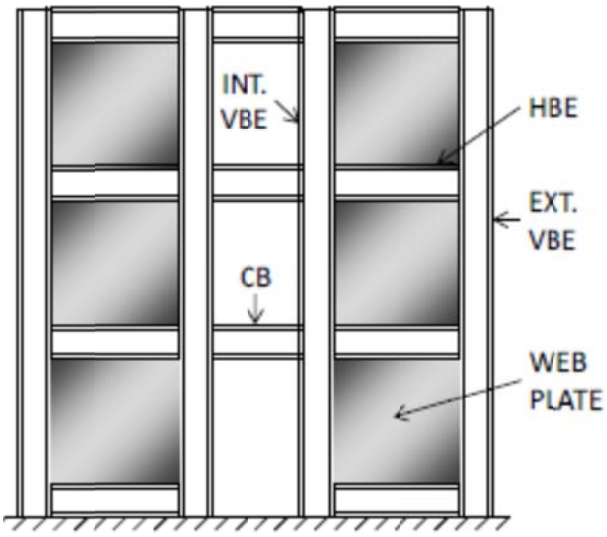

Figure 1.3 Elevation of a SPSW-WC (Borello and Fahnestock 2011)

SPSW-WC systems have the potential to provide additional benefits beyond the basic SPSW configuration. For example, when architectural requirements dictate that a building's lateral force resisting system must be placed around the core, two SPSWs may be placed adjacently to allow for openings in the core (Borello and Fahnestock 2012a). In addition, because SPSWs become uneconomical and impractical for large web plate length-to-height (L/h) aspect ratios (AISC 2010), two adjacent SPSWs may be placed in one bay of the building. The previous

edition of the AISC Seismic Provisions (AISC 2005) placed an upper limit of 2.5 on the L/h aspect ratio due to the lack of experimental data above L/h = 2.0, but this is no longer deemed necessary since economical designs will not be in this range. Thus, adjacent SPSWs provide a natural opportunity to improve efficiency and performance by introducing coupling to create a SPSW-WC. Analytical and numerical studies (Borello and Fahnestock 2012a, 2012b) have shown that the SPSW-WC configuration reduces steel weight and seismic response when compared to a comparable pair of uncoupled walls. These initial results indicate the promise of the system and the potential for its relatively easy adoption and implementation.

Despite the evident benefits of the SPSW-WC system, few investigations of the system have been conducted. As discussed in Chapter 2, the only experimental studies of coupled SPSWs have been conducted by Zhao and Astaneh-Asl (2004), Lin et al. (2010), and Li et al. (2011). However, results from these tests are not applicable to SPSW-WC in general, so a comprehensive analytical, numerical and experimental study is warranted.

1.5 Steel Plate Shear Wall with Coupling Research Program

To fill the current knowledge gap related to seismic analysis, behavior, design and performance of SPSW-WC, an integrated analytical, numerical and experimental research program is being conducted at the University of Illinois at Urbana-Champaign. This project is part of a larger research project on SPSWs sponsored by the National Science Foundation through the George E. Brown, Jr. Network for Earthquake Engineering Simulation (NEES).

A design procedure that is based on current code provisions for SPSWs has been developed and evaluated using nonlinear response history analysis (Borello and Fahnestock 2011). To evaluate the design procedure, a total of fourteen building prototypes were designed (Borello and Fahnestock 2012b).

For the SPSW-WC study, the prototype buildings were designed using capacity design procedures based on the current state-of-practice for SPSWs (Borello and Fahnestock 2012b). Numerical models were developed and validated, and they were used in static pushover analyses and earthquake response history analyses (Borello and Fahnestock 2012b). SPSW-WC behavior and the adequacy of the design procedure will be studied and evaluated through laboratory tests on two large-scale SPSW-WC specimens.

1.5.1 Large-Scale Experiments

As part of the SPSW-WC study, laboratory tests will be conducted on two approximately half-scale (0.43 scale) specimens (Borello and Fahnestock 2011). The tests will be conducted in the NEES Multi-Axial Full Scale Sub-Structured Testing & Simulation (MUST-SIM) laboratory at the University of Illinois at Urbana-Champaign. One of the unique features of the MUST-SIM facility is the ability to subject large-scale structural systems or subassemblies to complex loading and deformation states (NEES @ Illinois 2013). This is possible because of the facility's three loading and boundary condition boxes (LBCB). Each LBCB has six degrees of freedom (DOF) that may be controlled to apply complex load and boundary conditions on the specimen being tested (NEES @ Illinois 2013).

Both specimens are a three-story subassembly of a six-story prototype frame used for numerical studies (Borello and Fahnestock 2011). To prevent the LBCBs from constraining the top CB, it was omitted from the specimen designs (Borello and Fahnestock 2011). Of the two SPSW-WC specimens that will be tested, one has flexural yielding dominated CBs (FLEX) and the other has intermediate flexural/shear yielding dominated CBs (INT). Each specimen is approximately 20 ft. in height. For the second and third stories of each specimen, the pier width and height are 4 ft.–9 in. and 5 ft.–7 in., respectively. The pier width and height of the first story are 4 ft.-9 in. and 7 ft.-9 in., respectively, for both specimens.

During each test, each pier of the SPSW-WC will be loaded by an LBCB. The IVBE and EVBE base plates and the bottom HBE will be bolted into a plate that will be pretensioned to the facility's strong floor (Borello and Fahnestock 2011). The IVBE and EVBE top plates and the HBE in each pier will connect to steel adapter plates, which will connect to the LBCBs. To brace the system against global out-of-plane instability and represent the story bracing in an actual building provided by the lateral force resisting system running perpendicular to the SPSW-WC, a bracing system was designed to brace the specimens at the second and third story beam-to-column connections. Figure 1.4 shows the experimental set-up.

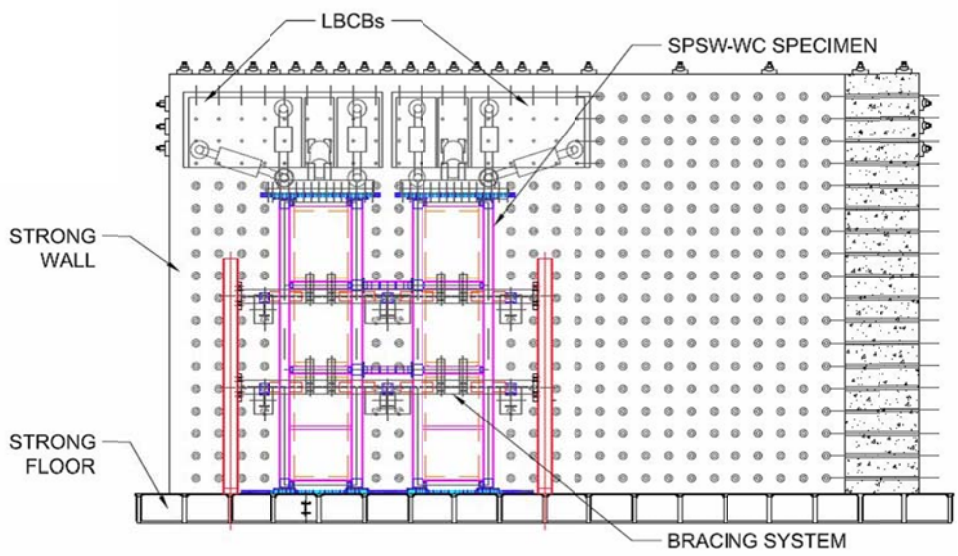

Figure 1.4 Large Scale Experimental Set-Up in MUST-SIM Facility

The control algorithms to be used during testing are based on the prototype SAC buildings. SAC is the acronym for the partnership between the Structural Engineers Association of California, the Applied Technology Council, and the California Universities for Research in Earthquake Engineering formed to investigate the poor performance of welded, steel moment frame connections following the 1994 Northridge earthquake in California (FEMA 2000). Displacements and forces at the top of the third story in the prototype buildings for each SPSW-WC coupling pier under a pushover loading protocol were reduced to six-DOF (Borello and Fahnestock 2011). Mathematical expressions representing the relationship among the displacement and force demands form the basis of the control algorithms (Borello and Fahnestock 2011). The algorithms were validated on analytical models of the test specimens by comparing their global and local behavior to that of the bottom three stories of the prototype buildings (Borello and Fahnestock 2011). To further validate the control algorithms, tests on the small-scale SPSW-WC model were conducted in the 1/5th scale NEES MUST-SIM facility.

1.5.2 Small-Scale Steel Plate Shear Wall with Coupling Specimen

A small-scale SPSW-WC specimen was designed and tested as part of the SPSW-WC program at the University of Illinois. This specimen is scaled-down from the large scale SPSW-WC FLEX specimen. The test on the small-scale specimen was used to validate control

algorithms for the large scale tests, and to study the basic mechanisms of coupled wall behavior. This small-scale testing is the focus of this thesis.

1.6 Thesis Organization

This thesis describes the small-scale SPSW-WC analytical, numerical, and experimental models and results used to help provide an understanding of the mechanics of the proposed structural system under seismic loads. The following is a summary of the topics discussed in each chapter:

- Chapter 1: An overview of the conventional SPW and SPSW is provided. The reasons for investigating the behavior of SPSW-WC are discussed. In addition, the advantages of the SPSW-WC as compared to the SPSW are highlighted. Finally, an overview is given of the research program at the University of Illinois at Urbana-Champaign that is focused on understanding SPSW-WC behavior under seismic loads.
- Chapter 2: A review of experimental studies of small- and large-scale SPW, SPSW, and coupled SPSW specimens is provided. The existing literature on SPSW-WC analytical and numerical studies is also reviewed.
- Chapter 3: The design of the small-scale SPSW-WC specimen is discussed, including the process through which the large-scale FLEX specimen was scaled down.
- Chapter 4: An analytical model to determine the small-scale specimen's plastic strength is discussed. Flexural buckling capacities of the EVBEs and IVBEs are presented. Numerical models of the small-scale specimen developed in SAP2000 and the Open System for Earthquake Engineering Simulation (OpenSees) are also presented. Analytical and numerical results are presented and discussed.
- Chapter 5: The experimental set-up and data collection plan for the test on the small-scale specimen is discussed.
- Chapter 6: Experimental results are presented, discussed and compared to analytical and numerical results.
- Chapter 7: The research is summarized and conclusions regarding the results are made.

CHAPTER 2
LITERATURE REVIEW

This chapter provides selected background on previous experiments on small- and large-scale steel plate shear wall (SPW), special plate shear wall (SPSW), and coupled SPSW specimens. The small scale experiments are chosen to show that prior tests have helped to demonstrate the benefits of SPW and SPSW configurations, although no attempt has been made to conduct tests on a small-scale SPSW-WC specimen. Discussion of tests on large-scale SPSW and coupled SPSW configurations is provided to present the beneficial structural characteristics of these systems and highlight the need for further experimental investigations of SPSW-WC.

2.1 Previous Small-Scale Experiments on Steel Plate Shear Walls

During the early development of the SPW system, experiments were conducted on small-scale specimens to understand the system's behavior under lateral seismic loads. These tests provided invaluable insight into the strength, stiffness, ductility, and energy dissipation of the SPW.

Roberts and Ghomi (1991) conducted quasi-static cyclic load tests on six small-scale unstiffened plate shear panel specimens to determine their seismic performance. Three of the panels had a length of 300 mm (11.8 in.), and the other three panels were 450 mm (17.7 in.) long. All panels had a height of 300 mm (11.8 in.). Aluminum and steel panels were tested. The aluminum panels were 0.54 mm (0.0213 in.) thick, and the steel panels had thicknesses of 0.83 mm (0.033 in.) and 1.23 mm (0.0484 in.). All panels were subjected to a minimum of four load cycles. Experimental results showed that all the more slender panels provided good energy dissipation and ductility. The steel panels provided greater strength and dissipated more energy than the aluminum panels. These tests demonstrated the high ductility and energy dissipation capacity of slender and unstiffened steel web plates under cyclic lateral earthquake loads.

In a study by Caccese et al. (1993), the effects of web plate thickness and the stiffness of HBE-to-VBE connections on the seismic behavior of unstiffened thin SPW were studied. Cyclic tests were conducted on six 1:4 scale specimens: a moment resisting frame (MRF), three SPWs with moment-resisting HBE-to-VBE connections and different plate thicknesses, and two SPWs

with shear HBE-to-VBE connections and web plates with different thicknesses. The three-story SPW specimens had a bay width of 4 ft.–1 in. and a height of 9 ft.-5 in. The moment connection was made by fillet welding the complete HBE section to the VBE. The shear connection was made by fillet welding the web of the HBE to the VBE. All web plates were continuously welded to the flanges of the VBEs and HBEs. The different nominal web plate thicknesses that were studied were: 0.76 mm (0.0299 in.), 1.90 mm (0.0747 in.), and 2.66 mm (0.1046 in.). SPW specimens with the moment connections were fabricated with each of the web plate thicknesses, and the specimens with the shear connections were fabricated only with the first two web plate thicknesses. Cyclic displacements were applied to each specimen until a maximum top floor drift of two percent was achieved, and two displacement histories were applied to all specimens. If a specimen was not significantly damaged after the cyclic tests, it was pulled monotonically to the displacement limit of the load actuator. Results showed that the use of steel web plates in a moment-resisting frame significantly increased the system's stiffness, strength, and ability to absorb and dissipate energy. Results also indicated that the use of slender web plates was beneficial to SPW seismic performance because the web plates yielded under tension field action much earlier than the development of plastic hinges in the VBEs. For these cases, the formation of plastic hinges in the VBEs governed strength instead of inelastic buckling of the VBEs. The latter was observed in the SPW with the thickest web plates. Thus, the SPW with slender web plates can fully benefit from the post-buckling strength developed through tension field action.

2.2 Previous Large- and Full-Scale Experiments on Steel Plate Shear Walls, Special Plate Shear Walls and Coupled Special Plate Shear Walls

The first test on a large-scale multi-story SPW with slender and unstiffened web plates was conducted by Driver et al. (1998). The specimen that was tested was a four-story SPW with one bay, slender and unstiffened web plates, and moment-resisting connections between the boundary elements. The specimen's height and width were 7.4 m (approximately 24 ft.) and 3.4 m (approximately 11 ft.), respectively. Panel aspect ratios for the first to fourth stories were 0.59, 0.56, 0.56, and 0.48, respectively. The main goals of the investigation were to understand the behavior of individual elements and connections, and to understand the global system behavior in relation to energy dissipation and the contribution of the moment-resisting connections to

seismic performance. Gravity loads were applied to the top of each column for the duration of the test and lateral loads were applied at each floor level. A gradually increasing displacement loading history of 30 cycles was used. Test results indicated that the web plates helped the specimen to behave in a highly ductile manner, and provided significant strength through post-buckling tension-field action. The moment-resisting connections increased the amount of energy dissipated by the system. Additionally, uniform hysteresis loops indicated the very stable performance of the specimen throughout the test, and the use of web plates and moment-resisting connections provided redundancy to the specimen. Thus, it was concluded that this SPW configuration would perform robustly during an earthquake.

Zhao and Astaneh-Asl (2004) studied the seismic behavior of a coupled SPSW. The system that was studied was a pair of SPSWs connected at the floor levels by CBs, and the external VBEs were large concrete-filled tubes (CFT) with a diameter of 610 mm (2 ft.) and a thickness of 8 mm (5/16 in.). The system was designed by Magnusson Klemencic Associates for one of its building projects. Two half-scale specimens were fabricated and tested: a sub-assembly consisting of two floors of the prototype building, and a sub-assembly consisting of three floors of the building. The height of the web plates differed between both specimens. Taking advantage of the system's symmetry about its vertical center line, each specimen represented half of the actual system, and a roller was placed at the end of each CB to simulate boundary conditions in the actual structure. The HBEs were continuous through the internal VBE, and the HBE top and bottom flanges were welded to the internal VBE with full-penetration welds. The extensions of the HBEs past the internal VBE functioned as the CBs. The web plates in the two-story specimen had a thickness of 6 mm (1/4 in.), and the web plates in the three story specimen were 10 mm (3/8 in.) thick. The connections between the HBEs and the CFT were moment-resisting connections consisting of four deformed steel reinforcing bars fillet welded onto each HBE flange. The bars were embedded into the CFT to increase the system's ductility. During testing, an actuator was used to apply cyclic shear forces to the top of the specimens. The CFT columns in both specimens remained mainly elastic throughout the tests, with very little yielding observed. Each specimen achieved a maximum overall drift of 0.032, with maximum story drifts reaching values above 0.05. Also, neither specimen experienced a significant decrease in strength at large story drifts. Thus, adequate ductile behavior and energy dissipation were observed in the HBEs, web plates, and internal VBEs of the specimens. Failure initiated in both

specimens when the top CB completely fractured at the face of the internal VBE. However, these positive results are limited to the particular configuration that was tested and cannot be extended to understand the seismic behavior of SPSW-WC whose external VBEs are wide flange structural shapes and not CFTs. For a SPSW-WC, the seismic behavior and formation of the plastic mechanism is expected to be different. Moreover, in this study, only half of the actual sub-assembly in the structure was represented by each specimen under the assumption of symmetric system behavior. Tests on large-scale specimens that represent a complete sub-assembly are necessary to achieve a better understanding of global system seismic behavior.

In a research program at the National Center for Research on Earthquake Engineering (NCREE) in 2007, Li et al. (2011) conducted cyclic tests on four full-scale narrow SPSWs to verify a proposed VBE capacity design methodology that limits the formation of the plastic hinge to the VBE base. The panel aspect ratios of these specimens are similar to the ratios of the first story panels of the SPSW-WC piers to be tested at the University of Illinois. The two story specimens were narrow SPSWs 2.14 m (7 ft.-1/4 in.) wide and 6.5 m (21 ft.-4 in.) tall. All of the web plates had a thickness of 2.6 mm (0.10 in.), and their aspect ratios met the requirement of the *2005 AISC Seismic Provisions*. The VBE-to-HBE connections were all designed as welded moment connections. Three of the four specimens are discussed: specimens N and S were unstiffened SPSWs, and RS was the same as S but had two restrainers at each story on both sides of the web plates. Specimen N's design followed the proposed VBE design methodology. The HBEs and VBEs in specimen S were lighter than those in the other specimens, and the VBE design did not meet the requirements of the proposed design method. Although the final structural shapes chosen for specimen RS were the same as those in specimen S, specimen RS was fitted with restrainers on both sides of the web plates on each floor level to reduce the diagonal tension field's pull-in forces on the VBEs and HBEs. Hence, specimen RS satisfied the design criteria of the proposed VBE design method. The SPSW specimens were cyclically tested up to a roof drift of five percent. Results confirmed the predicted plastic hinge locations in the VBEs and demonstrated the adequate ductility of the SPSW system. As predicted, in the N and RS specimens, plastic hinges in the VBEs developed at the bases. In specimen S, it was observed that plastic hinges due to compressive loads on the VBEs developed away from the VBE ends. The results validated the proposed VBE design method, and demonstrated that SPSWs designed according to the methodology displayed adequate ductility and strength. Despite specimen S

developing a plastic hinge within the height of each VBE, it demonstrated adequate ductility and strength. This indicated that a more efficient SPSW design may be achieved by using lighter VBEs and HBEs. These results help to motivate SPSW-WC research, as the SPSW-WC configuration enables the use of lighter boundary elements compared to a conventional SPSW.

Li et al. (2011) also conducted tests on a reduced scale coupled steel plate shear wall (C-SPSW). Initially, a prototype six-story C-SPSW was designed based on the 2005 *AISC Seismic Provisions* and *AISC Specification for Structural Steel Buildings*. The bottom VBE of the system was designed based on a proposed column design methodology in which the plastic hinge is allowed to develop within the bottom quarter height of the VBE. As seen in the results of tests by Li et al. (2011) on specimen S described above, a VBE design in which plastic hinge formation is not restricted to the VBE base allows lighter VBEs to be used and results in a more economical system. The CBs in the C-SPSW were designed as eccentrically braced frame shear links. The specimen that was tested at NCREE was a 40% scale model of the bottom two and a half stories of the prototype C-SPSW. The specimen's web plates were 3.5 mm (0.14 in.) thick. A Reduced Beam Section (RBS) was used at the HBE ends, and the CB webs were stiffened to help meet rotational demands. To simulate the effects of the upper stories of the C-SPSW acting on the specimen, the specimen was subjected to cyclic lateral forces, cyclic overturning moments, and a constant gravity load. Roof drifts up to five percent were studied. Experimental results demonstrated the specimen's significant ductility and ability to dissipate energy. Because of the system's high ductility, there was no significant reduction in strength when five percent roof drift was applied. The plastic mechanism that developed in the C-SPSW consisted of shear hinges in the CBs, flexural hinges at the HBE ends, and flexural hinges at the VBE ends near the base. An interesting observation was that the plastic hinge in the external VBEs was wider and higher than the hinge in the inner VBEs. This difference may be explained by the fact that the axial demand (imposed by the HBE vertical end reaction and vertical component of web plate tension field) in the inner VBEs was less than in the external VBEs because the vertical end reactions in the CBs helped to counteract the axial demand in the inner VBEs (Li et al. 2011). Because of this, and based on the interaction between axial load and bending moment in the VBEs, the higher axial load in the external VBEs resulted in a relatively low flexural strength compared to that of the internal VBEs. The tests on different SPSW configurations conducted by

Li et al. (2011) demonstrated that using a more relaxed VBE design methodology would allow a SPSW and C-SPSW to be economical and perform adequately under lateral seismic loads.

In an experimental study conducted by Lin et al. (2010) at NCREE, a full-scale SPSW specimen was tested under pseudo-dynamic loads. This investigation involved two phases, and it was conducted to further demonstrate the efficiency and robustness of SPSWs under seismic loads. The full-scale specimen was designed using a capacity-based methodology wherein the web plates over the story height are assumed to yield due to tension-field action, and the VBEs and HBEs are designed to resist the demand imposed by yielding of the web plates. The specimen had a height of 8 m (26 ft.-3 in.) and a width of 4 m (13 ft.-1½ in.). The first and second story web plates had a thickness of 3 mm (0.1 in.) and 2 mm (0.08 in.), respectively. Concrete slabs were placed at both floor levels. In the Phase I tests, three horizontal restrainers on each side of both web plates were used to reduce out-of-plane displacement of the web plates due to shear buckling, and to minimize the buckling sound. The pseudo-dynamic loads were based on three ground accelerations recorded during the 1999 Chi-Chi earthquake in Taiwan, scaled to represent seismic hazards of 2%, 10%, and 50% probabilities of exceedance in fifty years. For Phase I, a total of four tests were conducted: ST (suspended test), Test 1, Test 2, and Test 3. Prior to Test 1, one side of the second floor concrete slab experienced significant cracking, and significant buckling was observed in the web plates of both stories. Hence, the test was suspended (ST) until the concrete slab was repaired. To study the performance of the SPSW with significantly buckled web plates, the same ground motion used for test ST was subsequently used for Test 1. Tests 1 through 5 were completed with only a fifteen second period of zero ground acceleration between each test. This was done to capture the effect of existing web plate buckling on the nonlinear behavior of the SPSW. For the Phase II tests, the damaged web plates were replaced and no restrainers were used.

At the completion of the Phase 1 tests, it was observed that the VBEs and HBEs had not fractured, and that the web plates on both stories had significantly buckled and cracked. The web plate restrainers did not yield or fracture, and served their purpose in the Phase I tests because smaller out-of-plane displacements of the web plates due to buckling and lower buckling sounds were noticed during the Phase I tests than during the Phase II tests. Phase I results from the application of the ground acceleration from the 2% probability of exceedance in fifty years event (the most severe event of the three that were studied) demonstrated the significant energy-

dissipation capacity of SPSWs. Another interesting observation was that the maximum inter-story drift in Test 1 was significantly greater than the maximum drift observed for the ST test, but the cumulative energy dissipated by the SPSW during the ST test was significantly greater than that for Test 1. This discrepancy is explained by the fact that once the web plates buckled during the ST test, tension field action developed. Because the test was suspended and then restarted (Test1), much larger inter-story drifts had to be imposed on the SPSW to further stress the buckled web plate and re-activate tension field action (Lin et al. 2010). Hence, during an aftershock, a SPSW with buckled web plates will further benefit from the post-buckling strength provided by tension field action if the SPSW experiences greater story drifts than it did during the main earthquake (Lin et al. 2010).

2.3 Knowledge Gap that Motivates SPSW-WC Research

Although past research has demonstrated the significant robustness, ductility, and energy dissipation of the SPSW system, some drawbacks of the system remain to be solved. Some of the main reasons for the limited used of SPSWs are (Berman et al. 2008):

- Conventional SPSWs have large column dimensions that increase the wall thickness and cost
- The lack of understanding of SPSW behavior under lateral loads has resulted in conservative design provisions that further decrease the system's competitive advantage
- The low flexural stiffness of SPSWs relative to reinforced concrete shear walls makes SPSWs challenging to use in high-rise buildings

The challenge faced in the design of the VBEs is the relatively high axial demands that are imposed on them due to the vertical reactions at the HBE ends, the vertical component of the web plate tension field action, and resistance to overturning moment. The VBE axial load arising from resistance to overturning moment can be significantly large for multi-story SPSWs (Berman et al. 2008). These large column demands may result in poor system performance and failure of the VBEs under lateral seismic loads, so inevitably the column design requirements currently available for SPSWs are conservative (Berman et al. 2008). In a VBE design procedure proposed by Berman and Bruneau (2008), it is assumed that there is uniform yielding of the web

plates along the height of the SPSW and that all HBEs have developed plastic hinges at their ends before any yielding occurs in the VBEs. These assumptions are conservative, especially the assumption of uniform web plate yielding in mid-to-high rise SPSWs (Berman et al. 2008). As a result, the axial force demands estimated for the VBEs may be large, causing the designer to use inefficient structural members for the VBEs. The coupling mechanism in a SPSW-WC system may provide a solution to this problem. The CBs help to decrease axial load demands on the VBEs in two ways. First, CBs further promote frame action of the system, causing the web plates to resist a smaller portion of the applied lateral load. Thus, thinner web plates may be used, leading to a reduction of the axial demand on the VBEs. Secondly, the vertical end reactions in the CBs counteract the axial demands from the tension field and HBE vertical end reactions, causing a reduction in the axial demand on the internal VBEs. These benefits of the SPSW-WC warrant further research of this efficient and economical system. Additionally, more research is needed to better understand the progression of yielding in the system

Improvements must also be made in the flexural stiffness of the SPSW system. In mid-to-high rise buildings, the relatively low flexural stiffness of SPSWs (compared to reinforced concrete shear walls) is an impediment to the widespread use of the system (Berman et al. 2008). Because only the VBEs in a SPSW are active in resisting overturning moment, the system is very flexible in loading cases where flexure governs over shear (Berman et al. 2008). The use of CBs in a SPSW-WC may provide adequate flexural stiffness in mid-to-high rise building applications, but there is a lack of an adequate method for designing CBs (Berman et al. 2008). Thus, more research focused on the SPSW-WC is necessary to better understand how the coupling mechanism affects the system's flexural stiffness, and to develop an adequate design methodology for the CBs.

2.4 Steel Plate Shear Wall with Coupling: Behavior under Lateral Seismic Loads

The need for more research to develop a more economical, robust, and efficient SPSW configuration has led to interest in the SPSW-WC system. Numerical simulations by Borello and Fahnestock (2012b) have demonstrated the robust seismic performance, architectural flexibility, and material efficiency of a SPSW-WC. In this study, fourteen prototype buildings were

designed and analyzed using static pushover and response-history analysis to verify the adequacy of the capacity-based design methodology.

The existing SPSW design requirements contained in the *AISC Seismic Provisions* state that the HBEs and VBEs shall be designed to remain elastic within their spans when the web plates have fully yielded under tension field action (AISC 2010). Plastic hinging is allowed at the ends of the HBEs in order to develop the plastic collapse mechanism, and hinging at the mid-span of the HBEs is not allowed because it may prevent full web plate yielding (AISC 2010). These capacity-based design provisions were adopted for the SPSW-WC (Borello and Fahnestock 2012b).

The use of CBs in addition to moment-resisting connections between boundary elements provides increased frame action, reducing the portion of the applied lateral force resisted by the web plates. Hence, thinner web plates may be used than what is possible in a SPSW. Because the required HBE strength is a function of web plate thickness, the use of thin web plates allows for the proportioning of lighter HBEs (Borello and Fahnestock 2012b). The axial demands in the VBEs of a SPSW-WC are generated by the vertical component of the web plate yielding and the vertical reaction of the HBEs (consists of the shear required to form plastic hinges in the HBE and the vertical component of the imbalance between the yielding of web plates above and below the HBE) (Borello and Fahnestock 2012b). Because in a SPSW-WC the web plates are thinner and the HBEs are relatively light, the axial demands on the VBEs are reduced relative to those on the VBEs of a SPSW (Borello and Fahnestock 2012b). The shear in the CBs that generates flexural or shear plastic hinges in the element's ends (occurring after the web plates yield under tension field action), counteracts the aforementioned axial demands on the internal VBEs of a SPSW-WC (Borello and Fahnestock 2012b). Consequently, material savings are achieved and the system is more efficient than a SPSW.

The CBs introduce another mechanism that helps to resist overturning moment. This mechanism is M_{COUP}, the couple formed by equal and opposite vertical pier forces (Borello and Fahnestock 2012b). As in a SPSW, the other mechanisms helping to resist overturning moment are the flexural strength of the external and internal VBEs (M_{EVBE} and M_{IVBE}, respectively) and each pier (M_{PIER}) (Borello and Fahnestock 2012b). These flexural strengths are used to define the system's Degree of Coupling (DC), a metric for quantifying the interaction between the coupled piers (Borello and Fahnestock 2012a; Canadian Standards Association 1994; Harries et al. 2004):

$$DC = \frac{M_{COUP}}{M_{TOTAL}} = \frac{M_{COUP}}{\sum M_{VBE} + \sum M_{PIER} + \sum M_{COUP}} \quad (2.1)$$

As equation 2.1 shows, the DC is the proportion of the total overturning moment on a SPSW-WC that is resisted by M_{COUP}. Because the DC is a function of the relative flexural strength of the VBEs, piers, and CBs, it will change as the SPSW-WC is loaded and yielding progresses throughout the system (Borello and Fahnestock 2012a).

Borello and Fahnestock (2012b) designed six-story and twelve-story prototype buildings based on a SAC five-bay square building floor plan. The seismic behavior of four SPSW configurations was studied: a single planar SPSW, a SPSW-WC with intermediate flexural/shear yielding dominated CBs (INT model), a SPSW-WC with flexural yielding dominated CBs (FLEX model), and a pair of uncoupled SPSWs (Borello and Fahnestock 2012b). On each floor of the FLEX model, the CBs were the same size as the corresponding HBEs (Borello and Fahnestock 2012b). In the INT model, the CBs were proportioned to have twice the plastic moment strength of the corresponding HBEs at each floor level (Borello and Fahnestock 2012b). The INT model had a higher DC than the FLEX model. The FLEX and INT classification for CBs was based on the *AISC Seismic Provisions* classification for eccentrically braced frame links (Borello and Fahnestock 2012b). Eight six-story building prototypes were designed with the four different configurations, and six twelve-story building prototypes were designed with the first three configurations. It was observed that for all building prototypes, the VBEs were the largest contributor to the weight of the SPSW configurations, and material efficiency increased with the degree of coupling.

Results from the static pushover analyses indicated that the yield strength of the SPSW configurations increased with the degree of coupling. As expected, results also demonstrated changes in the DC of each system based on the pattern of yielding. A decrease in the DC indicated that the CBs yielded before the piers. An increase in DC indicated that the piers yielded before the CBs, causing M_{COUP} to resist a larger part of the applied lateral load relative to the other mechanisms for resisting overturning moment.

From the results of the response history analysis based on a seismic hazard level of 10% probability of exceedance in 50 years, it is clear that SPSW-WC behavior in terms of story drift is similar to or better compared to the uncoupled configuration (Borello and Fahnestock 2012b).

It was also observed that the SPSW-WC configurations generally experienced smaller mean maximum story drifts than the single planar SPSW configurations. In general, the SPSW-WC configurations were within the two percent design story drift limit. The only exceptions were the mean maximum drifts experienced by the top stories, which exceeded the drift limit by only as much as 20%.

The results of these numerical simulations demonstrate the efficiency, and significant strength and stiffness of the SPSW-WC configuration. They also highlight the need to conduct experiments on large-scale SPSW-WC specimens to further verify the numerical models and develop a better understanding of the system's seismic behavior.

CHAPTER 3
SMALL-SCALE SPECIMEN DESIGN

To provide predictions of the behavior of the large-scale SPSW-WC specimens that will be tested in the MUST-SIM facility at the University of Illinois at Urbana-Champaign, and validate the control algorithm and loading protocol that will be used during the large scale tests, a small-scale SPSW-WC specimen was designed, built, and tested. The design process began with the application of dimensional analysis and similitude concepts to scale down the two large-scale specimens' structural members. The two large-scale SPSW-WC specimens were the system with flexural yielding dominated CBs (FLEX) and the system with intermediate CBs (INT), which have combined flexural/shear yielding in the CBs. The small-scale model approximately represented the large-scale FLEX specimen, within the constraints of available section and plate sizes. The small-scale specimen was fabricated in the Civil and Environmental Engineering Machine Shop at the University of Illinois at Urbana-Champaign.

3.1 Dimensional Analysis

The design of the small-scale specimen began with the use of dimensional analysis and the application of similitude to scale down the large-scale specimens. The theoretical framework for the use of dimensional analysis is provided by the Buckingham pi theorem, which states that a dimensionally homogeneous equation can be reduced to a relationship among independent dimensionless products of variables (pi terms) (Munson et al. 2006). Following this framework, pi terms including the variables describing the geometry and material properties of the SPSW-WC were created based on the variables' common basic dimensions. The basic dimensions used in the specimen's design were force (F), length (L), and time (T). Using similitude between the large-scale and small-scale models, scale factors for the variables of interest were developed using the pi terms.

In the dimensional analysis, the IVBEs, EVBEs, HBEs, and CBs were analyzed separately from the web plate. This was done to differentiate between the variables related to the IVBE, EVBE, HBE, and CB, and those relevant to the web plate. The basic dimensions

associated with the IVBEs, EVBEs, HBEs, and CBs were F, L, and T. The basic dimensions associated with the web plate were F and L.

Within the framework of the Buckingham pi theorem, pi terms required to scale down the large-scale IVBEs and EVBEs, HBEs, CBs, and web plates were created using the method of repeating variables. The essential steps involved in this method are (Munson et. al. 2006):

- Listing all variables relevant to the geometry and material properties of the SPSW-WC
- Expressing the variables in terms of their basic dimensions
- Determining the required number of pi terms
- Selecting a group of repeating variables (the number of repeating variables is equal to the number of basic dimensions). The repeating variables must be chosen such that when they are combined with the non-repeating variables, pi terms are formed. The group of repeating variables must contain the basic dimensions (F, L, and T for the boundary elements and CBs; F and L for the web plates). Additionally, each repeating variable must be dimensionally independent of the others in the group because this group cannot be a pi term.
- Forming pi terms by multiplying each non-repeating variable by the product of the repeating variables (each repeating variable is raised to a power that makes the product dimensionless)

The pi terms created for the IVBEs, EVBEs, HBEs, CBs, and web plate are presented in Appendix A.

3.2 Similitude

Using the pi terms, similitude between the large- and small-scale specimens was used to generate scale factors for each variable. Because the height of the large-scale model and the maximum allowable height for the small-scale SPSW-WC in the $1/5^{th}$ scale MUST-SIM Laboratory were known, the height scale factor was predetermined. The height of the large-scale specimen was approximately 20 ft., and the small-scale specimen's height in the small-scale MUST-SIM facility was limited to a maximum of 3 ft. – 2 ½ in. Consequently, the height scale factor is prescribed to 0.150. Similarly, the Young's Modulus of the material used in the large-

and small-scale specimens was known, so the scale factor for the Young's Modulus was predetermined as well. All of the scale factors (SF) are listed in Appendix B. The scale factors were used to calculate a target value for each variable:

$$Target\ Value = SF \times (Large - scale\ value\ of\ the\ variable) \tag{3.1}$$

Sections for the IVBEs and EVBEs were chosen from the 13th Edition AISC Steel Construction Manual (AISC 2008) (referred to as AISC Manual in the following text) with property values that closely matched the associated target values. To quantify how well a given property value matched a target value, the percent error was calculated:

$$Percent\ Error = \frac{(AISC\ Value) - Target\ Value}{Target\ Value} \times 100 \tag{3.2}$$

A positive error indicated a small-scale section property that was greater than the target value, and a negative error indicated a section property that was less than the target value. The small-scale design was based on the large-scale FLEX specimen because the percent error associated with the cross-sectional areas of the IVBEs and EVBEs was less than for the INT specimen. The cross-sectional area is an important geometric property because of the significant axial demands expected in the IVBEs and EVBEs of the large-scale specimen.

3.3 IVBE and EVBE Design

In the large-scale FLEX specimen, the EVBEs were W8x58 sections and the IVBEs were W8x48 sections (Figure 3.1). The two important properties that determined the sections that were used in the small-scale specimen were the sections' cross-sectional area, A, and moment of inertia, I, about the axis of bending. For the small-scale specimen, the axis of bending was about the section's weak-axis, so I_y was used. These properties were the most relevant in the selection of small-scale IVBE and EVBE sections because of the significant axial forces experienced by the members, and the pull-in forces that these elements are subjected to due to tension field action after buckling of the web plates.

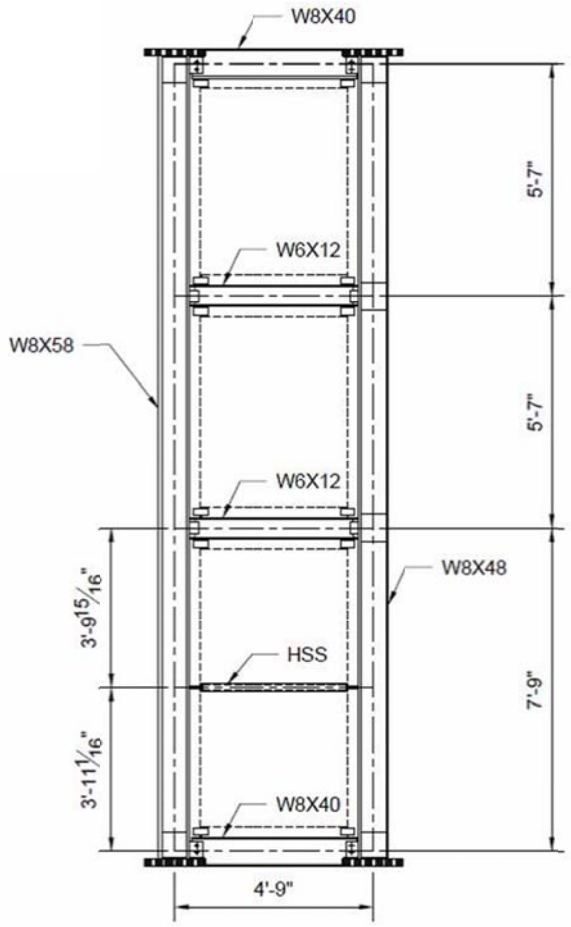

Figure 3.1 Pier of Large-Scale SPSW-WC FLEX Specimen

Scaling down the cross-sectional area and moment of inertia of the large-scale IVBEs and EVBEs produced target values for each property. The AISC Manual was used to find sections with an *A* and *I* that were close to the target values. Based on the percent error calculated between the target values and the section's *A* and *I*, the small-scale IVBE and EVBE sections were chosen.

Target property values were obtained by applying scale factors to the *A* and *I* of the large-scale EVBEs and IVBEs. Small-scale sections were chosen from the AISC Manual such that the percent error between the target values and a section's *A* and *I* were minimized. As presented in Table 3.1, this process yielded three different small-scale sections for the EVBEs and IVBEs.

The HSS2x1x1/8 section (Figure 3.2) was chosen for the small-scale EVBEs and IVBEs because it provided the best balance of error between *A* and *I*.

Table 3.1 Choosing EVBE and IVBE Sections for the Small-Scale Specimen

	Large-Scale	Small-Scale	% Error, *A*	% Error, I_y	Final Small-Scale Section
External VBE	W8x58	HSS2x1x1/8	58	-20	HSS2x1x1/8
		HSS2x1-1/2x1/8	88	111	
		HSS2-1/2x1x1/8	88	-0.4	
Internal VBE	W8x48	HSS2x1x1/8	92	-1	HSS2x1x1/8
		HSS2x1-1/2x1/8	128	162	
		HSS2-1/2x1x1/8	128	24	

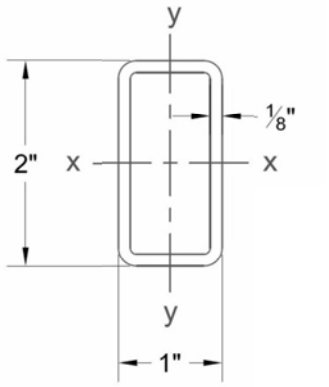

Figure 3.2 Rectangular HSS2x1x1/8 EVBEs and IVBEs

3.4 HBE and CB Design

To better match the target *I* and plastic section modulus, *Z*, of the HBEs and CBs, two different geometries were considered: solid rectangular sections and built-up W-sections. The *I* and *Z* properties of the HBEs and CBs are important because of the flexure that is expected in these elements. The small-scale sections with *I* and *Z* values that had the smallest percentage error were chosen. To prevent out-of-plane instability of the small-scale HBEs and CBs during testing, the weak-axis (x-axis) was chosen as the axis-of-bending (Figure 3.3, 3.4). Hence, the *I* and *Z* values were calculated about the x-axis.

The initial approach to choosing small-scale HBE and CB sections was to choose solid rectangular sections based on a calculated Z and the target I derived from similitude with the large-scale HBEs and CBs. Z was calculated by considering the difference in yield strength (F_y) between the steel used for the large-scale W-sections (F_y = 50 ksi) and the steel that would be used for the plates (F_y = 36 ksi). Using F_y = 36 ksi and the target M_p, the required Z for the rectangular sections was calculated using the following equation:

$$M_p = F_y \times Z \tag{3.3}$$

Using the target I and the calculated Z, the following system of equations was solved for the rectangular cross-section's depth, d, and width, b (Figure 3.3):

$$I = \frac{b \times d^3}{12} \tag{3.2}$$

$$Z = \frac{b \times d^2}{4} \tag{3.3}$$

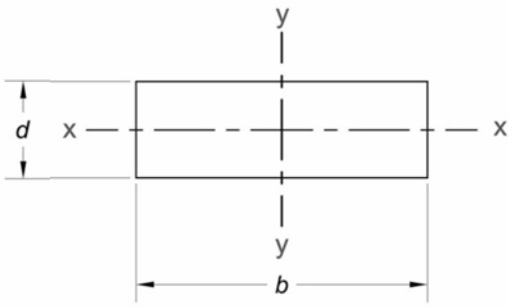

Figure 3.3 Dimensions of the Solid Rectangular Section: *b* = width, *d* = depth

The cross-section dimensions obtained using the method described above are presented in Table 3.2.

Table 3.2 Small-Scale Solid Rectangular Section – Dimensions

	Large-Scale	Small-Scale Cross-Section	
		b (in.)	d (in.)
HBE	W6x12	0.209	0.863
CB	W6x12	0.209	0.863

As seen in Table 3.2, the depth of the small-scale cross-sections is much greater than the width. Hence, during small-scale testing there may have been issues with lateral-torsional buckling in the HBEs and CBs. To avoid this, three more configurations were considered for the small-scale HBEs and CBs: built-up W-sections composed of three steel plates, solid rectangular sections designed based on the target moment of inertia, and solid rectangular sections designed based on the target plastic section modulus.

The built-up section composed of three plates is shown in Figure 3.4. To determine if this configuration was appropriate for the small-scale specimen, it was designed for each of the HBEs and CBs.

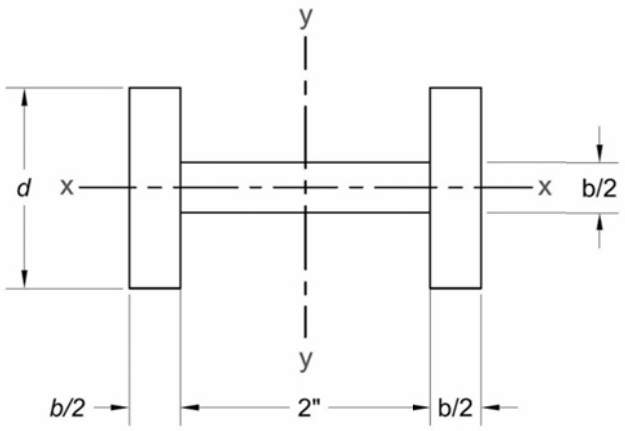

Figure 3.4 Built-Up HBE and CB Section

Table 3.3 presents the dimensions of the small-scale built-up HBE and CB sections, and the error between the calculated *I* and *Z* and associated target values.

Table 3.3 Built-Up Small-Scale HBE and CB Sections

	Large-Scale	b/2 (in.)	d (in.)	% Error, I	% Error, Z
HBE	W6x12	1/8	7/8	27.6	43.2
CB	W6x12	1/8	7/8	27.6	43.2

The other options considered for the HBEs and CBs were two designs for a solid rectangular section (Figure 3.3): (1) one in which the section was designed based on the target *I*, and (2) a second option in which the sections were designed based on the target *Z*. In both cases, the width, *b*, of the sections was prescribed to be 1-3/8 in. This was done to ensure that the width of the solid rectangular sections was within the workable flat dimension of the HSS2x1x1/8 sections. The workable flat (Figure 3.5) is obtained using the AISC Manual provision for calculating the outer radius dimensions of HSS rounded corners, and it is 1-7/16 in. for the HSS2x1x1/8 section:

$$\text{outside corner radii} = 2.25\text{t}_{\text{nom}} \tag{3.4}$$

$$\text{workable flat} = (\text{HSS depth}, d) - (2 \times \text{outside corner radii}) \tag{3.5}$$

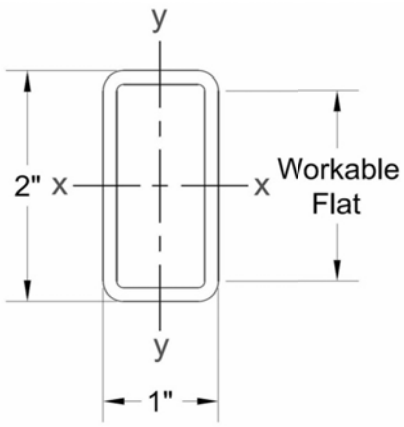

Figure 3.5 HSS2x1x1/8 VBEs – Workable Flat Dimension

The difference between the two designs based on a solid rectangular section was the procedure to calculate the section's depth, *d*. In the first option, *d* was based on the target *I*. Thus, *d* was calculated using equation 3.2. After *d* was rounded to the nearest 1/16 in., *I* was

recalculated and *Z* was calculated. In the second option, *d* was based on the target *Z*. Thus, *d* was calculated using equation 3.3. With *d* rounded to the nearest 1/16 inch, *Z* was recalculated and *I* was calculated. The purpose of these procedures was to determine which set of cross-sectional dimensions provided a better approximation of the target *I* and *Z*.

Tables 3.4 and 3.5 present the cross-sectional dimensions and percent errors associated with *I* and *Z* for the solid rectangular sections designed based on the target moment of inertia and target plastic section modulus, respectively.

Table 3.4 Solid Rectangular Section for HBEs and CBs (Based on Target *I*)

	Large-Scale	b (in.)	d (in.)	% Error, I	% Error, Z
HBE	W6x12	1-3/8	1/2	27.8	120.8
CB	W6x12	1-3/8	1/2	27.8	120.8

Table 3.5 Solid Rectangular Section for HBEs and CBs (Based on Target *Z*)

	Large-Scale	b (in.)	d (in.)	% Error, I	% Error, Z
HBE	W6x12	1-3/8	5/16	-68.7	-13.6
CB	W6x12	1-3/8	5/16	-68.7	-13.6

As can be observed in Tables 3.3 and 3.4, the moment of inertia and plastic section modulus of the built-up W-section and the solid rectangular section based on the target *I* were above the respective target values. It is observed in Table 3.5 that the moment of inertia and plastic section modulus of the solid rectangular section based on the target *Z* were below the respective target values. It should be noted that the capacity-based design methodology followed for the large-scale specimen accounted for the CBs and HBEs reaching their plastic moment capacities at their ends and developing plastic hinges in these regions. Consequently, it was important for the plastic section modulus of the small-scale HBEs and CBs to be close to their respective target values. Based on the percentage errors for the plastic section modulus presented in Tables 3.3, 3.4, and 3.5, the solid rectangular section based on designing for the target *Z* was chosen because of the relatively small error in *Z*.

3.5 Web Plate Design

For the design of the small-scale web plate, three options were considered. First, similitude was strictly maintained, and the appropriate small-scale web plate thicknesses were determined from the large-scale web plates. Second, the use of perforated web plates was explored. Third, braces placed at the back and front of the specimen at each story were considered.

To maintain strict similitude between the large-scale FLEX specimen and the small-scale specimen, the thickness of the large-scale web plates (t_w) was scaled down using the scale factor of 0.15 determined for the web plate thickness. The web plates on the first and second stories of the large-scale FLEX specimen were 0.056 in. thick, and the third story web plate was 0.044 in. thick. Thus, the scaled-down thicknesses for the web plates on the first and second stories, and the third story plate were 0.0084 in. and 0.0066 in., respectively. Since these thicknesses are not available for appropriate plate material, full web plates were not an option.

The other option considered was to use perforated web plates (Figure 3.6). In a design requiring web plate thicknesses smaller than the minimum provided by steel fabricators, perforations can be used to reduce the strength and stiffness of readily available solid web plates to the levels required by the design (AISC 2010).

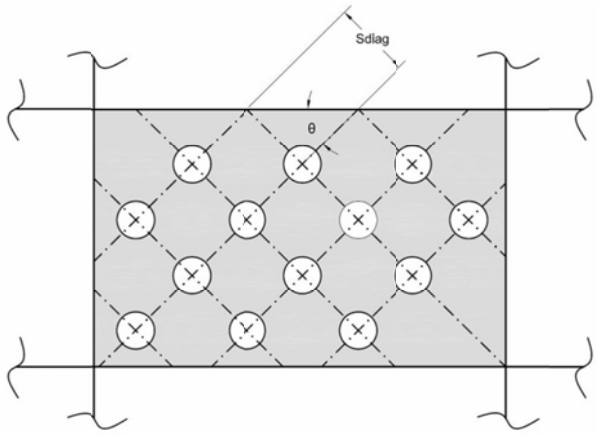

Figure 3.6 Special Perforated Steel Plate Shear Walls (AISC 2010)

To use the same large-scale web plate thicknesses but with the plates' strength and stiffness reduced to the levels required by similitude, different patterns of circular perforations

were investigated. The following equation was used to determine the required number of horizontal rows of perforations in the web plate (AISC 2010):

$$t_{eff} = \frac{1-\frac{\pi}{4}\left(\frac{D}{S_{diag}}\right)}{1-\frac{\pi}{4}\left(\frac{D}{S_{diag}}\right)\left(1-\frac{N_r D \sin\alpha}{H_c}\right)} t_w \tag{3.6}$$

In equation 3.6, H_c is the clear column height between beam flanges, N_r is the number of horizontal rows of perforations, D is the hole diameter, S_{diag} is the shortest center-to-center distance between the circular perforations, α is the angle (degrees) of the shortest center-to-center lines in the perforation pattern measured from the vertical, t_{eff} is the effective web plate thickness, and t_w is the web plate thickness. Because S_{diag} must be at least $1.67D$, S_{diag} is prescribed as $1.67D$ (AISC 2010).

For each story of the small-scale specimen, t_{eff} is prescribed as the scaled-down web plate thickness, and t_w is prescribed as the large-scale plate thickness to maintain similitude. α was set equal to the angle of the brace measured from the vertical for each story. No suitable combination of D and N_r was found which resulted in the required t_{eff}. Thus, perforated plates were not a feasible option.

The final option that was studied was the use of braces to represent the web plates at each story of the small-scale specimen. For the design of the brace, the nominal shear strength, V_n, was calculated for each of the three large-scale web plates using the following equation proposed by Berman and Bruneau (2003):

$$V_n = 0.5 F_y t_w L_{cf} \sin 2\alpha \tag{3.7}$$

where F_y is the yield strength of the web plate, L_{cf} is the clear distance between column flanges, and α is the angle of inclination of the principal tensile stresses (due to tension field action) in the web plate measured from the vertical. α was determined using the following equation developed by Timler and Kulak (1983):

$$\tan^4 \alpha = \frac{1+\frac{t_w L}{2A_c}}{1+t_w h\left(\frac{1}{A_b}+\frac{h^3}{360 I_c L}\right)} \tag{3.8}$$

where α and t_w are as defined previously, L is the distance between the VBE centerlines, A_c is the average VBE cross-sectional area, h is the distance between HBE centerlines, A_b is the average HBE cross-sectional area, and I_c is the average VBE moment of inertia.

Each value of V_n was then scaled-down using the scale factor for nominal shear strength (0.0225). The effective brace thickness, t_w, for each story in the small-scale specimen was set equal to the web plate thickness at each corresponding story in the large-scale specimen. Instead of using α, the angle β (measured from the vertical to the diagonal brace) was used (Figure 3.7).

$$\beta = \tan^{-1}\frac{L}{h} \tag{3.9}$$

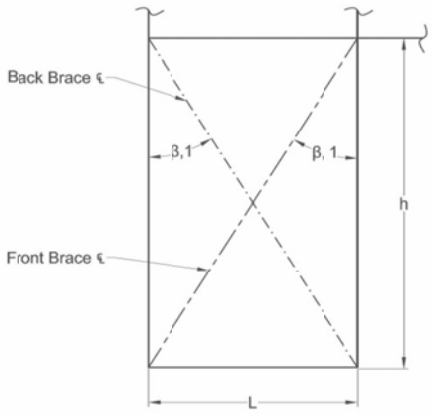

Figure 3.7 Small-Scale SPSW-WC Geometry (Only the First Story is Shown)

With small-scale values of V_n ($V_{n\text{-}sc}$) and t_w determined, the width of the effective braces was calculated based on the respective tensile yield forces, P_y. Referring to Figure 3.8, the required brace cross-sectional area, A_g, was calculated using the following equations:

$$P_y = F_y \times A_g \tag{3.10}$$

$$\sin\beta = \frac{V_{n-sc}}{P_y} \tag{3.11}$$

$$A_g = \frac{V_{n-sc}}{F_y \times \sin\beta} \tag{3.12}$$

.

Once the required gross cross-sectional area of the brace was determined, the required width of the brace, *w*, was calculated:

$$w = \frac{A_g}{t_w} \tag{3.13}$$

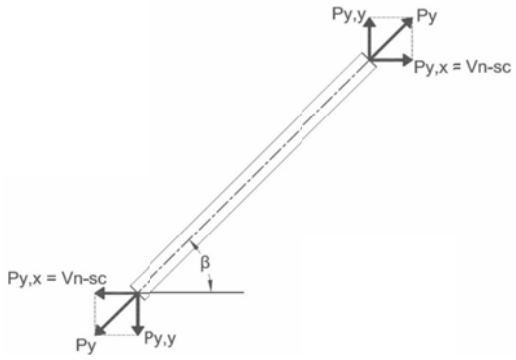

Figure 3.8 Tensile Yield Force in Brace

Performing the above calculation for the front and back braces of each story gives the required brace widths presented in Table 3.6.

Table 3.6 Brace Width, *w*

Story	w (in.)
1	1
2	13/16
3	13/16

Of concern was the need to have the effective braces yield in tension but not go into the strain hardening region of their stress-strain relation. The braces would be fabricated from the same material as the web plates for the large-scale FLEX specimen, so results from coupon tests

on the web plate material were used to inform proportioning of the braces (Figure 3.10). The actual thickness of the material was 0.060 in., and its average yield stress was 54 ksi. To remain within the average yield plateau of the tensile stress-strain relationships in Figure 3.9, the braces were proportioned with a decreased width throughout most of their length at all stories. These lengths were determined from the geometry of the small-scale specimen such that the required strains in the braces would be achieved. Using equations 3.12 and 3.13 with F_y = 54 ksi, a decreased with of ½ in. was chosen for all stories (Figure 3.10). The widths shown in Table 3.6 were maintained at the regions near the ends of the braces to ensure adequate connections to the VBEs.

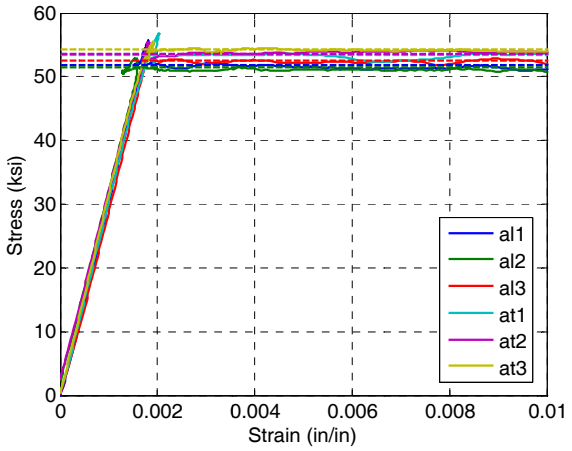

Figure 3.9 Stress-Strain Curves: Tests on Large-Scale Web Plate Material Samples

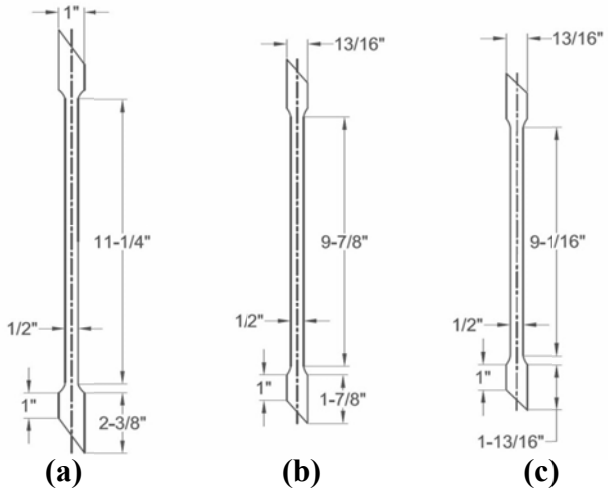

Figure 3.10 Braces: (a) First Story, (b) Second Story, (c) Third Story

3.6 Final Small-Scale SPSW-WC Design

An elevation of the small-scale specimen is presented in Figure 3.11. A photo of the fabricated specimen is shown in Figure 3.12. All connections in the specimen were fillet weld connections. The HBEs in both piers were welded to top and bottom ½"-thick steel connection plates. The total height of the specimen is 2 ft.- 10-5/8 in., and the bay widths are 9 in. for each pier. Detailed drawings of the specimen are presented in Appendix C of this document.

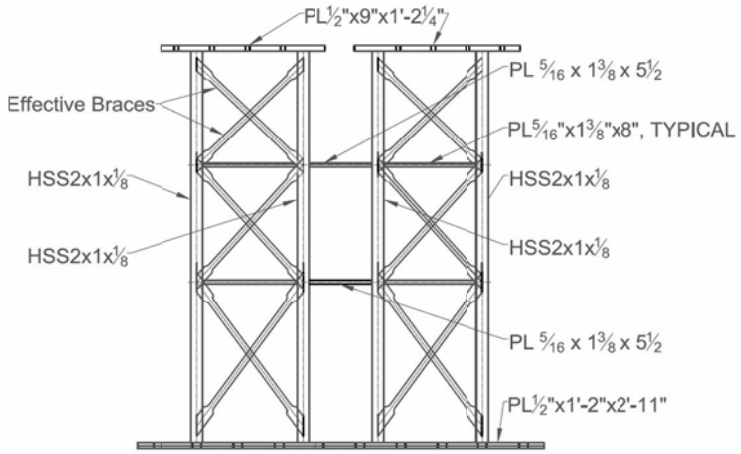

Figure 3.11 Small-Scale SPSW-WC Elevation

Figure 3.12 Small-Scale SPSW-WC Specimen

CHAPTER 4
ANALYTICAL AND NUMERICAL PREDICTIONS OF SPECIMEN CAPACITY

To complement the experimental investigation, analytical and numerical studies of the small-scale SPSW-WC were conducted. The analytical studies included a plastic analysis of the system and a determination of the buckling capacity of the IVBEs and EVBEs. The kinematic method of plastic analysis was used to determine the small-scale specimen's ultimate strength. The IVBE and EVBE buckling capacity was determined following the column design provisions in the Specification for Structural Steel Buildings (AISC 2008). The numerical studies consisted of models of the specimen developed in SAP2000 and the Open System for Earthquake Engineering Simulation (OpenSees). SAP2000 is a structural analysis software package that is widely used in structural engineering design offices. OpenSees is an open source software for developing finite element models of structural systems and simulating the response of the models to seismic loads (OpenSees). In SAP2000 and OpenSees, nonlinear static pushover analyses were conducted to determine the small-scale specimen's ultimate strength.

4.1 Plastic Analysis by the Kinematic Method

Borello and Fahnestock (2012a) demonstrated that the kinematic method of plastic analysis is an adequate approach for determining the plastic strength of the SPSW-WC system. In the kinematic method, a plastic collapse mechanism for the system is assumed and the principle of virtual work is applied to determine the system's ultimate strength. A plastic collapse mechanism develops when sufficient plastic hinges have formed in the system for it to become unstable. As stated by the principle of virtual work, the total virtual work performed by forces external to the system is equated to the total virtual work performed by forces internal to the system. The specimen's ultimate (base shear) strength was obtained using the kinematic method of plastic analysis.

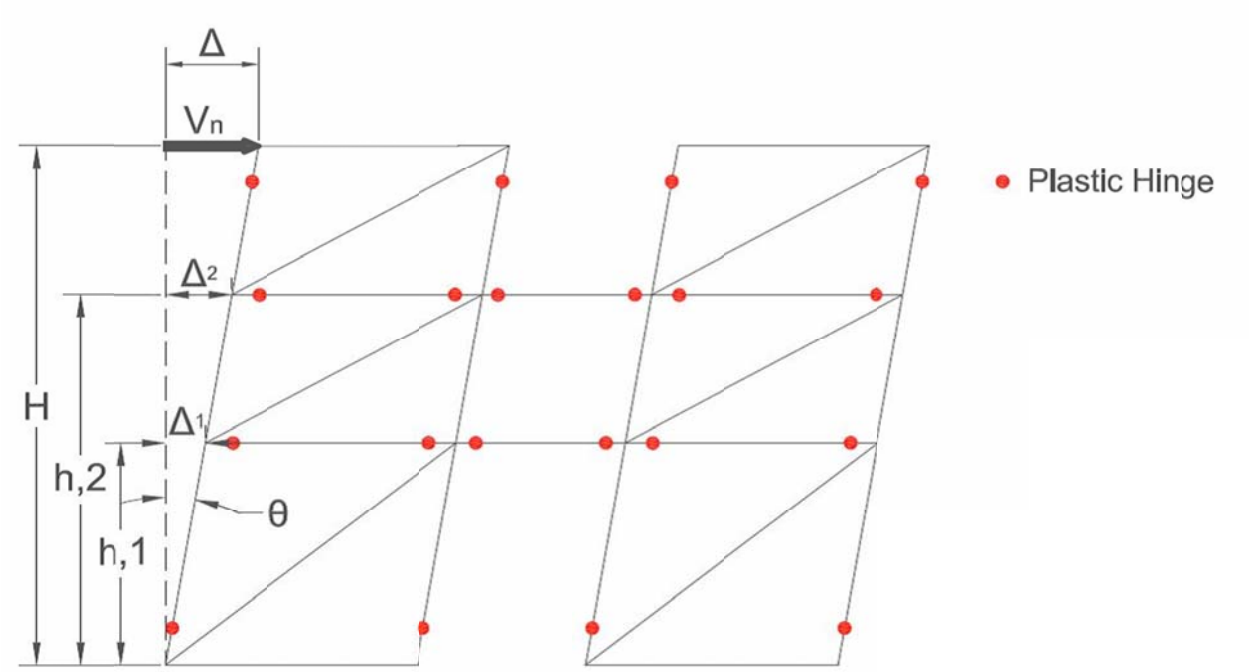

Figure 4.1 Plastic Collapse Mechanism (Pier 1 is Left Pier, Pier 2 is Right Pier)

For the analysis, the collapse mechanism presented in Figure 4.1 was assumed. This assumed mechanism follows the basis of the capacity-based design methodology adopted for SPSW-WC. The braces in all stories were assumed to yield in tension, plastic hinges were assumed to develop at the ends of the HBEs and CBs, and plastic hinges were assumed to form at the base and top of the IVBEs and EVBEs. Plastic hinges were assumed to develop at the top of the IVBEs and EVBEs due to the relatively high flexural stiffness of the LBCB loading platform-to-top plate connection compared to that of the IVBEs and EVBEs. The external lateral force V_n was the only force assumed to be acting on the system, acting through a virtual horizontal displacement Δ. Because of static equilibrium of the specimen, V_n is equal to the base shear (ultimate) strength of the system. Thus, the external virtual work, W_{EV}, on the small-scale specimen is:

$$W_{EV} = V_n \Delta \tag{4.1}$$

The internal virtual work is performed by the horizontal components of the tension force in the brace at each story displacing a distance Δ_i associated with a given story i, and the moments at

the plastic hinges moving through a virtual rotation θ. Hence the internal virtual work, W_{IV}, is expressed as:

$$W_{IV} = \left(8M_p^{HBE}\theta\right) + \left(4M_p^{CB}\theta\right) + \left(8M_p^{VBE}\theta\right) + W_{IV-Braces} \tag{4.2}$$

Assuming small virtual displacements and rotations, the following relation is valid:

$$\theta \approx \frac{\Delta}{H} \tag{4.3}$$

Here, H is the total height of the specimen (Figure 4.1). Substituting equation 4.3 into 4.1, the following relation is obtained:

$$W_{EV} = V_n\theta H \tag{4.4}$$

Only the horizontal component of the tension force in the effective brace ($P_{y,x}$) at each story does work by going through the virtual displacement Δ_i (Figure 4.2). $P_{y,x}$ for each story i is determined using the following equation:

$$\left(P_{y,x}\right)_i = \left(F_y A_g \sin\beta\right)_i \tag{4.5}$$

In equation 4.5, F_y is the yield stress of the brace, A_g is the cross sectional area of the ½"-wide brace cross-section, and β is the angle between the brace centerline and the centerline of the VBE. Using trigonometry, the displacements Δ_i of each story were written in terms of θ and substituted into the expressions for the internal virtual work done by the horizontal component of the brace forces:

$$\Delta_i = h_i\theta \tag{4.6}$$

h_i is the height of story i (Figure 4.1).

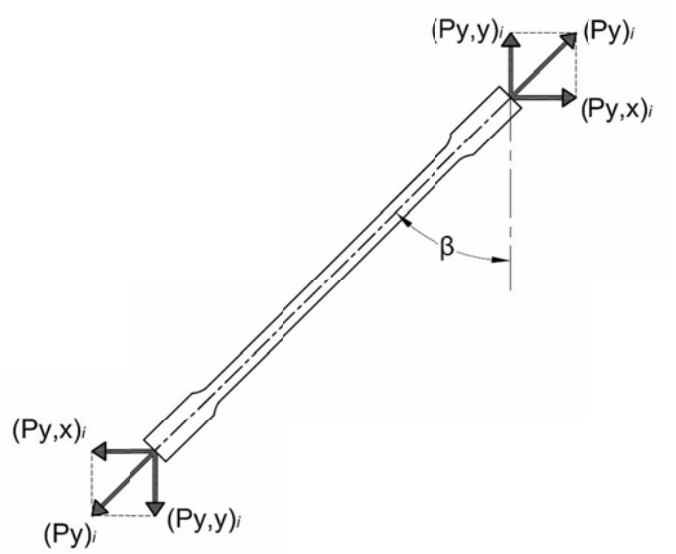

Figure 4.2 Tension Force in the Braces

Applying the principle of virtual work, equations 4.2 and 4.4 were set equal to each other:

$$V_n\theta H = \left(8M_p^{HBE}\theta\right) + \left(4M_p^{CB}\theta\right) + \left(8M_p^{VBE}\theta\right) + \sum_{i=1}^{3}\left(F_y A_g \sin\beta\right)_i h_i\theta \quad (4.7)$$

The last term in equation 4.7 represents the total virtual internal work done by the horizontal component of the tension force in the braces. At the second and third story floors, the work done by the horizontal force component of the brace force acting at the top and bottom of the story was considered and added algebraically (i.e. a horizontal tension force component acting in the opposite direction to the direction of the story displacement Δ_i did negative work). Observing that the virtual rotation θ cancels out of equation 4.7, and solving for V_n, the ultimate strength of the system was estimated to be 4.8 kips.

4.2 Buckling Capacity of the IVBEs and EVBEs

The buckling capacity of the HSS2x1x1/8 members used for the small-scale IVBEs and EVBEs was determined to ensure that local or global instabilities would not occur in the IVBEs and EVBEs during testing. The buckling capacity was calculated per Chapter E (Design of Compression Members) of the Specification for Structural Steel Buildings (AISC 2008). The

effective length factor K was taken as 1.0 for the calculations. Because the HSS2x1x1/8 section is classified as compact, local buckling of the cross-section is not an issue.

The design compressive strength, $\phi_c P_n$, of the IVBE and EVBE sections on each story of the specimen was calculated. P_n was based on the limit state of flexural buckling about the weak-axis (y-axis) of the cross sections (Figure 4.3). The sections were classified under elastic flexural buckling behavior at each story.

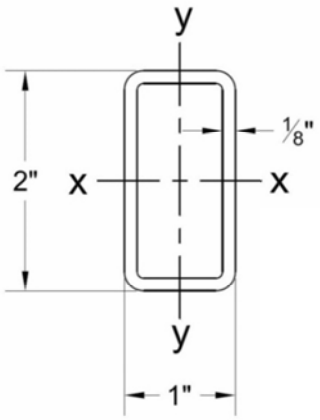

Figure 4.3 HSS2x1x1/8 Cross-Section

Table 4.1 presents the IVBE and EVBE lengths for each story and their design compressive strength based on the limit state of flexural buckling. The maximum vertical force that can be delivered in the testing facility to the IVBE or EVBE of one pier in the specimen is 3 kips. The factors of safety for each story are presented in Table 4.1.

Table 4.1 EVBE and IVBE Design Compressive Strength Based on the Limit State of Flexural Buckling

Story	EVBE/IVBE Length (in.)	$\varphi_c P_n$ (kips)	Applied Vertical Force Per Element (kips)	Safety Factor
1	13-11/16	23	3	7.7
2	9-11/16	24	3	8.0
3	9-11/16	24	3	8.0

4.3 SAP2000 Model

To complement the limit analysis described above, a model of the small-scale specimen was developed in SAP2000 (Figure 4.4), and a nonlinear static pushover analysis was performed.

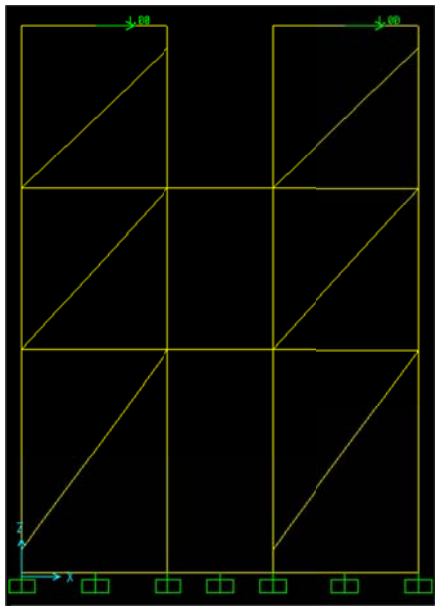

Figure 4.4 SAP2000 Model of Small-Scale Specimen

Material properties for the IVBEs and EVBEs, HBEs, CBs, braces, and top and bottom connecting plates were defined. The modulus of elasticity of the braces was 30,612 ksi based on the results of the coupon tests discussed in Chapter 3. All other materials had a modulus of elasticity of 29,000 ksi. The material defined for the HSS2x1x1/8 section used for the IVBEs and EVBEs was specified as ASTM A500 Grade B. This is the preferred material specification for rectangular HSS structural shapes (AISC 2008). The minimum yield stress, F_y, was defined as 46 ksi, and the minimum tensile stress, F_u, was defined as 58 ksi. The material used to model the rectangular plates used for the HBEs and CBs was specified as ASTM A36, with F_y of 36 ksi and F_u of 58 ksi. The material properties of the braces were based on the results of the coupon tests discussed in Chapter 3, section 3.5, with F_y of 54 ksi, and F_u of 63 ksi. The top and bottom connecting plates welded to the specimen were specified with ASTM A36 material, with F_y of 36 ksi and F_u of 58 ksi.

Frame elements were used to model the IVBEs and EVBEs, HBEs, CBs, connecting plates and braces. Because the connecting plates were modeled with frame elements, the flexural stiffness of these elements was adjusted by applying magnification factors to the elements' moments of inertia. Only the braces that would be in tension under the applied lateral load were modeled, as it was assumed that the braces would provide negligible compression strength. For the boundary conditions, the supports at the base of the specimen were modeled as fixed supports.

To perform the nonlinear static analysis, plastic hinges were added along the lengths of the frame elements (Figure 4.5). For each VBE, two plastic hinges were added: one at the base and one at the top of the third story. A plastic hinge was added to each end of the HBEs and CBs. Two plastic hinges were also added to each brace along the length with the reduced with of ½ in. For the IVBEs and EVBEs, plastic hinges with coupled axial force and moment behavior were assigned to capture the interaction between axial force and overturning moment demands in the IVBEs and EVBEs. For the HBEs and CBs, the plastic hinges were assigned to the rotational degree-of-freedom. For the effective braces, the plastic hinges were assigned to the axial degree-of-freedom. All hinges were defined as deformation controlled with ductile behavior.

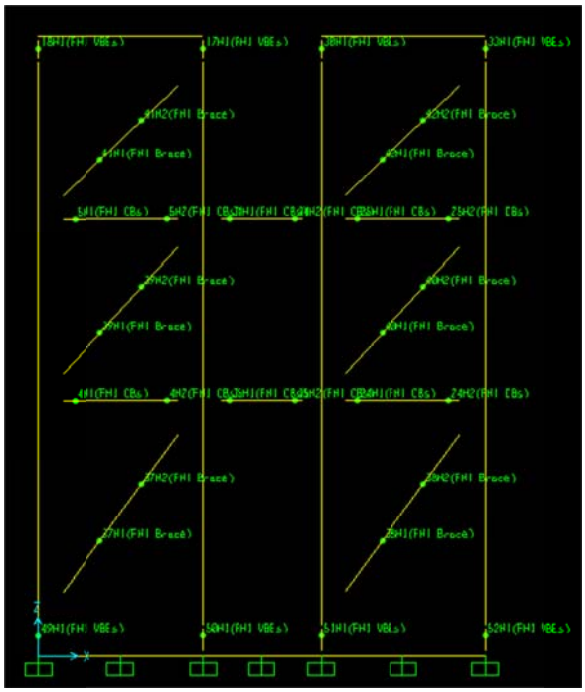

Figure 4.5 Plastic Hinge Assignments in SAP2000 Model

Two load types were assigned. One was the dead load due to the self-weight of the elements. The other load was a 1.0 kip lateral load assigned to the nodes representing the control point at the top of each pier (Figure 4.4). The control points were on the top connecting plates at the points that coincided with the centerlines of the piers.

The two nonlinear static load cases used in the simulation were DEAD (gravity loads due to self-weight) and Lateral. During the analysis, the DEAD load case was run first, and it initiated at a state in which the specimen was unstressed. This load case was applied under force control. Subsequently, the Lateral load case was applied in displacement control. The horizontal displacement of the node at the control point of the left pier was monitored. The analysis continued until the displacement target of two inches was reached. This target was based on the horizontal stroke limit of the actuators in the small-scale facility.

The results of the nonlinear static analysis showed that yielding was achieved at the assumed plastic hinge locations (Figure 4.6). This pattern of plastic hinge formation in the small-scale specimen coincides with the pattern predicted for the large-scale specimens. The resulting nonlinear static pushover curve is presented in Figure 4.9. Based on the nonlinear static analysis, the specimen's ultimate strength was approximately 5.5 kips.

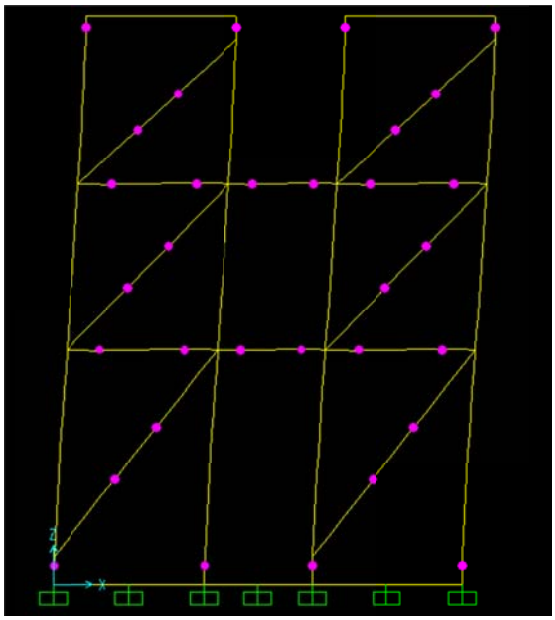

Figure 4.6 Formation of Plastic Hinges

4.4 OpenSees Model

A numerical model of the specimen was also developed in OpenSees, and a nonlinear static pushover analysis was performed. As presented in Figure 4.7, the small-scale specimen was modeled as a plane frame. The Steel01 Material object was chosen as the material model for the IVBEs, EVBEs, HBEs, CBs, and braces because it is based on a uniaxial bilinear stress-strain relationship (OpenSees). Fiber sections were only defined for the IVBEs, EVBEs, HBEs, and CBs. The fiber section defined for the IVBE and EVBE sections consisted of 30 fibers in the local y-direction and three fibers in the local z-direction (Figure 4.8). The rounded corners of the HSS cross-section used for the IVBE and EVBE sections were neglected and right-angle corners were used in defining the fiber sections. The fiber sections defined for the HBEs and CBs each consisted of ten fibers in the local y-direction and one fiber in the local z-direction (Figure 4.8). Few fibers were defined in the local z-directions because the analysis was planar.

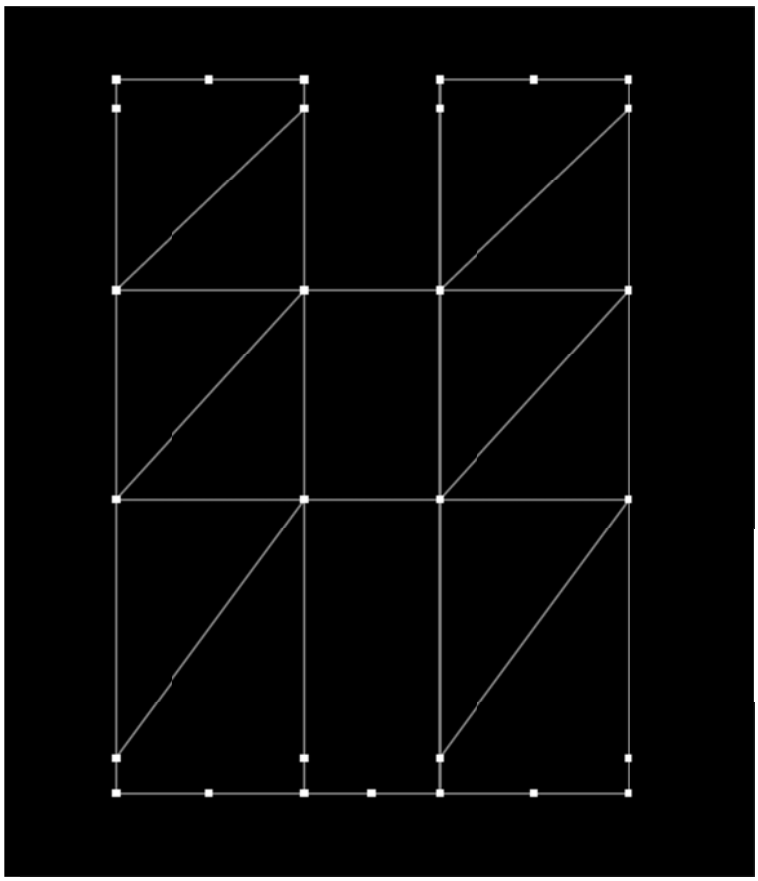

Figure 4.7 OpenSees Model of Small-Scale Specimen

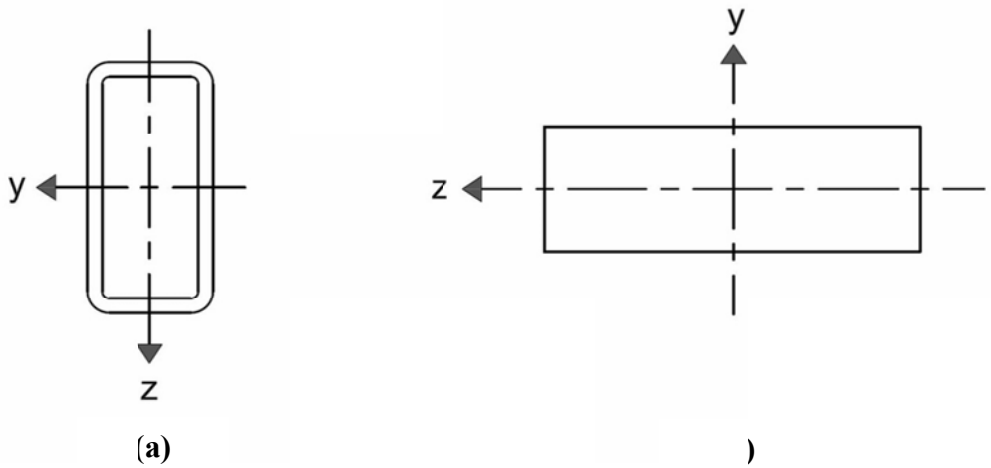

Figure 4.8 Coordinates for (a) IVBE and EVBE, and (b) HBE and CB Fiber Sections

In defining the elements that were used in the OpenSees model, a Corotational Coordinate Transformation object was used to define the method for transforming from the local coordinate system of each beam element to the global coordinate system. The Coratational Coordinate Transformation object was chosen for its ability to be used when the model undergoes large displacements (OpenSees). The EVBEs, IVBEs, HBEs, and CBs were modeled with force-based beam-column elements. This element was chosen because it accounts for the plastic behavior expected in the boundary elements. Truss elements were used to model the braces. Top and bottom connecting plates with an effective width were defined, and elastic beam-column elements were used to model these elements.

The location of the control point of each pier was the same as in the SAP2000 model: on the top floor at the middle of each pier. A 1.0 kip concentrated lateral load was placed at each control point, and the horizontal displacement of one of those points was monitored during the analysis. The distributed gravity loads due to the self-weight of the members were transformed into equivalent nodal loads.

Before performing the nonlinear static analysis, the gravity loads were applied under load control. The nonlinear static pushover analysis was then initiated from the specimen's stressed state. The solution algorithm for this nonlinear analysis was Newton with Line Search. The pushover simulation was run under displacement control, with a target displacement of 2 in.

The results of the pushover analysis indicate an ultimate strength of 4.78 kips (Figure 4.9). This agreed with the strength estimated using the analytical model, which helps to further

validate the use of plastic analysis and the assumed collapse mechanism for determining the ultimate strength of a SPSW-WC. The SAP2000 model provided an unconservative estimate of the small-scale specimen's strength. This may be due to the fact that the use of fiber sections in the OpenSees model results in a relatively more accurate model because nonlinear behavior due to yielding is captured more accurately than by the point hinges in the SAP2000 model. As shown in Figure 4.10, yielding was observed in all of the braces. No significant strain hardening was observed in the braces because of the low strain-hardening ratio (0.0001) assigned to the brace material properties to capture the stress-strain behavior observed in the coupon tests (see Chapter 3, section 3.5). In Figure 4.10, Pier 1 refers to the pier on the left in Figure 4.7, and Pier 2 refers to the pier on the right in the same figure.

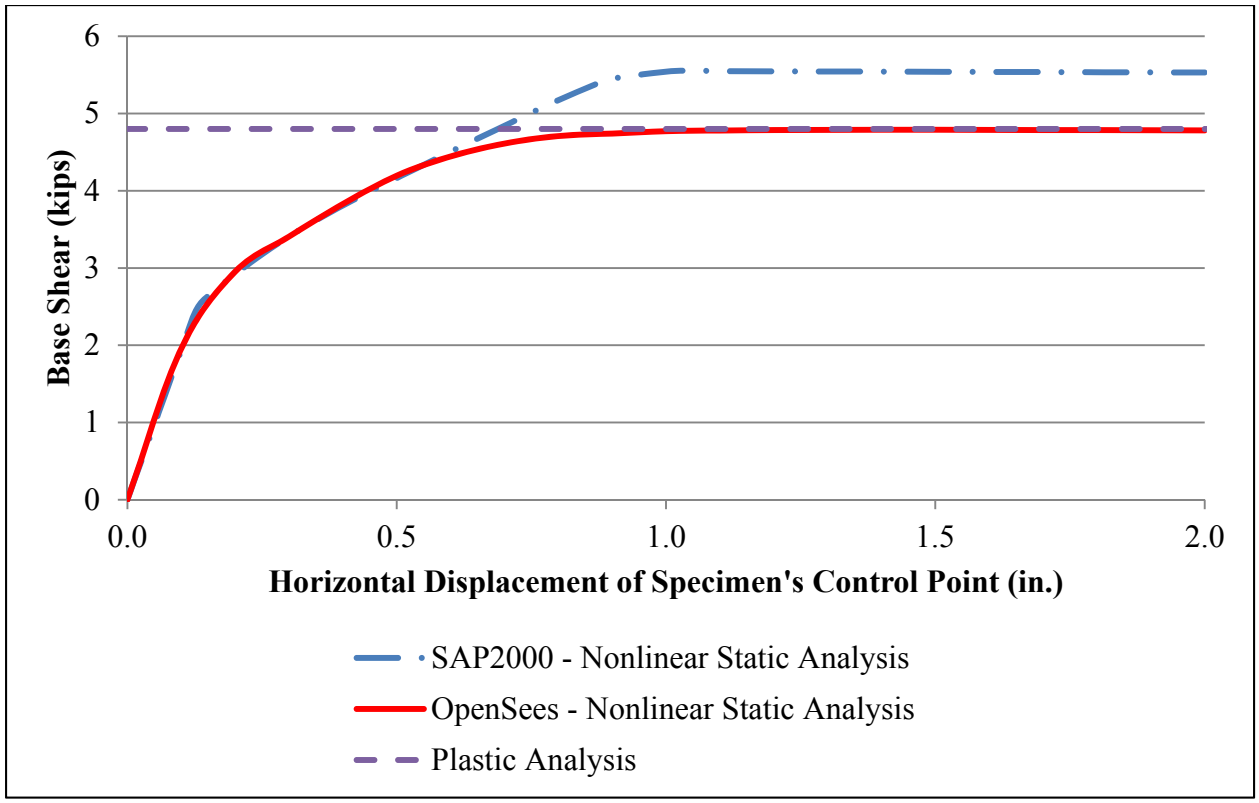

Figure 4.9 Pushover Curves for the Small-Scale Specimen

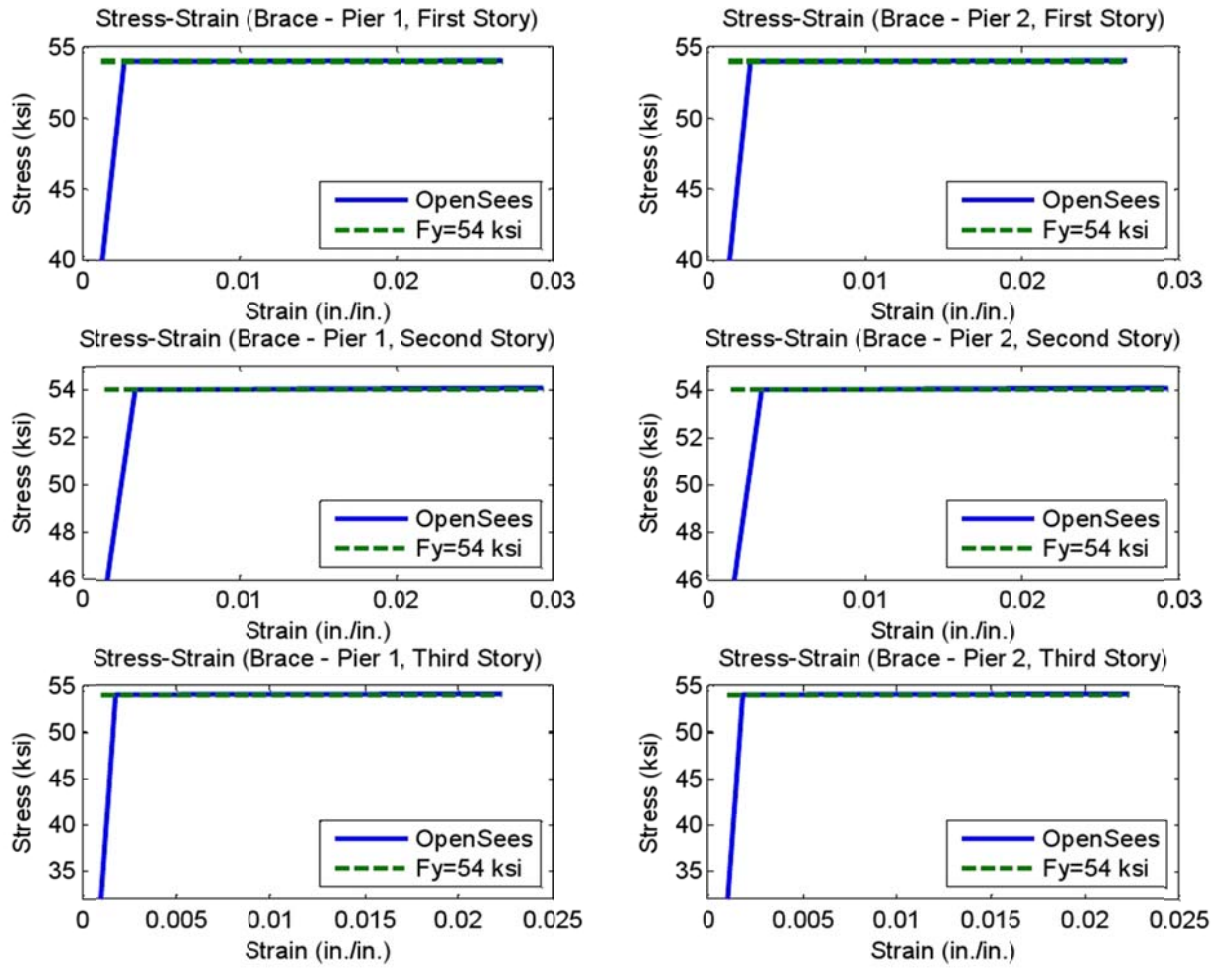

Figure 4.10 OpenSees Stress-Strain Curves for Braces

Figures 4.11 and 4.12 present the relationship between the moment and rotation at the plastic hinge regions near the ends of the HBEs and CBs, respectively. After analyzing the stress-strain relationship at a fiber in sections near the ends of each element, it was determined that full yielding of the cross-sections occurred near the element ends, indicating that the plastic moment was reached and plastic hinges developed at those cross sections. For the HBEs, full yielding occurred at a plastic rotation of approximately 0.02 rad. Full yielding of the CBs was achieved at plastic rotations between 0.02 rad and 0.03 rad.

The relationship between story shear and story drift is shown in Figure 4.13 for each story of the model. Because a concentrated lateral load was applied to the top of the model, the story shear along the model's height was constant and equal to the base shear of 4.78 kips. The

plots in the figure show the portions of the total story shear that was carried by the IVBEs and EVBEs due to frame action, and the portion that was carried by the braces. To calculate the story drifts, the story drifts of each IVBE and EVBE were recorded as part of the OpenSees simulation output. These drifts were averaged for each corresponding story to obtain the story drifts for the entire model. As can be observed in the figure, initially at each story, the braces resisted a greater portion of the total story shear than did frame action. As the braces yielded and they could no longer carry any additional load, the portion of the total story shear resisted by frame action increased relative to the braces. The difference between the amount of shear resisted through frame action and the amount resisted by the braces decreased along the model's height. This may be due to the decrease in the brace length along the specimen's height and its effect on the sequence of yielding in the braces. It can be observed in the plots of Figure 4.13 that the story drifts at which the braces yielded increased along the model's height. Thus at the second and third stories, the braces were able to continue to resist lateral load at relatively greater story drifts compared to the first story after the first story braces yield. Because this behavior was more significant in the model's upper stories, the braces and frame action shared nearly equal amounts of the story shear at the upper stories, especially at the third story. Additionally, on the third story, it is observed that at drift levels between about 0.25% and 0.4%, the portion of the story shear resisted by frame action was relatively constant, while the portion resisted by the braces increased. Once the braces on this story yielded, frame action began to resist the additional story shear that could no longer be resisted by the yielded braces.

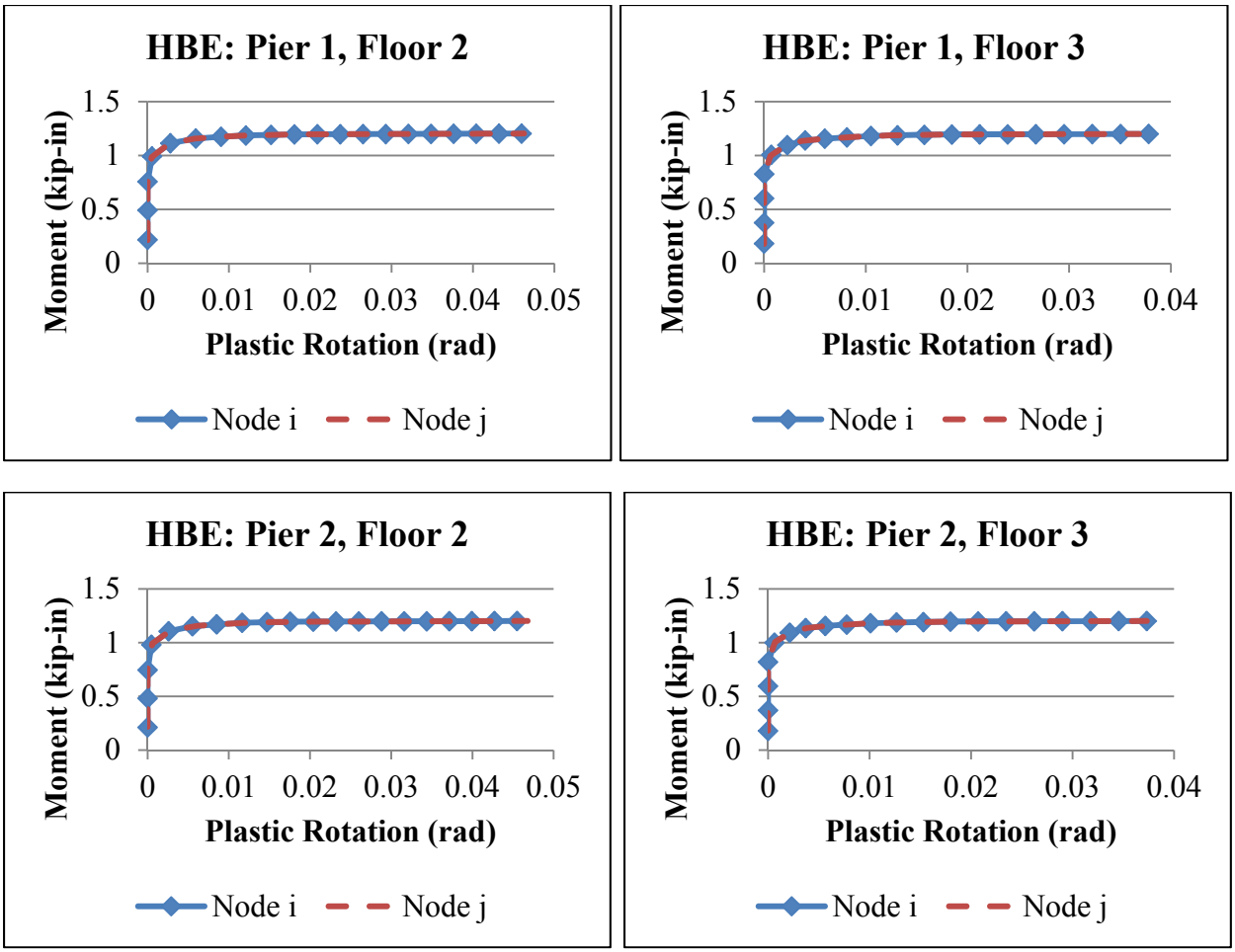

Figure 4.11 Moment vs. Plastic Rotation at the Plastic Hinge Regions of the HBEs

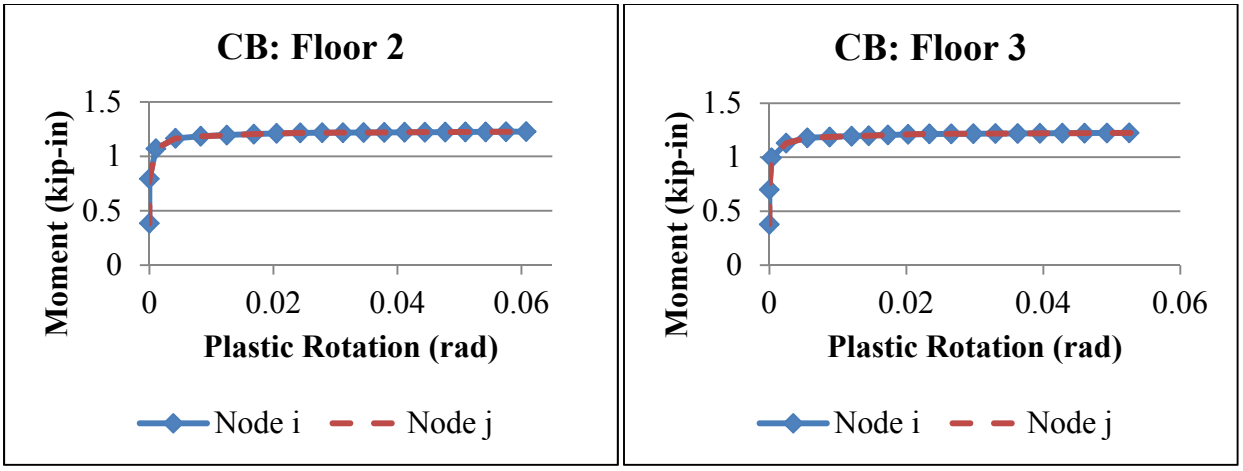

Figure 4.12 Moment vs. Plastic Rotation at the Plastic Hinge Regions of the CBs

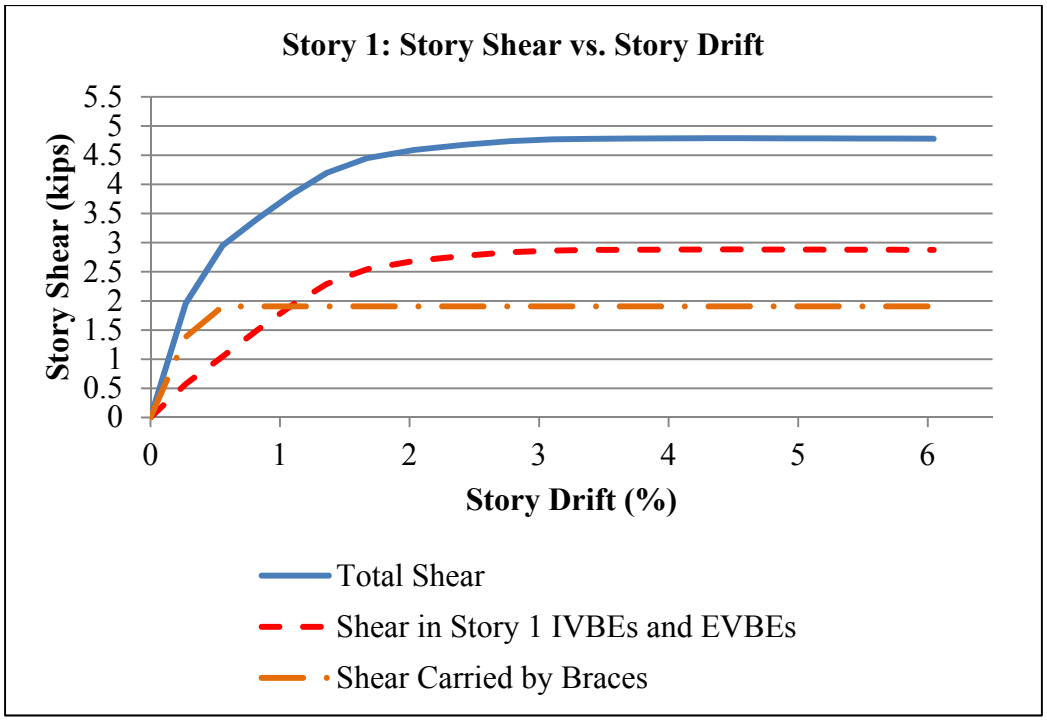

(a)

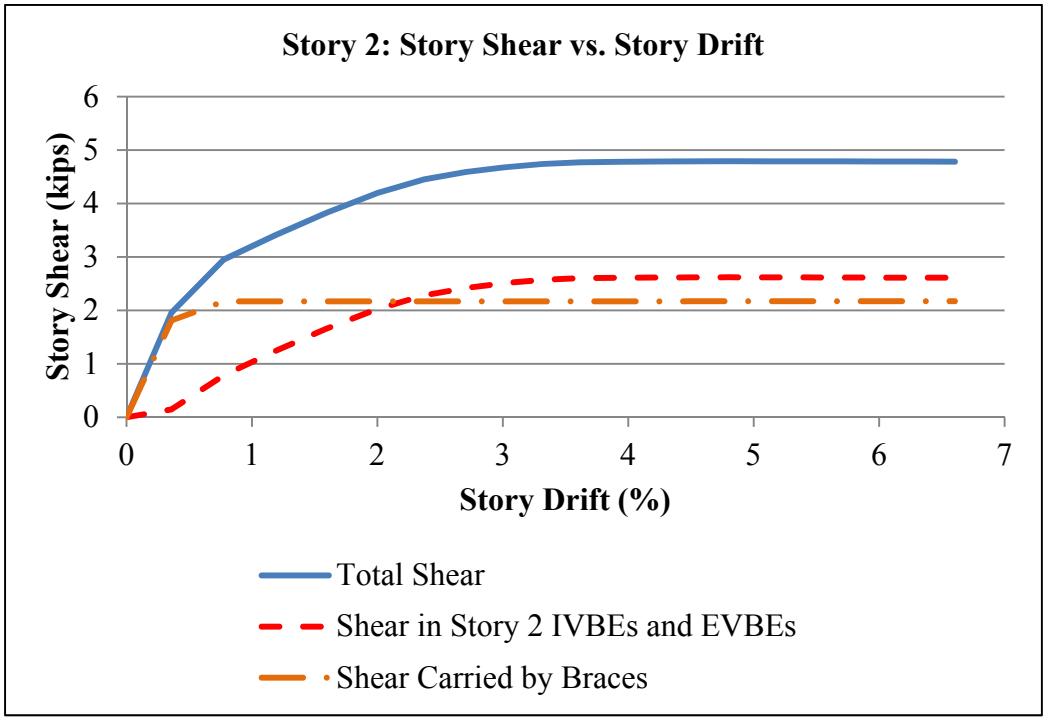

(b)

Figure 4.13 Story Shear vs. Story Drift: (a) Story 1, (b) Story 2, and (c) Story 3

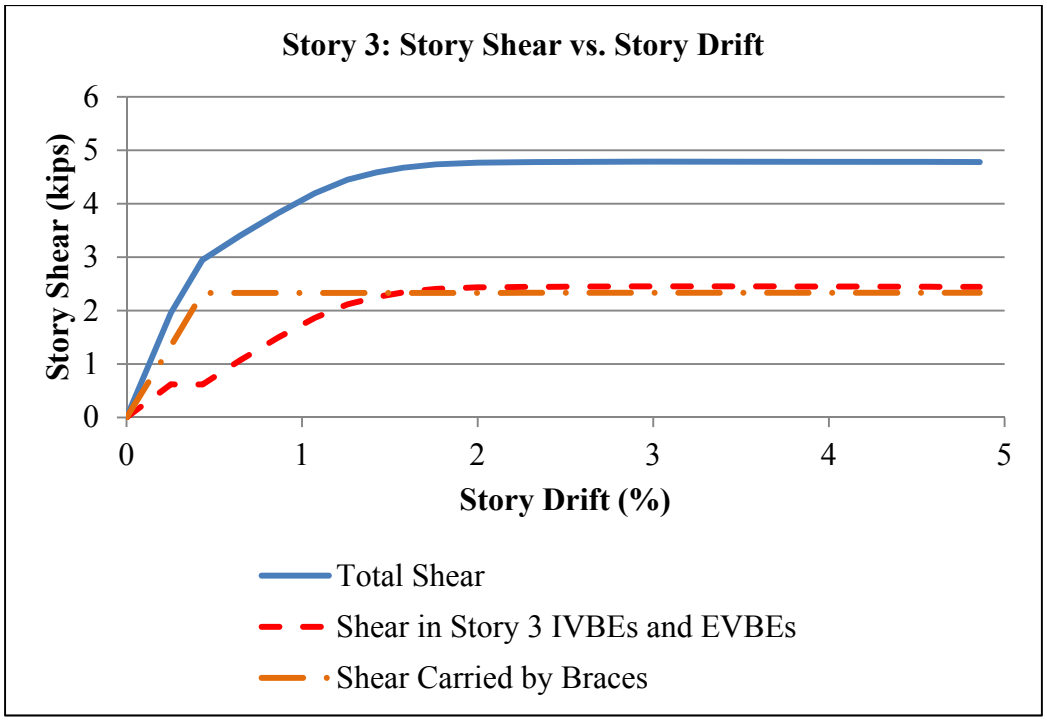

(c)

Figure 4.13 (Cont.)

CHAPTER 5
EXPERIMENTAL PROGRAM

The small-scale SPSW-WC specimen was tested in the 1/5th-scale test setup in the MUST-SIM facility at the University of Illinois at Urbana-Champaign (Figure 5.1), which is part of the Network for Earthquake Engineering Simulation (NEES) program. The 1/5th-scale setup is based on the primary MUST-SIM facility where the large-scale SPSW-WC specimens will be tested.

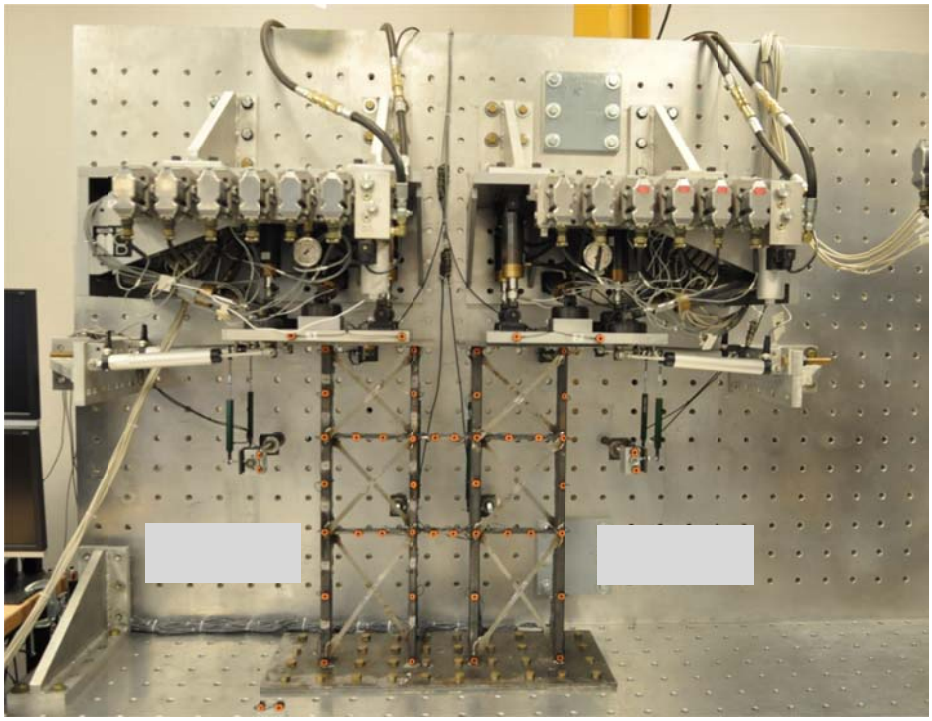

Figure 5.1 1/5th-Scale MUST-SIM Facility

In the small-scale facility, two load and boundary condition boxes (LBCBs) were used to apply a horizontal and vertical force, and bending moment to each pier of the small-scale specimen. Each LBCB consists of six hydraulic actuators, a reaction box and, a loading platform (platen) (Figure 5.2). The six actuators allow for six degrees-of-freedom to be controlled during testing: translations in the x-, y-, and z-directions; and rotations theta-x, theta-y, and theta-z (NEES@Illinois 2013).

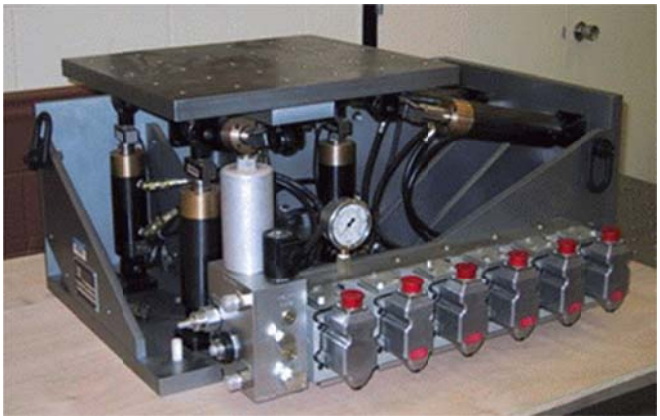

Figure 5.2 1/5th-Scale LBCB (NEES@Illinois 2013)

Referring to Figure 5.3, the two horizontal actuators attached to the far end of the reaction box control translation in the x-direction and rotation about the z-axis (theta-z). The three vertical actuators control translation in the z-direction, and rotations about the x-axis (theta-x) and y-axis (theta-y). One more horizontal actuator behind the three vertical actuators is used to control translation in the y-direction. Each actuator can provide up to a 3 kip force.

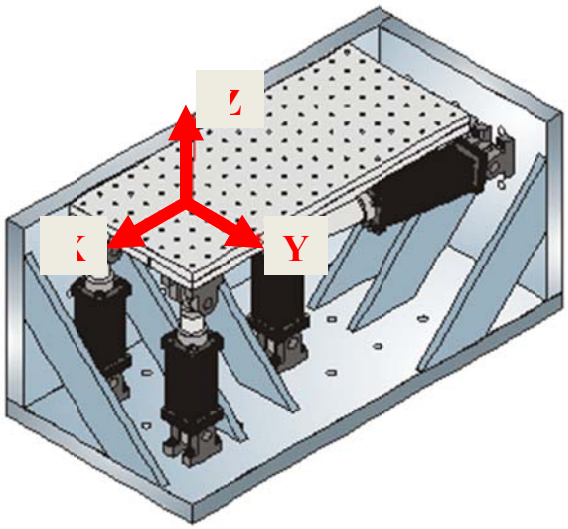

Figure 5.3 1/5th-Scale LBCB (NEES@Illinois 2013)

For the tests on the small-scale specimen, the two LBCBs were attached to the facility's strong wall as shown in Figure 5.1. In Figure 5.4, it may be observed that the top plates of the

specimen were each bolted to the loading platform of each LBCB. The specimen's base plate was bolted to the facility's strong floor (Figure 5.5)

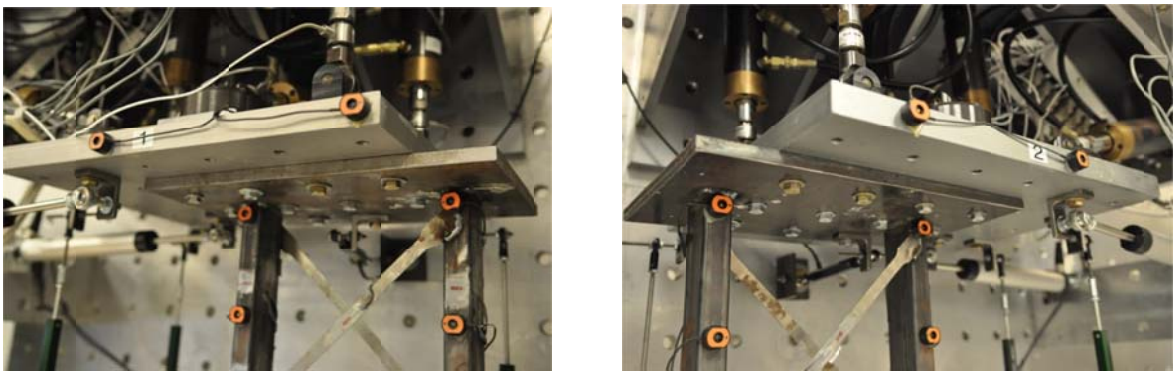

(a)

Figure 5.4 Connection of Specimen's Top Plates to LBCB Loading Platforms: (a) Pier 1, (b) Pier 2

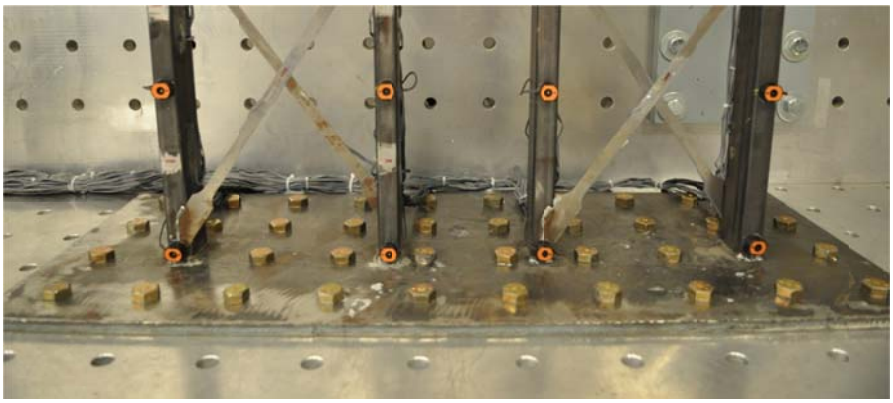

Figure 5.5 Connection of Specimen's Bottom Plate to the Strong Floor

Once the specimen was connected to the LBCB loading platforms and the strong floor, the specimen's control points were determined. Two control points were determined because each pier would be loaded independently by each LBCB. For convenience in the calculation of moments, each control point was established at the point on the bottom of each pier's top connecting plate that coincided with the center of each pier. All rotations and moments commanded to each LBCB were applied at the respective control point (Bletzinger 2012). In the LBCB Operations Manager (OM) setup, a transformation matrix was defined and used to align the coordinate axis originating at the control point of each pier of the specimen with the axis

originating at the corresponding LBCB's motion center (Bletzinger 2012). The LBCB motion center is located at the center of the bottom surface of the loading platform. Thus, because Pier 1 was connected to LBCB 1, a transformation matrix was used to align the coordinate axis originating at Pier 1's control point with the coordinate axis that originates at the motion center of LBCB 1. This was also the case for Pier 2 and LBCB 2.

To resolve the six degrees-of-freedom controlled through each of the LBCBs and provide a measure of elastic deformations in the LBCBs during testing, six external control sensors were used for each LBCB (Figure 5.6). A total of twelve linear potentiometers were used for the external control sensors. In Figure 5.6, the vertical sensors that are highlighted in green measured displacements in the z-direction and rotation about the x- and y-axes. The horizontal sensors that are highlighted in red measured displacements in x and rotation about the z-axis. The sensors that are highlighted in yellow measured displacement in the y-direction. With the linear potentiometers configured in this way, it was possible to determine the difference between the displacement commanded to the LBCBs and what the specimen's actual displacement was (Mock 2012).

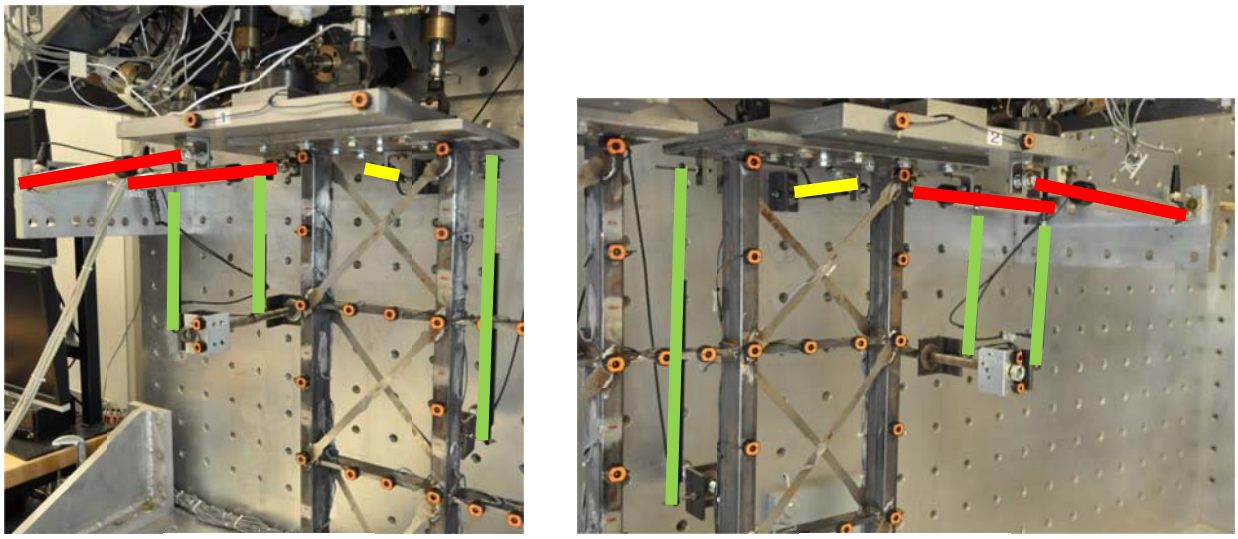

a) **(b)**

Figure 5.6 Locations of Linear Potentiometers: (a) Pier 1, (b) Pier 2

To record the strains in the small-scale specimen's IVBEs, EVBEs, HBEs, CBs, and braces, a total of 72 linear strain gages were attached to the specimen. The layout of the strain

gages is presented in Appendix E. To simulate testing conditions in the large-scale facility, an independent OM system was used to read the strain gage channels, rather than using the same OM system that was used to run the loading protocol. 71 strain gages were connected through breakout boxes to three National Instruments (NI) SCXI-1317 Front-Mounting Terminal Blocks, each with the capacity for 24 strain gage channels (Figure 5.7). Each of these front-mounting terminal blocks was connected to an NI SCXI-1521B input module (Figure 5.8). The input modules were inserted into a twelve-slot NI SCXI chassis (Figure 5.7). Because of a bad channel in one of the SCXI-1317 terminal blocks, a SCXI-1314 terminal block and SCXI-1520 input module were used to connect the remaining strain gage. During the calibration of the strain gages performed before testing, a faulty gage was discovered and noted. The faulty gage was located on the EVBE in the second story of Pier 1.

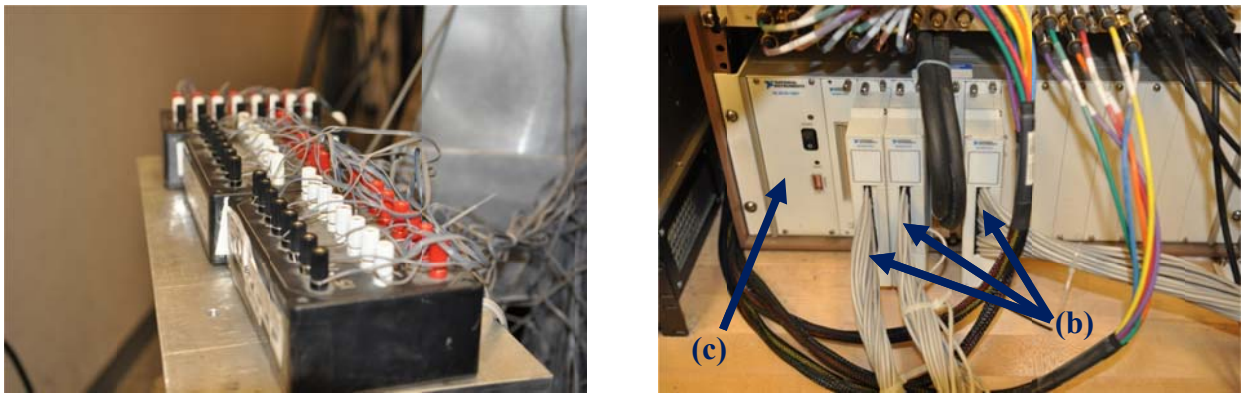

(a)

Figure 5.7 (a) Breakout Boxes, (b) Front-Mounting Terminal Blocks, and (c) Chassis

Figure 5.8 Input Module

A Krypton K600-DMM camera was used to provide another measure of the specimen's displacement (Figure 9). A total of 50 light emitting diodes (LEDs) were placed on the small-scale specimen, reference points, and loading platforms (Figure 5.9). The stationary LEDs (circled in red in Figure 5.9) were used to define a reference frame for the Krypton system. The LEDs on the loading platforms (circled in yellow in Figure 5.9) were used to measure the platforms' displacement. The specimen LEDs were used to measure specimen displacements.

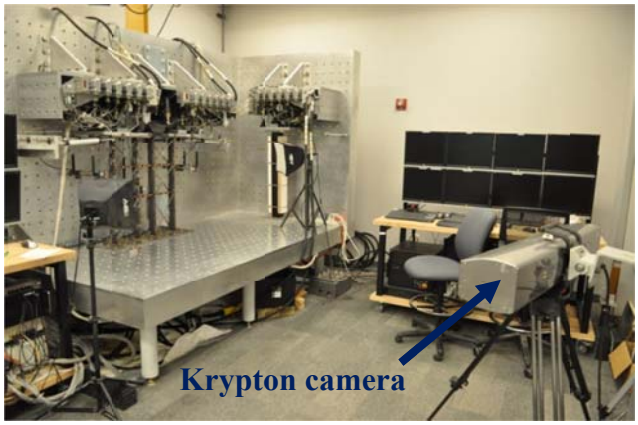

(a)

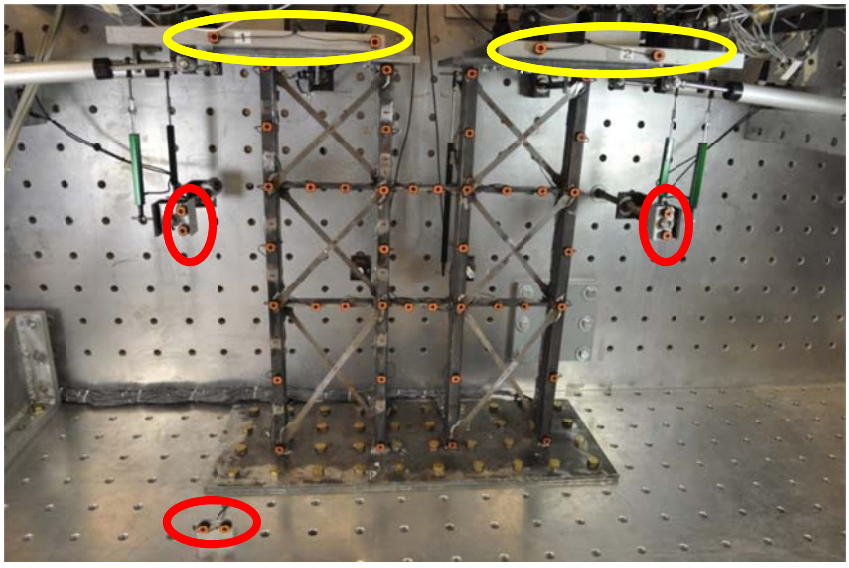

(b)

Figure 5.9 (a) Krypton Camera and (b) LEDs

A fixed camera was used to capture images of the specimen during testing. The camera was configured to take a picture at the end of each completed step. To obtain closer images of any damage, a second camera was used to capture images at the peak displacements as well as zero displacement positions.

The loading protocol consisted of gradually increasing cycles of lateral displacements in the x-direction of the LBCB boxes (Figures 5.10, 5.3). Figure 5.11 shows the roof drift cycles of 0.1%, 0.25%, 0.5%, 1.0%, 1.5%, 2.0%, 2.5%, 3.0%, 3.5%, 4.0%, 4.5%, and 5.0% that were imposed on the specimen. Each cycle was repeated twice up to the 5.0% cycle. The 5.0% cycle was repeated three times until an actuator displacement limit was reached and the specimen had experienced significant strength deterioration.

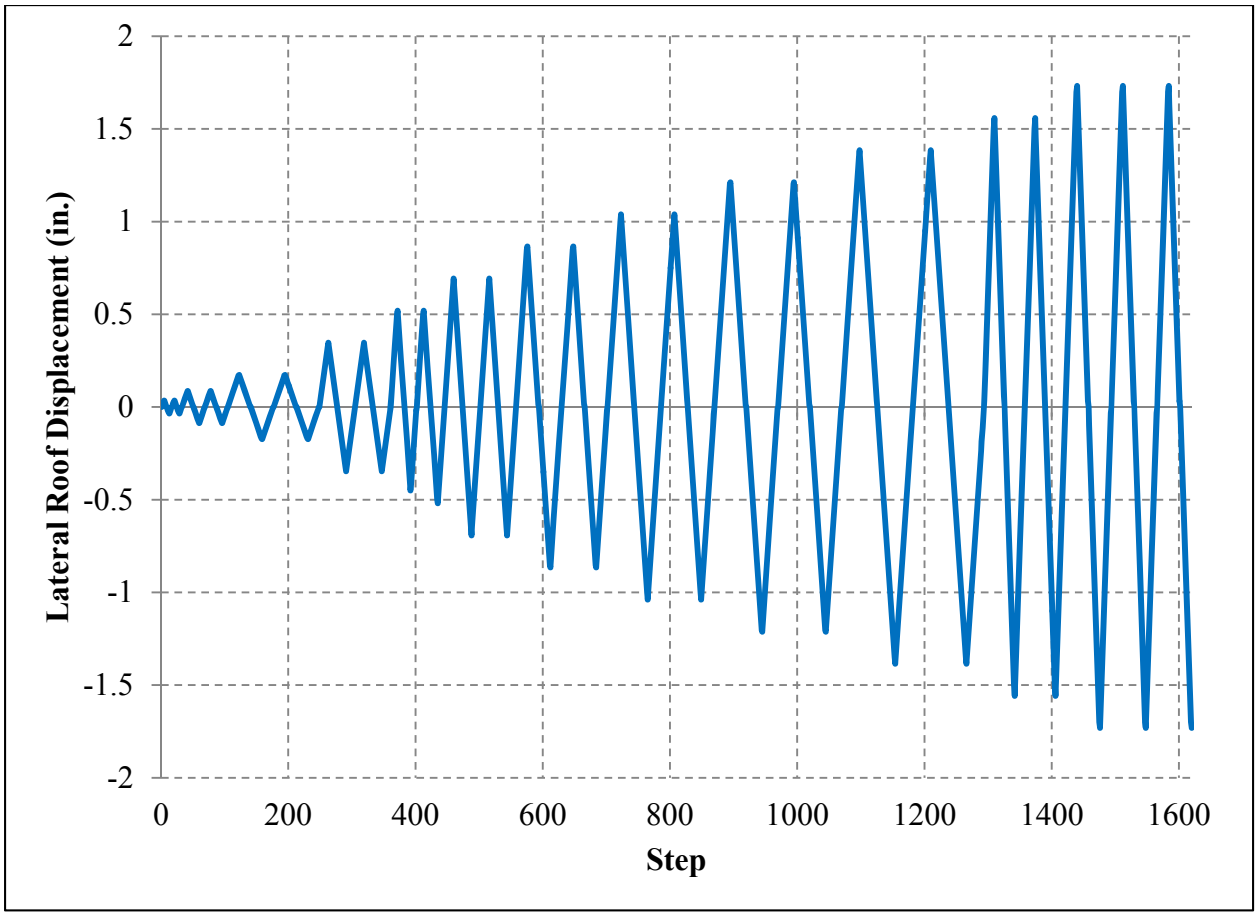

Figure 5.10 Displacement Loading History

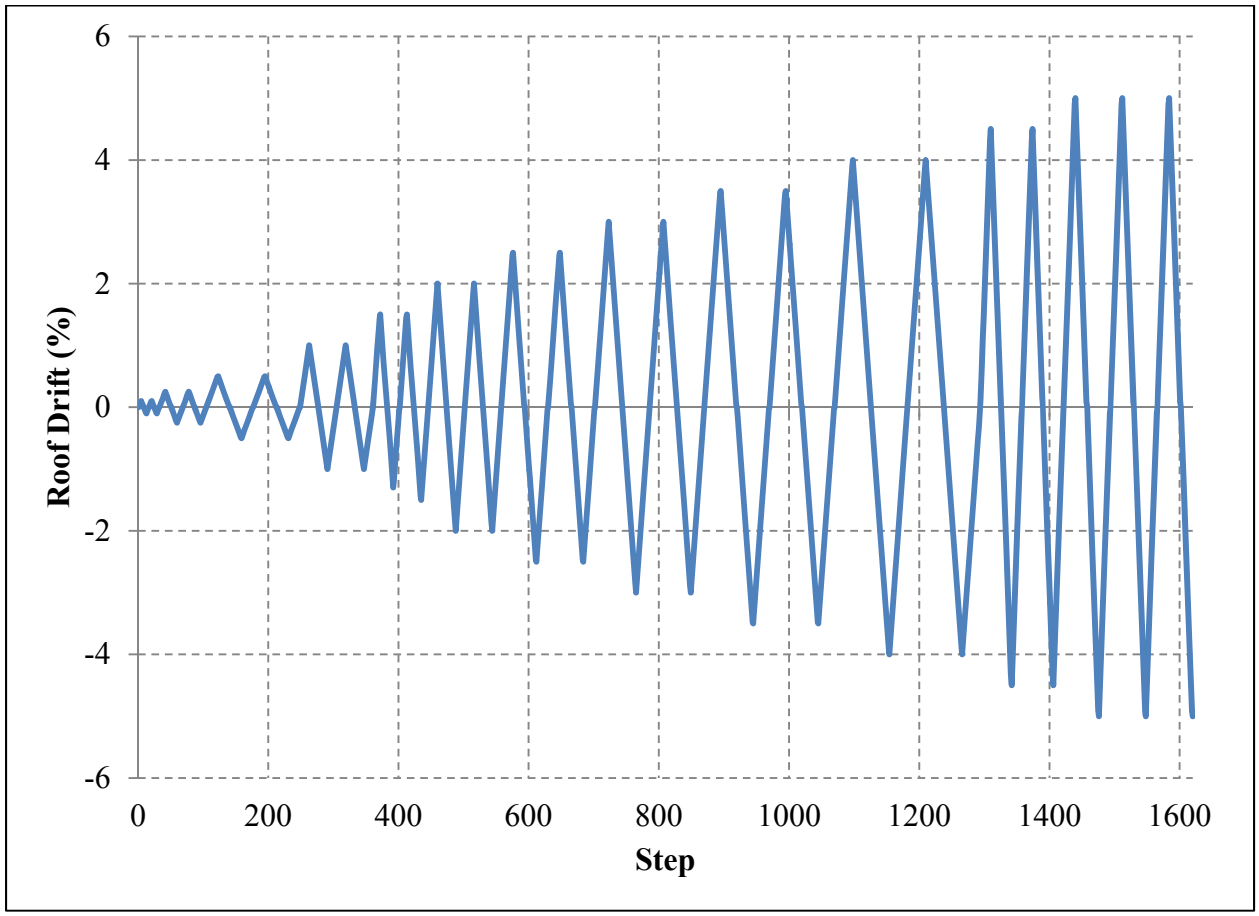

Figure 5.11 Roof Drift Loading History

The control algorithm developed by Daniel J. Borello (personal communication, April 6, 2013) commanded x-displacements and measured the lateral force F_x that was required to achieve the displacement target. The measured F_x was used to calculate the global overturning moment imposed on the specimen and the local moment imposed on each pier (M_{Pier}). The control algorithm was based on making a cut just below the top floor of the third story in the six-story SPSW-WC prototype that the large-scale specimen designs are based on, and on the assumption that the local moment in each pier is equal (Daniel J. Borello, personal communication, April 24, 2013). A distributed lateral load that took into account the inelastic behavior of the structure was applied, and the total overturning moment applied on the bottom three stories of the structure was due to the resultant of the portion of the distributed lateral load above the cut acting at an

effective height, $\bar{h}$, from the cut. At the cut, the coupling mechanism for resisting a portion of the global overturning moment was formed by the axial forces in the piers, so the degree of coupling (DC) was calculated using the following:

$$DC = \frac{P(e+L)}{M_{Total}} \tag{5.1}$$

$$M_{Total} = \bar{h}F_x \tag{5.2}$$

In the above equations, P is the axial force in a pier, e is the length of the CBs, L is the bay width, $\bar{h}$ is the effective height above the cut, and V is the resultant of the portion of the lateral force distribution above the cut. Combining equations 5.1 and 5.2 and solving for P gives:

$$P = \frac{\bar{h}F_x \times DC}{e+L} \tag{5.3}$$

To determine the value of M_{Pier}, it was known that the total resisting moment at the cut consisted of M_{Pier} for each pier and the moment ($P(e+L)$) due to the coupling mechanism:

$$M_{Total} = 2M_{Pier} + P(e+L) = 2M_{Pier} + M_{Total}DC \tag{5.4}$$

The final relation in equation 5.4 results after substituting equation 5.3 for P. Solving for M_{Pier} gives the following:

$$M_{Pier} = \frac{M_{Total}(1-DC)}{2} = \frac{\bar{h}F_x(1-DC)}{2} \tag{5.5}$$

The final relation in 5.5 results after substituting equation 5.2 for M_{Total}. Hence, the control algorithm is based on equation 5.3 for calculating the pier axial forces that induce the global overturning moment resistance due to coupling and 5.5 for calculating the local pier moments. The DC values are known from the large-scale specimen designs, and F_x is the measured lateral force required to reach a given displacement target.

CHAPTER 6
EXPERIMENTAL RESULTS

In this chapter, a summary of the test on the small-scale SPSW-WC specimen is provided. Important observations made during testing are discussed as well. Test results are presented and discussed.

6.1 Summary and Observations

Up until step 393 of the test (negative peak of the first 1.5% roof drift cycle), the x-displacement was commanded by the loading protocol discussed in Chapter 5 and the lateral force F_x required to impose the displacement target was measured. The measured F_x was then used to calculate the global overturning moment on the specimen, as well as the local moments imposed on the individual piers. A vertical force F_z was commanded to each LBCB to impose the global overturning moment on the specimen in conjunction with gravity loads. The moments and gravity load represented the actions of the upper stories of a six-story building on its first three stories during an earthquake.

A comparison of the strain gage step data with the roof drift loading history showed that all of the braces experienced first full yield between the drift cycles of 0.5% and 1.0%. This explains the reason for the noticeable plastic deformations beginning relatively early during the test.

Figure 6.1 Brace Deformations at End of Second 0.5% Drift Cycle

At step 393, which occurred while the specimen approached the negative peak of the first 1.5% drift cycle, the tension force limit in one of the z-direction actuators was reached in LBCB 2 (the LBCB connected to Pier 2 of the specimen). At this point, a modified loading protocol was used that continued to command x-displacements, but instead of calculating and commanding new pier moments and F_z at each loading step, the moments were commended to be zero and F_z was commanded at a constant value. Hence, the test became a constant axial load plus cyclic horizontal shear.

During step 608 (approaching the negative peak of the first 2.5% drift cycle), a low pinging sound was heard from the specimen. More pings were heard during subsequent steps. At step 775 (returning from the negative peak of the first 3.0% drift cycle), significant plastic deformations were observed in the front and back braces at all stories (Figure 6.2). At the first story of piers 1 and 2, the front and back braces came into contact because of their significant out-of-plane deformations.

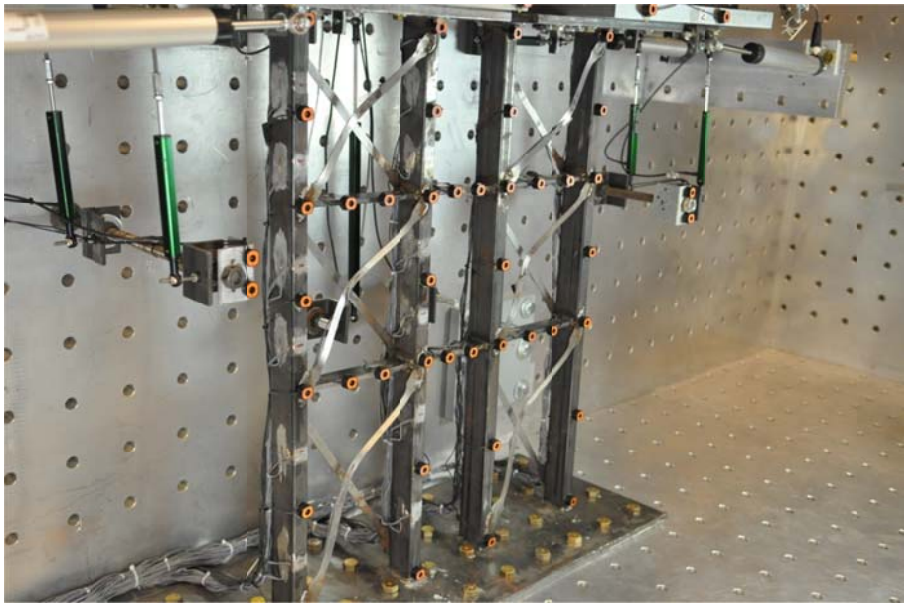

Figure 6.2 Plastic Deformations in Braces during 3.0% Drift Cycle

At step 1154 (negative peak of a 4.0% drift cycle), in addition to the significant plastic deformation in the braces, a base weld fracture along the outside flange of the Pier 2 EVBE was observed (Figure 6.3). The pinging sounds that had been heard were attributed to the development of this partial weld fracture.

Figure 6.3 Partial Fracture at Base Weld of Pier 2 EVBE

At the end of step 1294 (end of the 4.0% drift cycles), the loading protocol was updated to perform larger displacement increments of 0.1 in. All other control parameters remained the same. At step 1476 (at the negative peak of a 5.0% drift cycle), complete fracture of the base weld on the EVBE of Pier 2 was observed (Figure 6.4). In addition to this complete fracture, partial base weld fractures were observed at the external flange of the Pier 1 IVBE and internal flange of the Pier 1 EVBE (Figure 6.5). A partial weld fracture was also observed in the Pier 2 IVBE base weld. As the test progressed, these fractures grew, but complete fractures did not develop at these welds.

Figure 6.4 Complete Fracture of Pier 2 EVBE Base Weld

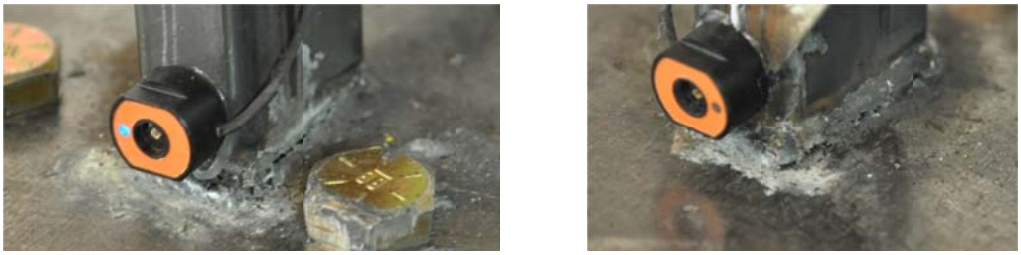

(a) **(b)**

Figure 6.5 Partial Base Weld Fractures at Pier 1 (a) IVBE and (b) EVBE

The test was ended on step 1620 (at the negative peak of a 5.0% drift cycle) when the displacement limit of one of LBCB 2's z-actuators was reached. Because of the complete fracture of the base weld of the Pier 2 EVBE, the tendency of the specimen to overturn caused significant rotation in the loading platform about the y-axis of LBCB 2. This significant rotation resulted in the z-actuator's displacement limit being reached. When the specimen was brought to a position of zero x-displacement significant plastic deformations in the braces were observed (Figure 6.6).

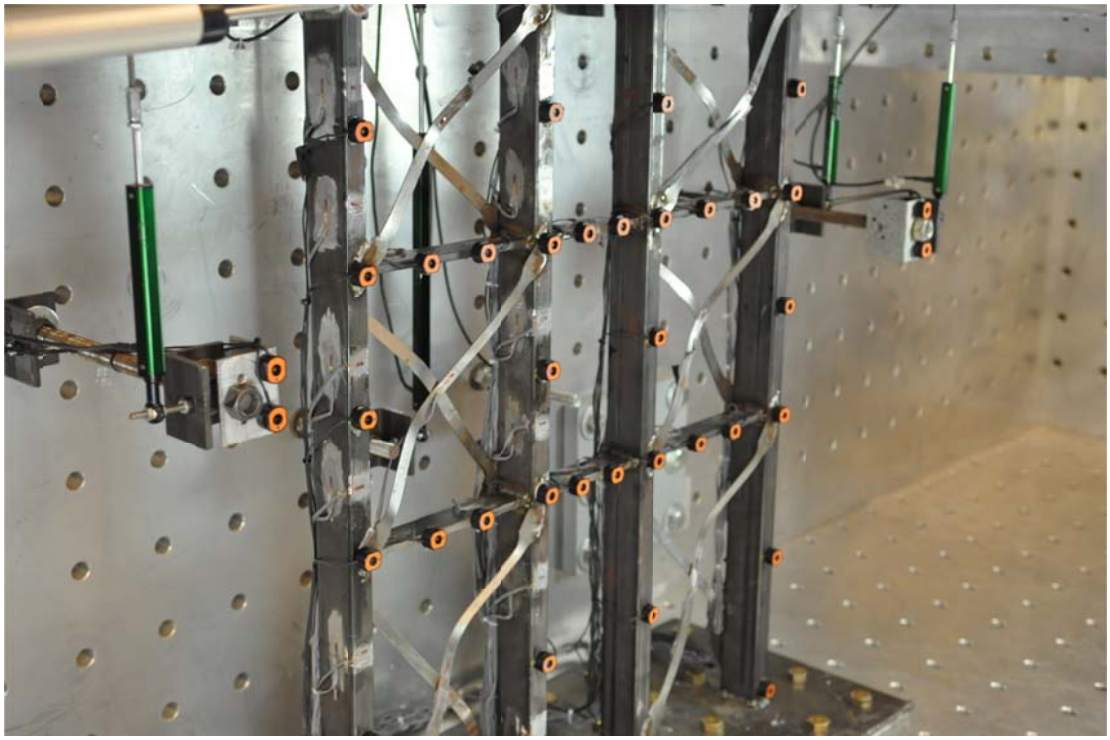

Figure 6.6 Plastic Deformations in Braces at End of Test

6.2 Test Results

The plot of Base Shear vs. Average Lateral Roof Displacement is presented in Figure 6.7. The average lateral displacement of the top floor was calculated by averaging the lateral displacements of the top floor of each pier. The plot shows that the specimen achieved an ultimate strength of approximately 3.5 kips at a roof drift of approximately 3.0%. The specimen also sustained drift levels of up to 5%, reaching a maximum top story lateral displacement of +/-

1.73 in. Pinching behavior is evident in the hysteresis loops, but the behavior was stable and strength and stiffness degradation was gradual. The energy that the system did dissipate was due in large part to the satisfactory behavior of the braces, which were able to sustain large plastic deformations without failure. Yielding in the HBEs and CBs also contributed to the specimen's energy dissipation. Figure 6.7 also shows that the behavior of the specimen was stable, with no sudden and significant reductions in strength or stiffness during most cycles of roof displacements. However, a significant and sudden reduction in strength and stiffness can be observed during the negative lateral displacement of one of the final 5.0% drift cycles. This is attributed to the complete fracture of the Pier 2 EVBE base weld discussed above.

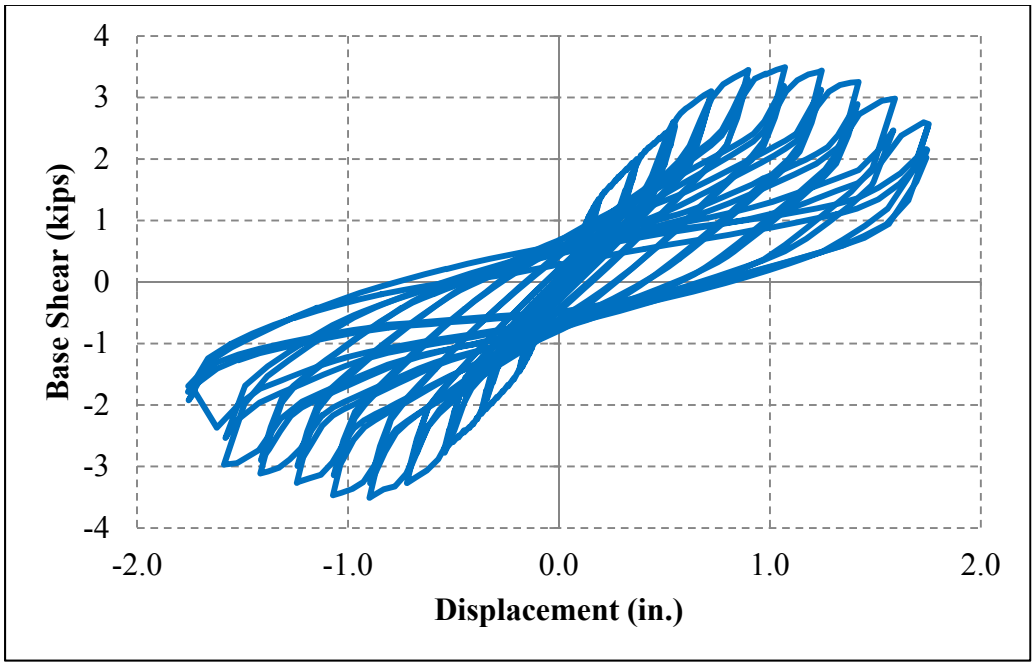

Figure 6.7 Base Shear vs. Average Lateral Roof Displacement

An analysis of the strain gage data showed that most of the extreme top and bottom fibers at strain gage locations in the HBEs and CBs experienced first yield relatively early in the test. Between steps 460 and 610, corresponding to displacement cycles with roof drifts of 2.0% and 2.5%, respectively, first yield occurred in the CBs. Between steps 460 and 575, corresponding to cycles with roof drifts of 2.0% and 2.5%, respectively, first yield occurred in the HBEs. Yielding was not observed at any of the instrumented locations on the EVBEs and IVBEs. Yielding was

observed in the braces at relatively lower drift levels than the CBs and HBEs. Brace yielding was observed as early as the 0.5% drift cycles.

The story shear vs. story drift responses for Pier 1 and Pier 2 are shown in Figure 6.8 and Figure 6.9, respectively. Since only a concentrated lateral load was applied to the top of each pier, the story shear was constant over the height of each pier. Story drifts were calculated using the step data obtained from the Krypton camera measurements. For each story of a pier, the average horizontal displacement of the LEDs near the joints at the top of the story was calculated. The same was done with the LEDs on the joints at the bottom of the story. The displacement of the top of the story relative to the bottom of the story was taken as the difference between the two average values. The story drift was calculated using this relative displacement.

In Figures 6.8 and 6.9, the plots of story shear vs. story drift reflect the effect of the complete base weld fracture at the Pier 2 EVBE. In the plot for Story 1 of Pier 1, it is observed that at a drift of about -6.0%, there is a sudden increase in the shear carried by this story. This jump occurs at the same time during which the base weld fracture occurs. Thus, the failure of the base weld in Pier 2 caused a drop in the capacity of Pier 2, and the lateral load that was shed was partially picked up by Pier 1. Similar behavior is observed in the second and third stories of Pier 1. Although the piers were nominally identical, Pier 2 was apparently stiffer than Pier 1. Consequently, Pier 2 attracted more of the applied lateral load as shown in Figure 6.9. Maximum story shears in Pier 2 were approximately 2.0 kips, while those in Pier 1 were about 1.5 kips.

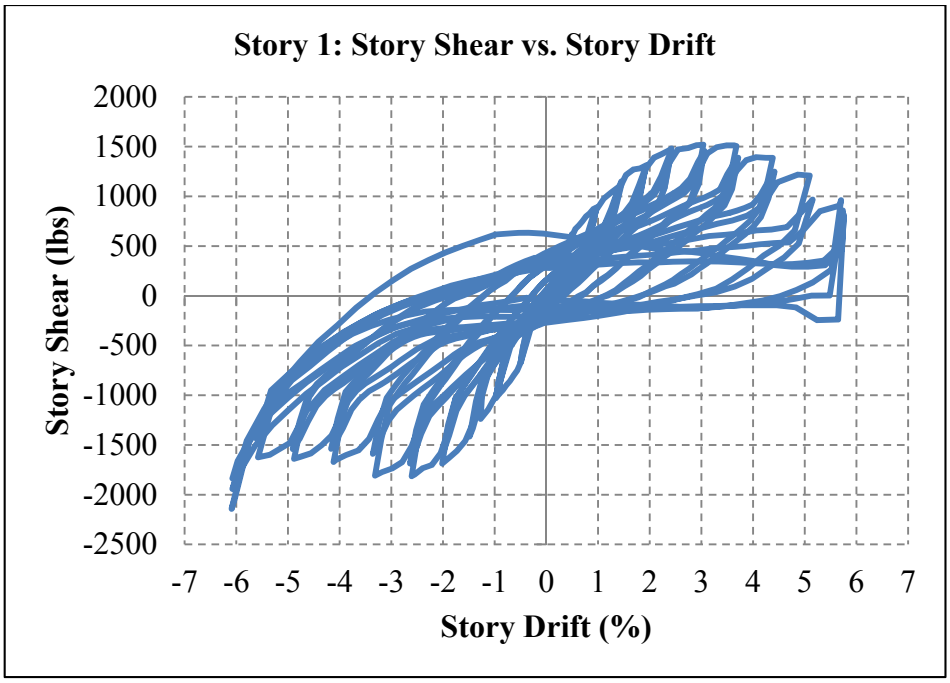

(a)

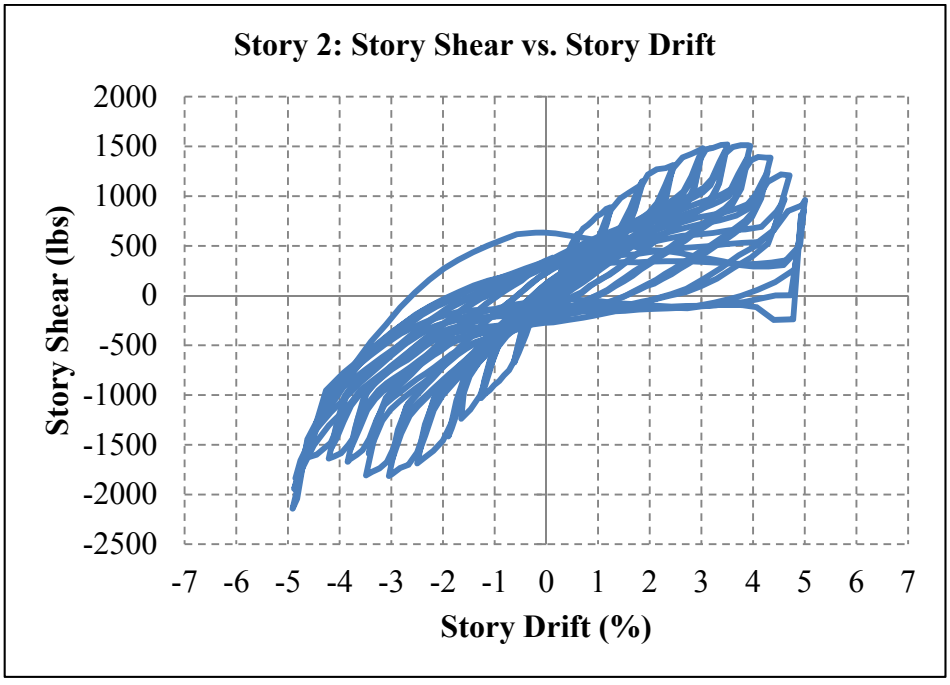

(b)

Figure 6.8 Story Shear vs. Story Drift in Pier 1: (a) Story 1, (b) Story 2, and (c) Story 3

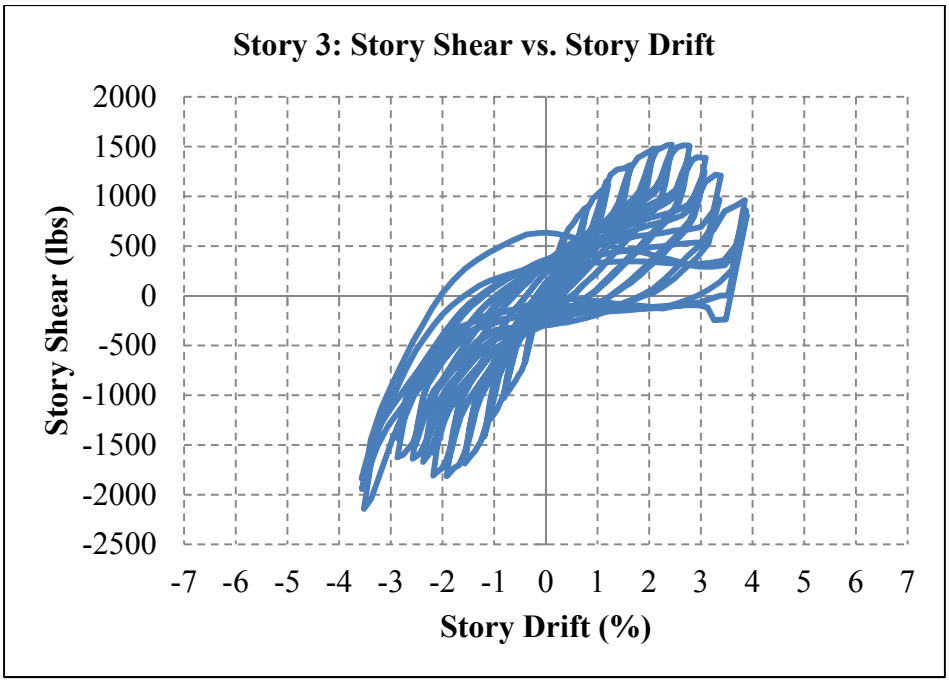

(c)

Figure 6.8 (Cont.)

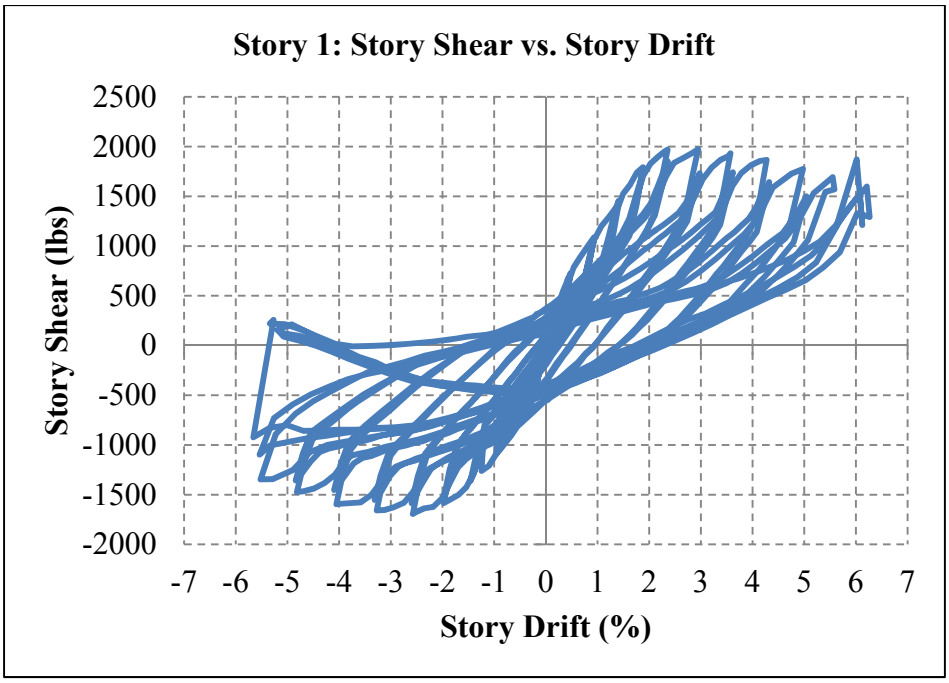

(a)

Figure 6.9 Story Shear vs. Story Drift in Pier 2: (a) Story 1, (b) Story 2, and (c) Story 3

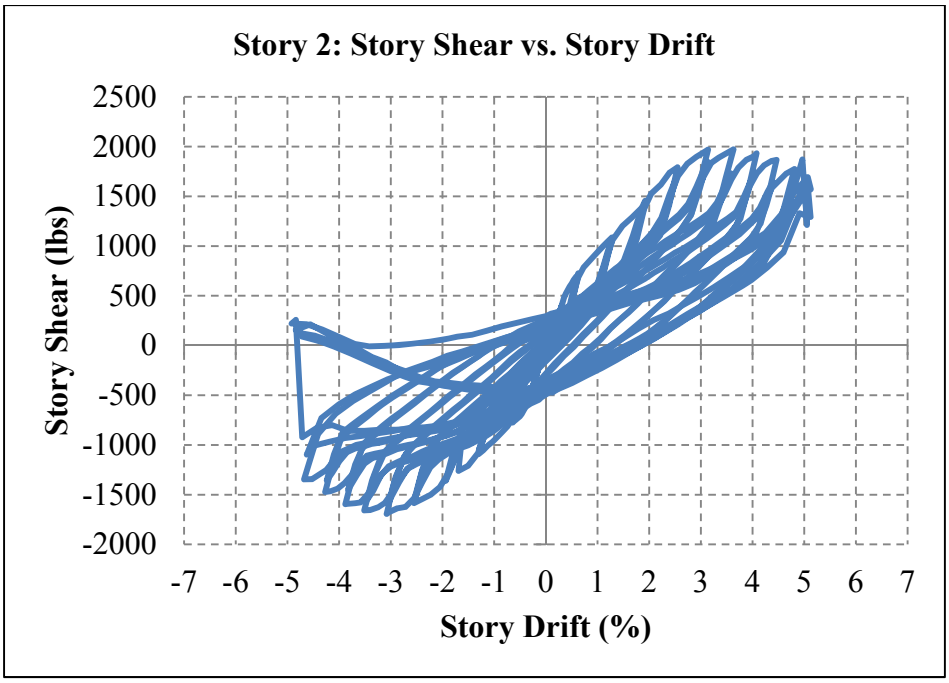

(b)

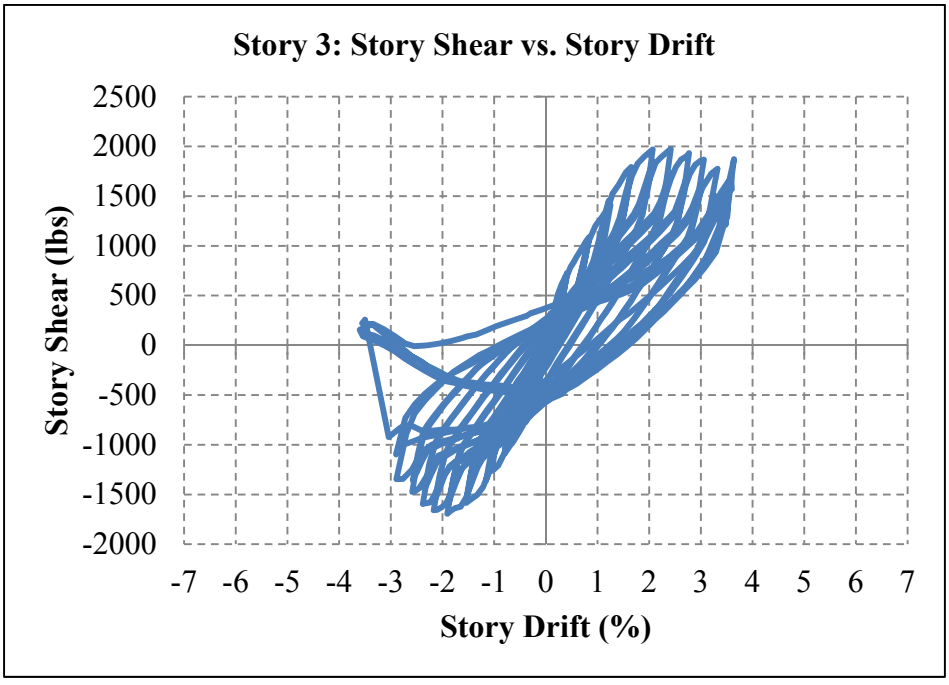

(c)

Figure 6.9 (cont.)

Figure 6.10 compares the experimental data to the analytical and numerical predictions. As illustrated in this figure, the initial stiffness and ultimate strength of the small-scale specimen in the experiment differ appreciably from the predictions. The analytical and numerical models overestimated the ultimate strength when compared to the strength observed in the test results. The numerical models also showed a higher initial stiffness than that of the actual specimen. The ultimate strength displayed by the small-scale specimen was approximately 3.5 kips, while strengths of 4.78 kips, 4.8 kips, and 5.5 kips were estimated by the OpenSees model, the plastic analysis, and the SAP2000 model, respectively. As mentioned previously, the SAP2000 model used plastic hinges to capture the nonlinear behavior due to yielding. Compared to the OpenSees model, this provided an approximation that was stronger. The OpenSees model used fiber-based elements for the IVBEs, EVBEs, HBEs, and CBs that accounted more accurately for the spread of plasticity. Thus, the OpenSees model was deemed to provide a better approximation of the actual behavior of the specimen under a lateral load.

The initial elastic stiffness of the numerical models was about 19.5 kips/in, while the elastic stiffness of the test specimen was approximately 7.5 kips/in. This resulted in a difference of about 62% relative to the numerical result. The low initial stiffness of the specimen observed during the test is likely due to initial imperfections in the braces. Before testing began, it was observed that the braces at some stories had an initial out-of-plane imperfection because their lengths were greater than the distance between the two points that the braces were welded to. This initial "slack" in the braces at some stories reduced the specimen's initial stiffness because at those stories larger displacements had to be applied before the braces were put into tension. The early pings heard during testing may have been the result of the initiation of small fractures in the base welds of the IVBEs and EVBEs. These small fractures may have partially reduced the ultimate strength of the specimen. In addition, strain gage data indicate that plastic hinges assumed at the base and top of the IVBEs and EVBEs did not form. In light of the experimental results, the analytical model was modified assuming that the tops and bottoms of the IVBEs and EVBEs were pure pins. Based on this modified collapse mechanism, the plastic analysis estimated an ultimate strength of 2.3 kips, which was below the strength observed during the test. This pinned boundary condition case is extreme since there was some rotational restraint provided by the welds at these locations, so the plastic strength values of 4.8 kips and 2.3 kips reasonably bracket the experimental result. The experimental results indicate that the base

connections were not capable of developing the plastic hinges in the IVBEs and EVBEs. Figure 6.11 shows the specimen at the moment it achieved its ultimate strength.

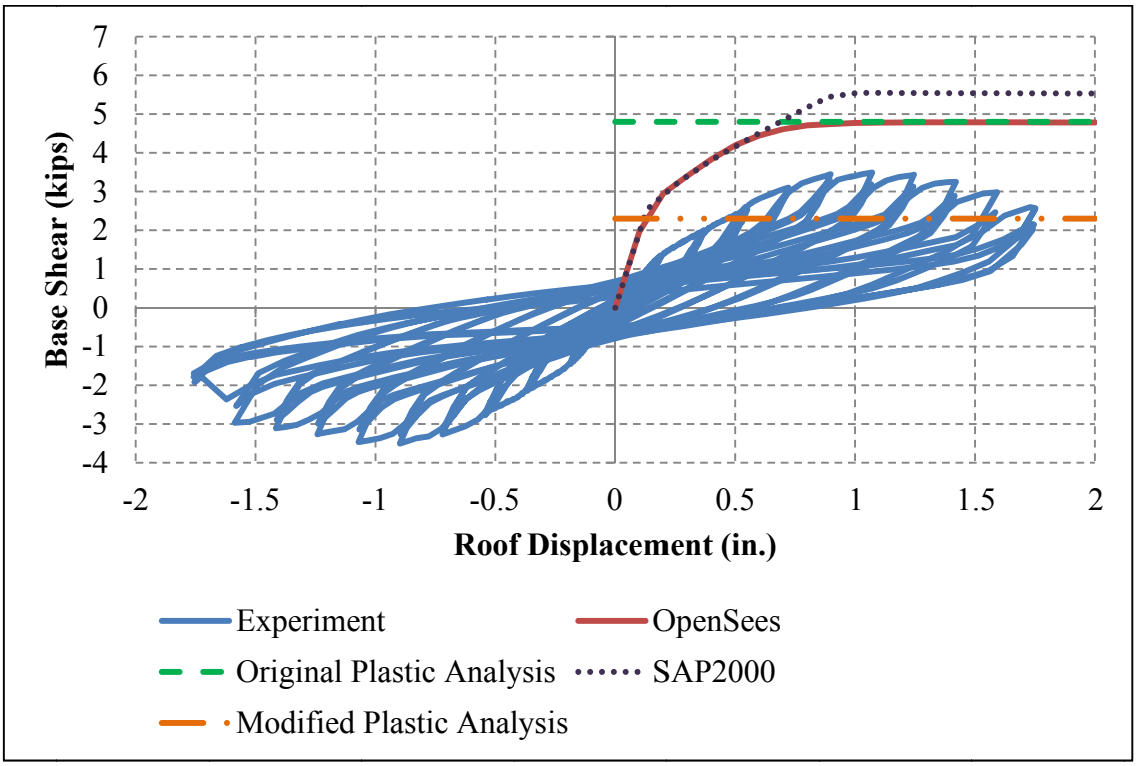

Figure 6.10 Comparison of Specimen's Ultimate Strength

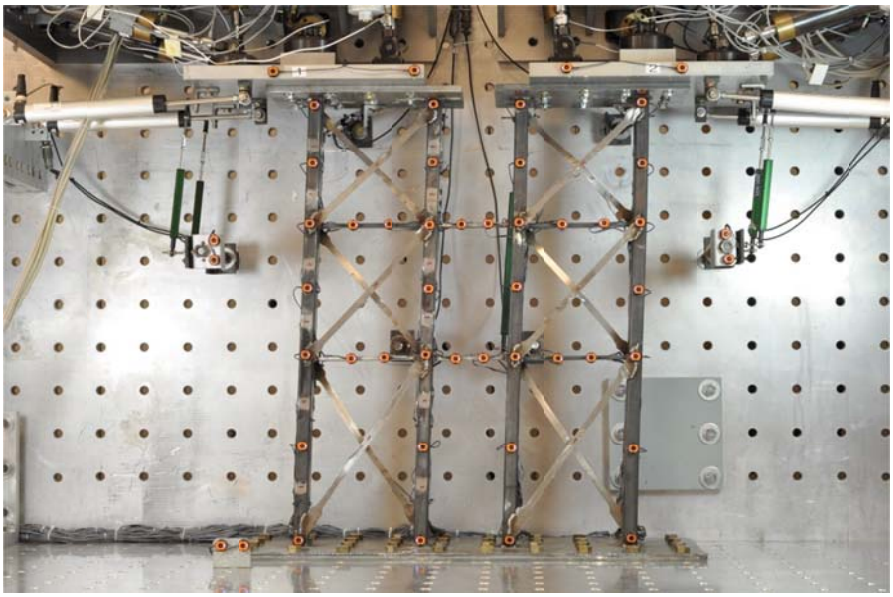

Figure 6.11 Specimen at Ultimate Strength

CHAPTER 7
SUMMARY AND CONCLUSIONS

In this chapter, summaries of the design of the small-scale SPSW-WC specimen and the experimental program are provided. A summary of the findings from the analytical, numerical, and experimental investigations is provided. The analytical and numerical results are compared to the experimental results, and the similarities and differences are discussed.

7.1 Small-Scale SPSW-WC Specimen Design

A small-scale, three-story SPSW-WC specimen was designed based on the large-scale FLEX SPSW-WC specimen with flexural yielding dominated coupling beams (CBs) that will be tested at the University of Illinois. Dimensional analysis and similitude were used to scale down the large-scale specimen. A hollow structural section was chosen for the internal and external vertical boundary elements (IVBEs and EVBEs, respectively) and solid rectangular sections were chosen for the horizontal boundary elements (HBEs) and CBs. The most feasible way to represent the web plates at each story was to use diagonal braces on the front and back of the small-scale specimen's piers on all stories. All of the connections between the boundary elements and the braces were made with fillet welds.

7.2 Analytical and Numerical Modeling

Based on a plastic analysis by the kinematic method, the ultimate strength of the small-scale SPSW-WC specimen was estimated. The analysis was based on an assumed collapse mechanism that followed the basis of the capacity-based design methodology adopted for the SPSW-WC. The collapse mechanism consisted of plastic hinges at the base and top of each IVBE and EVBE, and plastic hinges at the ends of the HBEs and CBs. Additionally, the braces on all stories were assumed to have yielded in tension. Based on this analysis, the ultimate strength of the specimen was estimated at 4.8 kips.

In addition to the analytical model, numerical models of the specimen were developed in SAP2000 and OpenSees. The SAP2000 model used frame elements to model the IVBEs,

EVBEs, HBEs, CBs, and braces. Under the assumption that the braces would provide negligible compressive strength, only the braces that would be in tension under an applied lateral load were modeled. The supports at the specimen's base were modeled as fixed. Plastic hinges were added along the frame elements to capture nonlinear behavior in the system due to yielding of cross-sections. A nonlinear static pushover analysis was performed using this model, and the system's ultimate strength was estimated as 5.5 kips.

In the OpenSees model, fiber sections were defined for the IVBEs, EVBEs, HBEs, and CBs. These elements were modeled with force-based beam-column elements. Truss elements were used to model the braces that would be in tension under an applied lateral load. A nonlinear static pushover analysis was performed on the model to estimate the specimen's ultimate strength. The simulation estimated the strength at 4.78 kips, which agreed with the strength estimated using the plastic analysis. The agreement between the plastic analysis and OpenSees results validated the use of plastic analysis and the assumed collapse mechanism for determining the ultimate strength of a SPSW-WC. The OpenSees model indicated that a greater portion of the total story shear was carried by frame action than was carried by the braces.

7.3 Experimental Results

A displacement-controlled test was conducted on the small-scale specimen to investigate its behavior in preparation for the tests on large-scale specimens. The small-scale test was conducted in the reduced-scale NEES MUST-SIM facility at the University of Illinois. In addition to the force and displacement output from the load and boundary condition boxes (LBCBs) that were used to conduct the experiments, strain gages, linear potentiometers, and a Krypton system were used to record the response of the specimen.

The loading protocol consisted of gradually increasing cycles of lateral displacements. A control algorithm imposed displacement and measured the lateral force required to achieve a given displacement target. The measured lateral force was used to calculate the desired global overturning moment on the specimen and the moment on each pier. The specimen was tested successfully up to a roof drift of 5.0%.

During the test, the braces performed satisfactorily, yielding between story drifts of 0.5% and 1.0%, and sustaining large plastic deformations without fracture. Based on the strain gage

step data, first yield occurred in the HBEs and CBs between story drifts of 2.0% and 2.5%. Strain gage data indicate that yielding did not occur in the IVBEs or EVBEs.

The global lateral force vs. roof displacement plot showed that the specimen achieved an ultimate strength of approximately 3.5 kips. The hysteretic loops indicated pinched behavior due to tension-only brace response. However, the specimen's behavior during the majority of the displacement cycles was relatively stable, with strength and stiffness degradation occurring gradually. It was only during a 5.0% drift cycle near the end of the test that a significant and sudden drop in strength was observed. This was the result of the complete fracture of the base weld on the EVBE of Pier 2. The test was concluded when a vertical actuator displacement limit was reached in the LBCB connected to Pier 2 due to the significant rotation in the loading platform that resulted from the fracture of the base weld.

7.4 Comparison of Analytical, Numerical, and Experimental Results

The specimen's ultimate strength observed during testing was lower than the values predicted by numerical and analytical models. The ultimate strength of the small-scale specimen was 3.5 kips, while a strength of 4.8 kips was predicted using an OpenSees model and simple plastic analysis. This discrepancy indicates that the collapse mechanism in the models may not have formed in the small-scale specimen during testing. Based on strain gage data, it appears likely that the VBEs did not develop plastic hinges at the top and bottom of the structure. A modified plastic analysis was conducted in which pinned connections were assumed at the tops and bottoms of the EVBEs and IVBEs. The resulting plastic strength was 2.3 kips, which lies below the ultimate strength of 3.5 kips observed in the experiment and the original calculated plastic strength of 4.8 kips. The original plastic strength of 4.8 kips and the modified plastic strength of 2.3 kips reasonably bracket the experimental result.

In addition to the strength discrepancy between the models and the experiment, the experimental stiffness was also much lower than the predicted stiffness. This difference is attributed to initial brace imperfections.

The successful test on the small-scale SPSW-WC validated the control algorithm that will be used in the large-scale SPSW-WC tests. Although pinched, the hysteretic behavior of the small-scale specimen was similar to the hysteretic behavior of past tests on large-scale SPSW

specimens. The small-scale test conceptually demonstrated the coupling mechanism that will be extensively explored in the large-scale tests.

REFERENCES

American Institute of Steel Construction (AISC) (2005). *AISC Seismic Provisions for Structural Steel Buildings (AISC 341-05)*, AISC, Chicago, IL.

American Institute of Steel Construction (AISC) (2010). *AISC Seismic Provisions for Structural Steel Buildings (AISC 341-10)*, AISC, Chicago, IL.

AISC (2008). *Steel Construction Manual, Thirteenth Edition*. AISC, Chicago, IL.

Berman, J., and Bruneau, M. (2003). "Plastic Analysis and Design of Steel Plate Shear Walls." *Journal of Structural Engineering*, 129, 1448-1456.

Berman, J.W., and Bruneau, M. (2008). "Capacity Design of Vertical Boundary Elements in Steel Plate Shear Walls," *Engineering Journal*.

Berman, J.W., Lowes, L.N., Okazaki, T., Bruneau, M., Tsai, K-C., Driver, R.G., and Sabelli, R. (2008). "Research Needs and Future Directions for Steel Plate Shear Walls." *Structures Congress 2008*, American Society of Civil Engineers (ASCE), Vancouver, Canada.

Bletzinger, M. (2012). *LBCB Operations Manager – User Manual*, University of Illinois at Urbana-Champaign.

Borello, D.J., and Fahnestock, L.A. (2011). "Design and Testing of Coupled Steel Plate Shear Walls," *Structures Congress 2011*, ASCE, Las Vegas, NV, 736-747.

Borello, D.J. and Fahnestock, L.A. (2012a). "Behavior and mechanisms of steel plate shear walls with coupling," *Journal of Constructional Steel Research*, 74, 8-16.

Borello, D.J., and Fahnestock, L.A. (2012b). "Seismic Design and Analysis of Steel Plate Shear Walls with Coupling," *Journal of Structural Engineering*.

Bruneau, M., Berman, J., Lopez-Garcia, D., and Vian, D. (2005). "Steel Plate Shear Wall Buildings: Design Requirements and Research," *Proceedings of 2005 North American Steel Construction Conference*, Montreal, Canada.

Bruneau, M., and Sabelli, R. (2006). *Design Guide 20 / Steel Plate Shear Walls,* AISC.

Caccese, V., Elgaaly, M., and Chen, R. (1993). "Experimental Study of Thin Steel-Plate Shear Walls Under Cyclic Load," *Journal of Structural Engineering*, 119, 573-587.

Canadian Standards Association. (1994). *Design of Concrete Structures (A23.3)*, Canadian Portland Cement Association, Ontario, Canada.

Driver, R.G., Kulak, G.L., Kennedy, D.J.L., and Elwi, A.E. (1998). "Cyclic Test of Four-Story Steel Plate Shear Wall," *Journal of Structural Engineering*, 124, 112-120.

Federal Emergency Management Agency (FEMA) (2000). *State of the Art Report on Systems Performance of Steel Moment Frames Subject to Earthquake Ground Shaking, FEMA-355C*, SAC Joint Venture.

Harries, K.A., Moulton, J.D., and Clemson, R.L. (2004). "Parametric study of coupled wall behavior – implications for the design of coupling beams," *Journal of Structural Engineering*, 130, 480-488.

Li, C-H., Chang, J-T., Tsai, K-C., and Lin, C-H. (2011). "Recent Experimental Researches on Steel Plate Shear Walls in NCREE." *Structures Congress 2011*, ASCE, Las Vegas, NV, 724-735.

Lin, C-H., Tsai, K-C., Qu, B., and Bruneau, M. (2010). "Sub-structural pseudo-dynamic performance of two full-scale two-story steel plate shear walls," *Journal of Constructional Steel Research*, 66, 1467-1482.

Mock, A. W. (2012). *Development of Bi-Directional Loading Protocol for Large Scale C-Shaped Wall Testing*, University of Illinois at Urbana-Champaign.

Munson, B.R., Young, D.F., Okiishi, T.H. (2006). "Similitude, Dimensional Analysis, and Modeling." *Fundamentals of Fluid Mechanics*, *5th Edition*, John Wiley & Sons, Inc., Hoboken, NJ, 346-390.

NEES @ Illinois. "MUST-SIM Overview." <http://nees.uiuc.edu/home/overview.html> (Feb. 19, 2013).

OpenSees. University of California, Berkeley, CA, <http://opensees.berkeley.edu/wiki/index.php/Main_Page> (March 20, 2013).

Roberts, T.M., and Ghomi, S.S. (1991). "Hysteretic Characteristics of Unstiffened Plate Shear Panels," *Thin-Walled Structures*, 12, 145-162.

SAP2000. Computers & Structures, Inc., Berkeley, CA.

Timler, P.A., and Kulak, G.L. (1983). "Experimental Study of Steel Plate Shear Walls." *Structural Engineering Report No. 114*, Department of Civil Engineering, The University of Alberta, Edmonton, Canada.

Zhao, Q., and Astaneh-Asl, A. (2004). "Cyclic Behavior of an Innovative Steel Shear Wall System." *13th World Conference on Earthquake Engineering*, Vancouver, Canada.

APPENDIX A

PI TERMS USED IN THE SMALL-SCALE SPECIMEN DESIGN

A.1 Pi Terms - VBE, HBE, and CB

Variable		Basic Dimension	Pi Term
Height	h	L	
Width	w	L	$\Pi_1 = \frac{w}{h}$
Length	l	L	$\Pi_2 = \frac{l}{h}$
Deflection	δ	L	$\Pi_3 = \frac{\delta}{h}$
Area	A	L^2	$\Pi_4 = \frac{A}{h^2}$
Young's Modulus	E	FL^{-2}	
Moment of Inertia	I	L^4	$\Pi_5 = \frac{I}{h^4}$
Yield Strength	F_y	FL^{-2}	$\Pi_6 = \frac{F_y}{E}$
Plastic Section Modulus	Z	L^3	$\Pi_7 = \frac{Z}{h^3}$
Plastic Moment	M_p	FL	$\Pi_8 = \frac{F_y Z}{E h^3}$
Force	F	F	$\Pi_9 = \frac{F}{h^2 E}$
Moment	M	FL	$\Pi_{10} = \frac{M}{h^3 E}$
Mass	m	$FL^{-1}T^2$	$\Pi_{11} = \frac{m}{hEt^2}$
Acceleration	a	LT^{-2}	$\Pi_{12} = \frac{at^2}{h}$
Time	t	T	

Note: The repeating variables are h, E, and t.

A.2 Pi Terms - Web Plate

Variable		Dimension	Pi Term
Web Plate Thickness	t_w	L	$\Pi_{13} = \frac{t_w}{L_{cf}}$
Tensile Field Angle	α		$\Pi_{14} = \alpha$
Yield Strength	F_y	FL^{-2}	
Clear Length of Web Panel between VBE Flanges	L_{cf}	L	
Nominal Shear Strength	V_n	F	$\Pi_{15} = \frac{V_n}{F_y {L_{cf}}^2}$

Note: The repeating variables are F_y and L_{cf}.

APPENDIX B
SCALE FACTORS USED IN THE SMALL-SCALE SPECIMEN DESIGN

B.1 Scale Factors for VBE, HBE, and CB

Variable	Scale Factor
Height	0.150
Length	0.150
Area	0.023
Young's Modulus	1
Moment of Inertia	0.001
Plastic Moment	0.003

B.2 Scale Factors for Web Plate

Variable	Scale Factor
Web-Plate Thickness	0.150
Nominal Shear Strength	0.0225

APPENDIX C

DETAILED DRAWINGS OF THE SMALL-SCALE SPSW-WC SPECIMEN

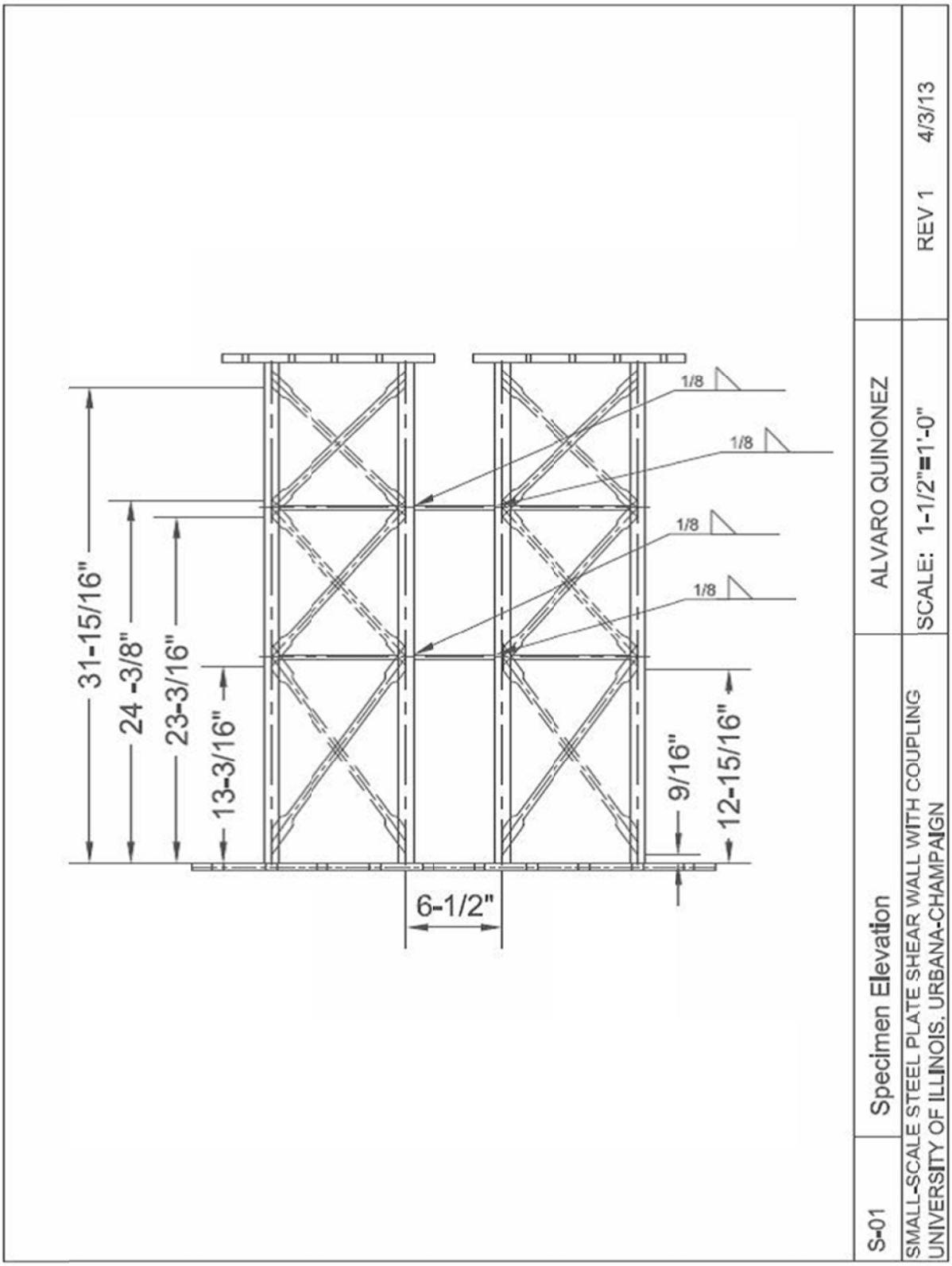

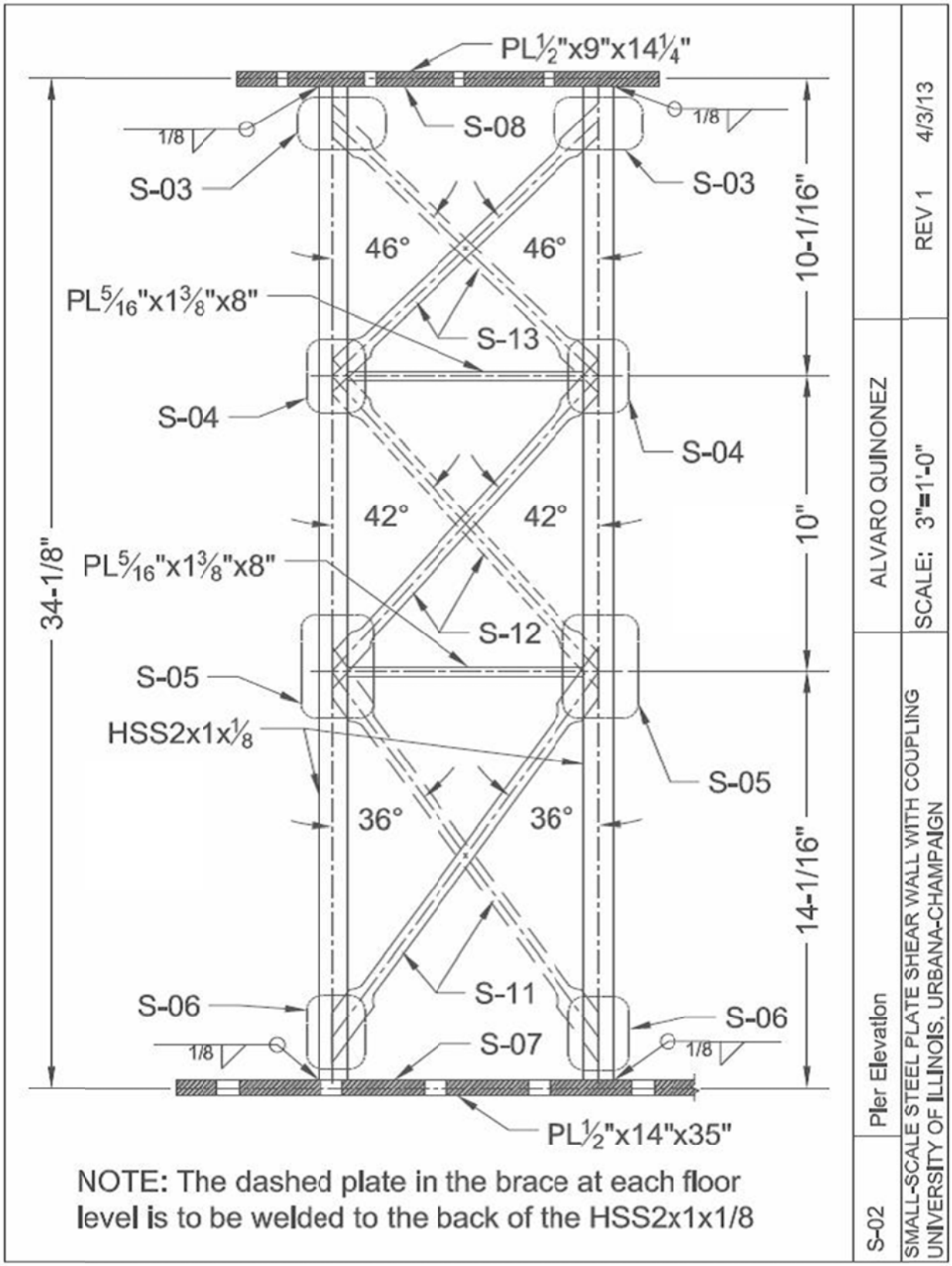
PL½"x9"x14¼"
S-08
1/8
1/8
S-03
S-03
46°
46°
PL5⁄16"x1⅜"x8"
S-13
S-04
S-04
42°
42°
PL5⁄16"x1⅜"x8"
S-12
S-05
S-05
HSS2x1x⅛
36°
36°
S-11
S-06
S-06
S-07
1/8
1/8
PL½"x14"x35"
34-1/8"
10-1/16"
10"
14-1/16"
NOTE: The dashed plate in the brace at each floor level is to be welded to the back of the HSS2x1x1/8
ALVARO QUINONEZ
REV 1 4/3/13
SCALE: 3"=1'-0"
Pier Elevation
S-02
SMALL-SCALE STEEL PLATE SHEAR WALL WITH COUPLING
UNIVERSITY OF ILLINOIS, URBANA-CHAMPAIGN

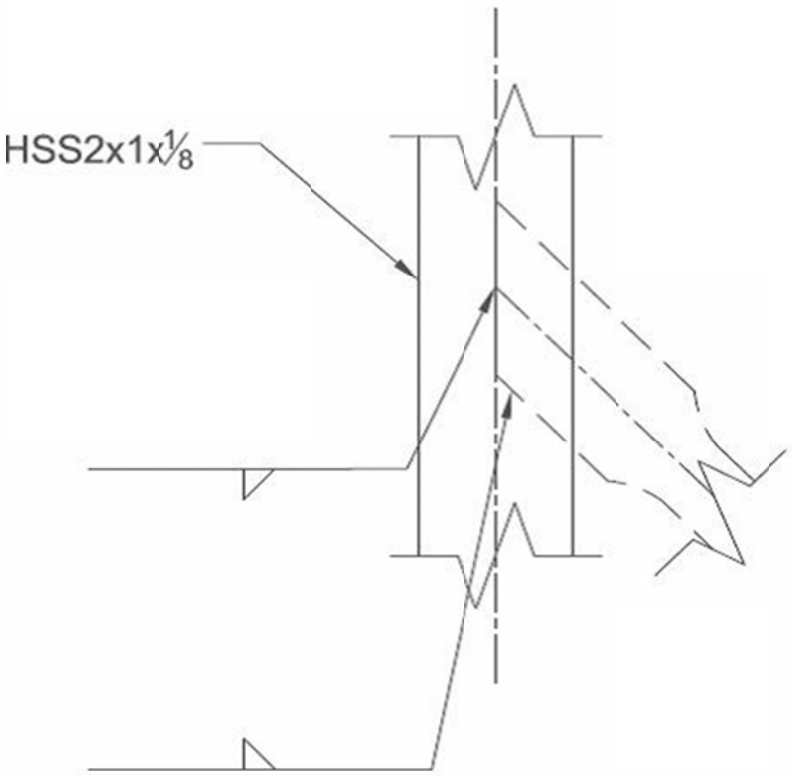

NOTE: The dashed plate is to be welded to the back of the HSS2x1x1/8

S-03	Fillet Weld Connection Detail	ALVARO QUINONEZ	
SMALL-SCALE STEEL PLATE SHEAR WALL WITH COUPLING UNIVERSITY OF ILLINOIS, URBANA-CHAMPAIGN		SCALE: 1'-0"=1'-0"	REV 1 4/3/13

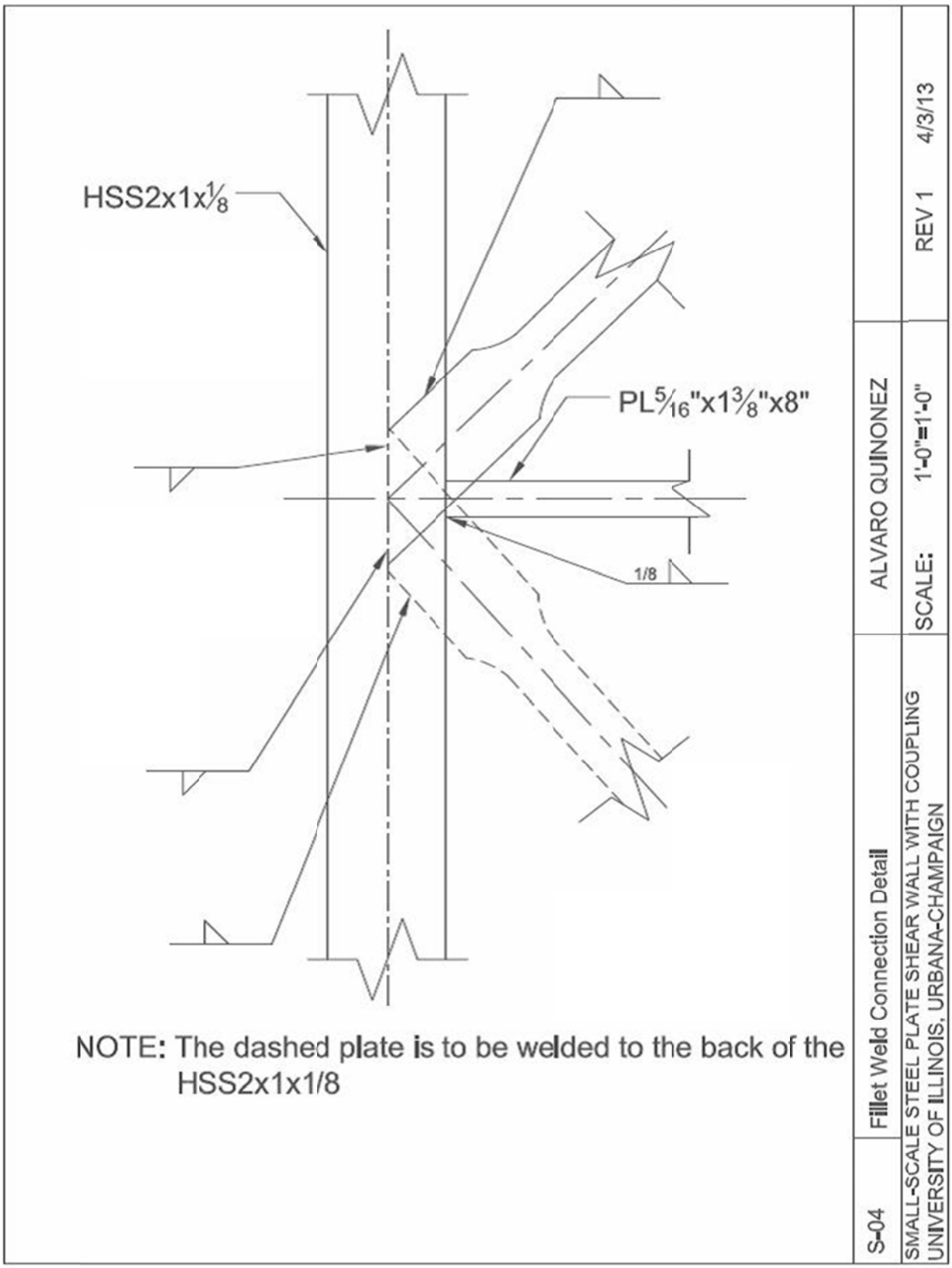
HSS2x1x1/8
PL5/16"x1 3/8"x8"
1/8
NOTE: The dashed plate is to be welded to the back of the HSS2x1x1/8
S-04
Fillet Weld Connection Detail
SMALL-SCALE STEEL PLATE SHEAR WALL WITH COUPLING
UNIVERSITY OF ILLINOIS, URBANA-CHAMPAIGN
ALVARO QUINONEZ
SCALE: 1'-0"=1'-0"
REV 1 4/3/13

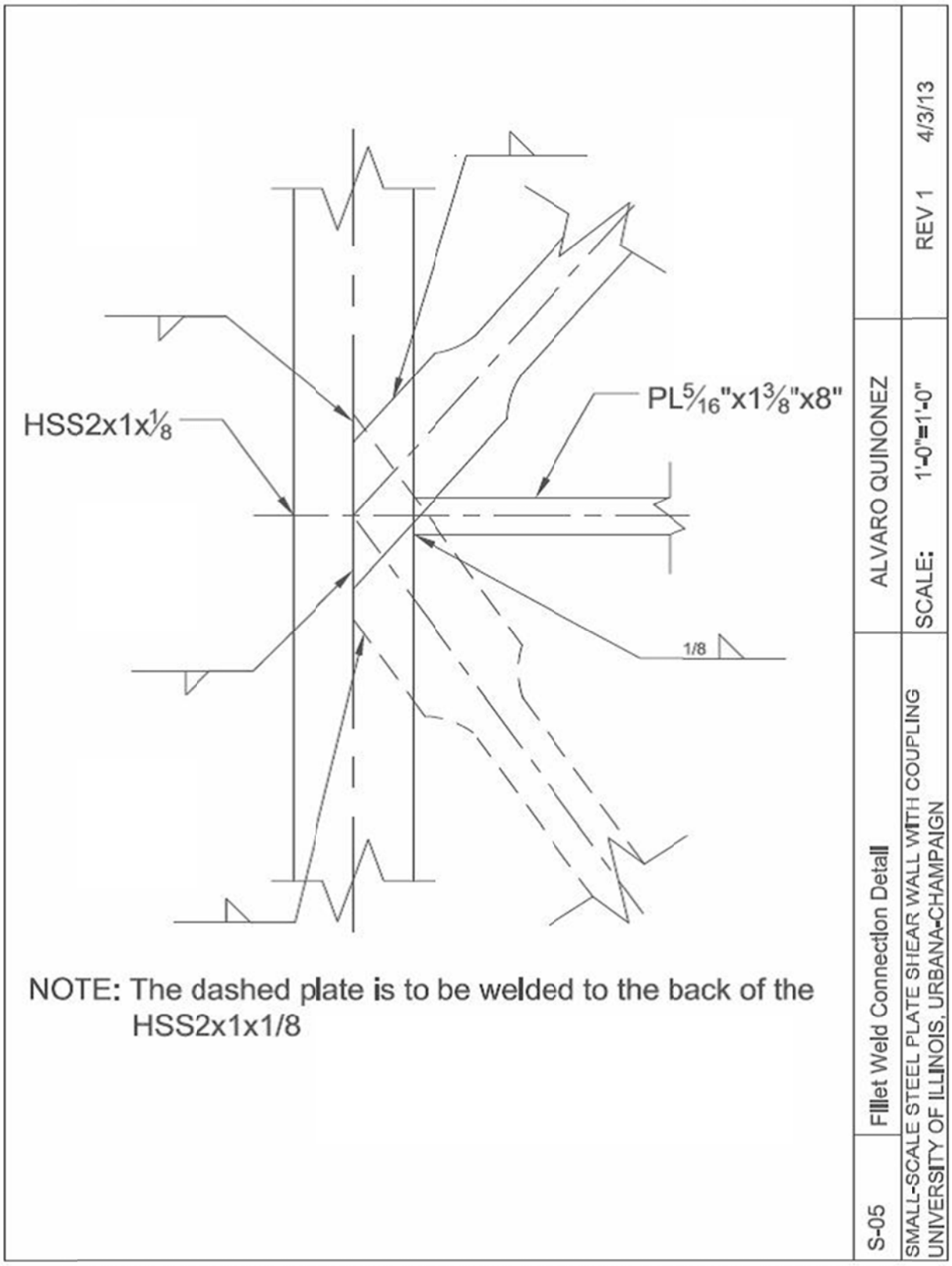
HSS2x1x1/8
PL5/16"x1 3/8"x8"
1/8
NOTE: The dashed plate is to be welded to the back of the HSS2x1x1/8
S-05
Fillet Weld Connection Detail
ALVARO QUINONEZ
SCALE: 1'-0"=1'-0"
REV 1 4/3/13
SMALL-SCALE STEEL PLATE SHEAR WALL WITH COUPLING
UNIVERSITY OF ILLINOIS, URBANA-CHAMPAIGN

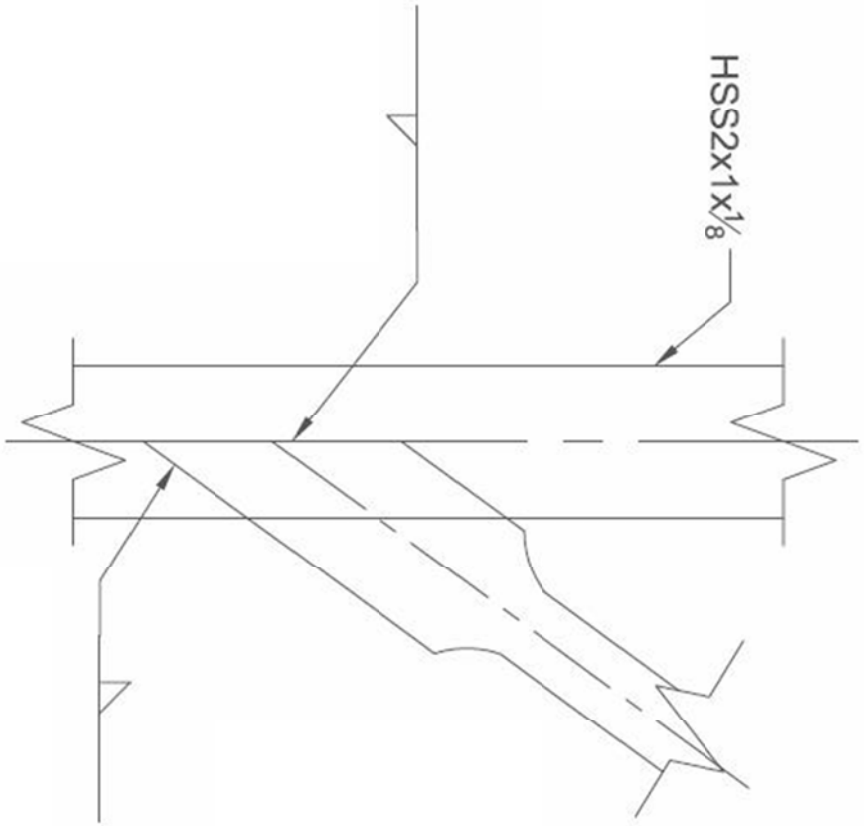

S-06	Fillet Weld Connection Detail	ALVARO QUINONEZ	
SMALL-SCALE STEEL PLATE SHEAR WALL WITH COUPLING UNIVERSITY OF ILLINOIS, URBANA-CHAMPAIGN		SCALE: 1'-0"=1'-0"	REV 1 4/3/13

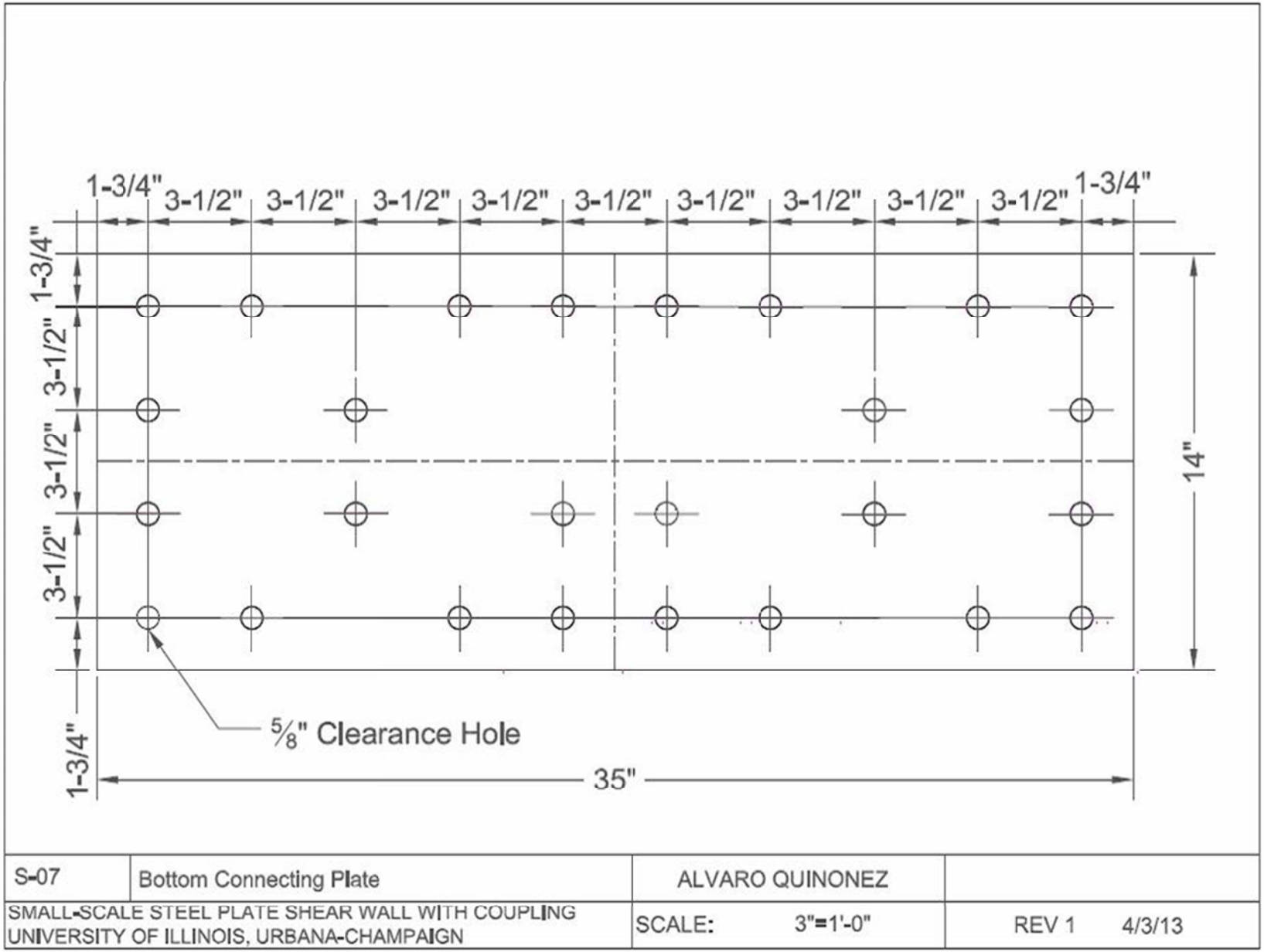

S-07	Bottom Connecting Plate	ALVARO QUINONEZ	
SMALL-SCALE STEEL PLATE SHEAR WALL WITH COUPLING UNIVERSITY OF ILLINOIS, URBANA-CHAMPAIGN		SCALE: 3"=1'-0"	REV 1 4/3/13

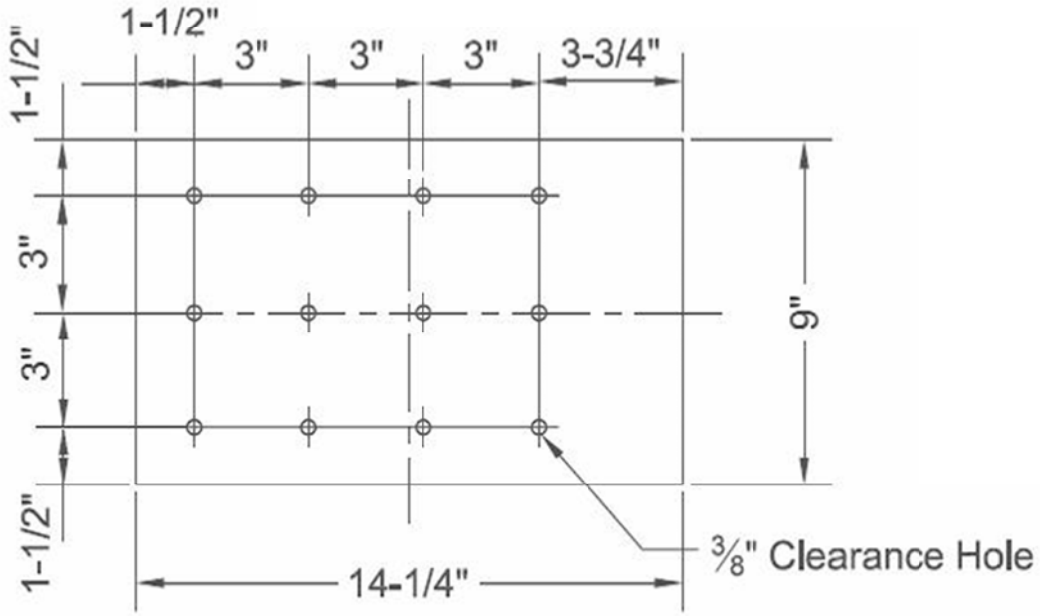

S-08	Top Connecting Plate	ALVARO QUINONEZ	
SMALL-SCALE STEEL PLATE SHEAR WALL WITH COUPLING UNIVERSITY OF ILLINOIS, URBANA-CHAMPAIGN		SCALE: 3"=1'-0"	REV 1 4/3/13

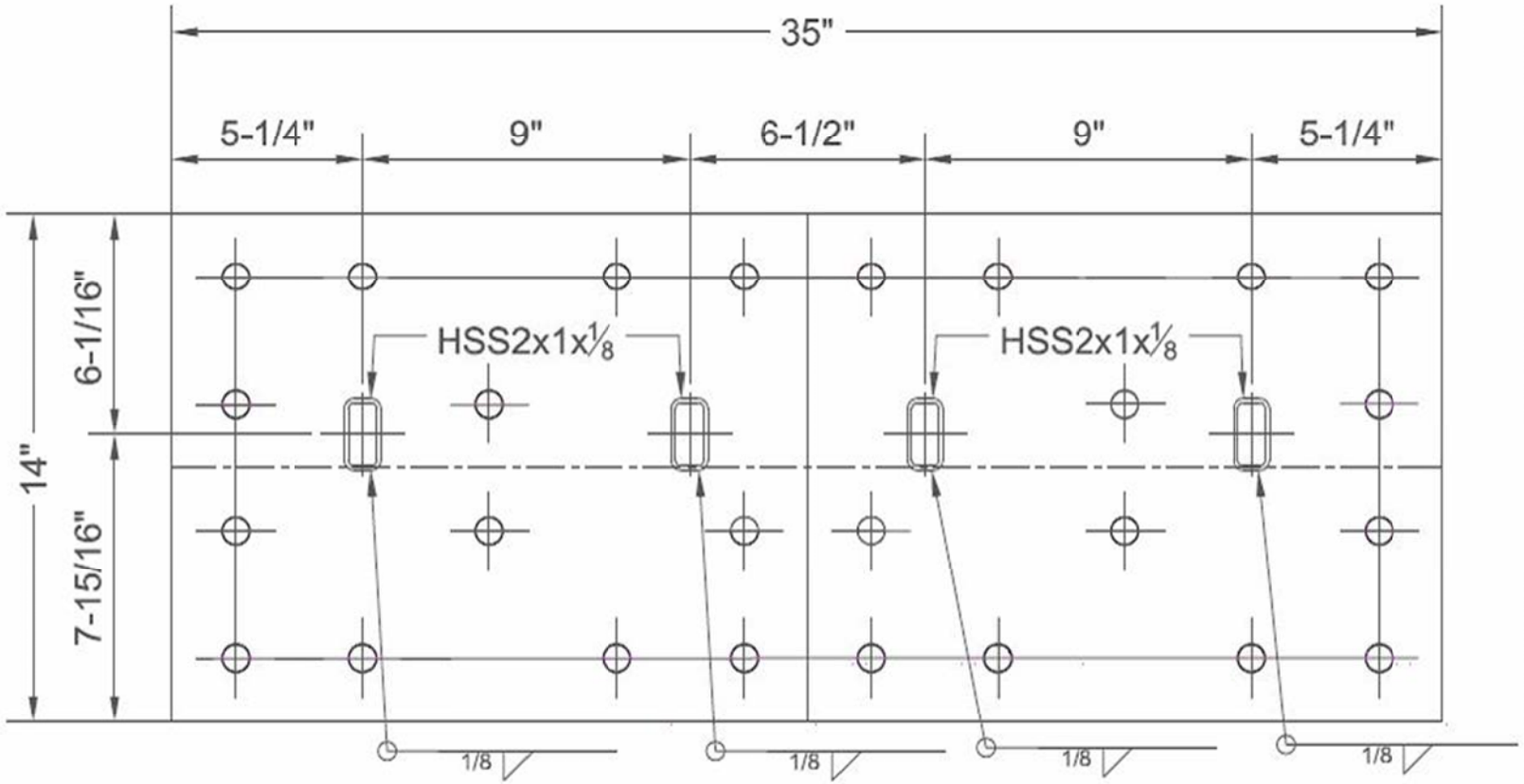

S-09	Bottom Connecting Plate with HSS2x1x1/8	ALVARO QUINONEZ	
SMALL-SCALE STEEL PLATE SHEAR WALL WITH COUPLING UNIVERSITY OF ILLINOIS, URBANA-CHAMPAIGN		SCALE: 3"-1'-0"	REV 1 4/3/13

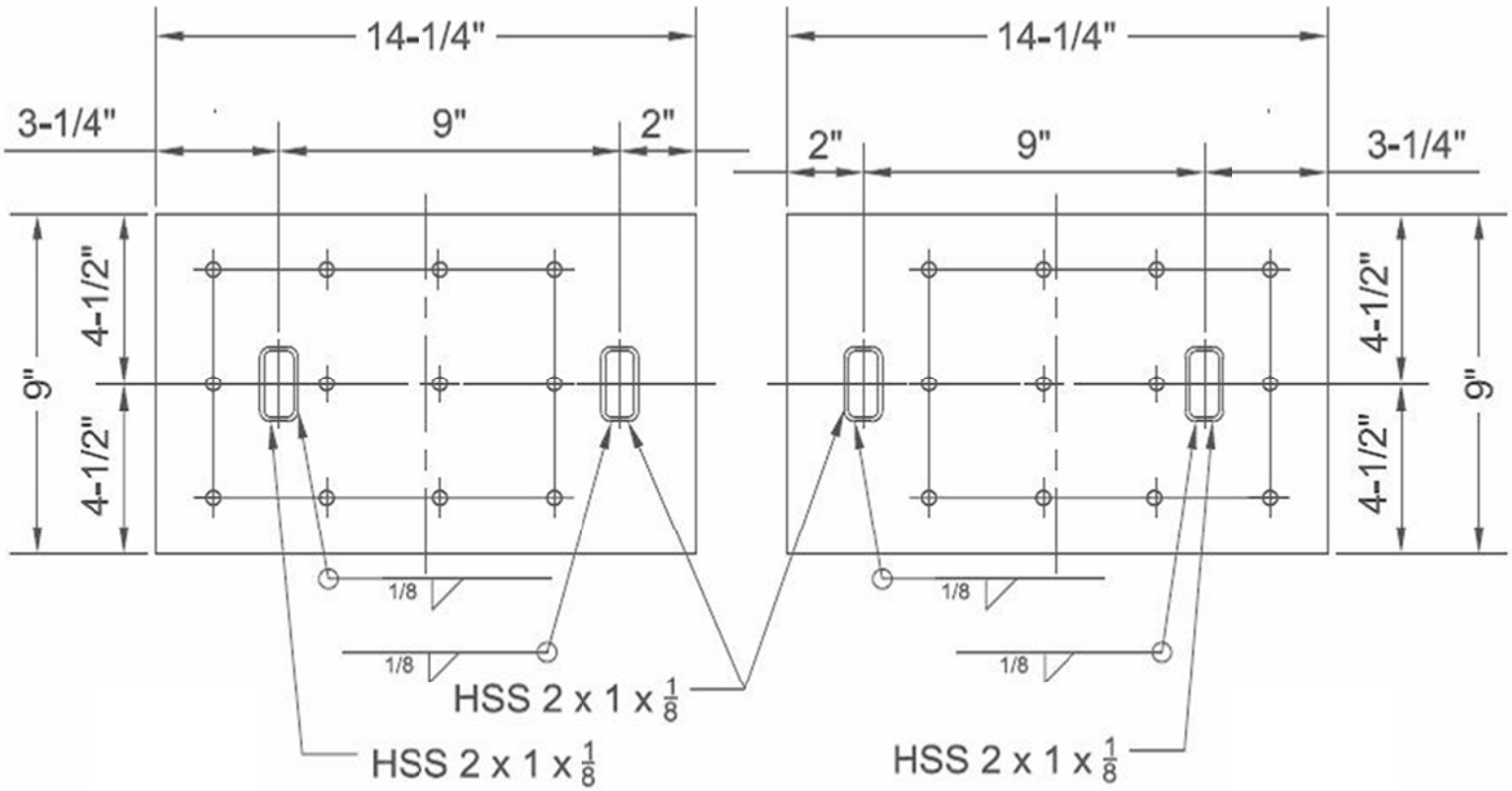

S-10	Top Connecting Plates with HSS2x1x1/8	ALVARO QUINONEZ	
SMALL-SCALE STEEL PLATE SHEAR WALL WITH COUPLING UNIVERSITY OF ILLINOIS, URBANA-CHAMPAIGN		SCALE: 3"=1'-0"	REV 1 4/3/13

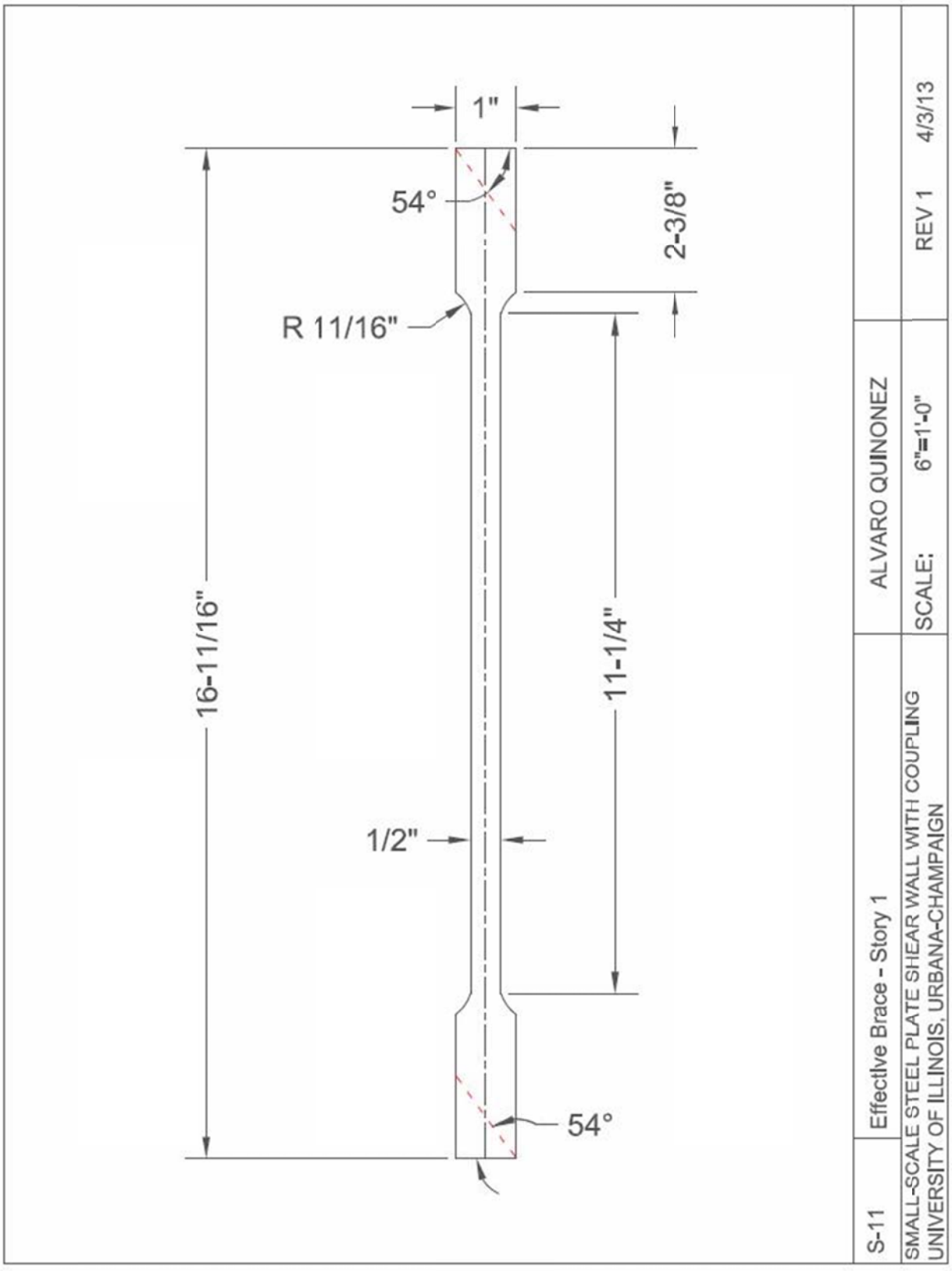
1"
54°
2-3/8"
R 11/16"
16-11/16"
11-1/4"
1/2"
54°
S-11
Effective Brace - Story 1
ALVARO QUINONEZ
SMALL-SCALE STEEL PLATE SHEAR WALL WITH COUPLING
UNIVERSITY OF ILLINOIS, URBANA-CHAMPAIGN
SCALE: 6"=1'-0"
REV 1 4/3/13

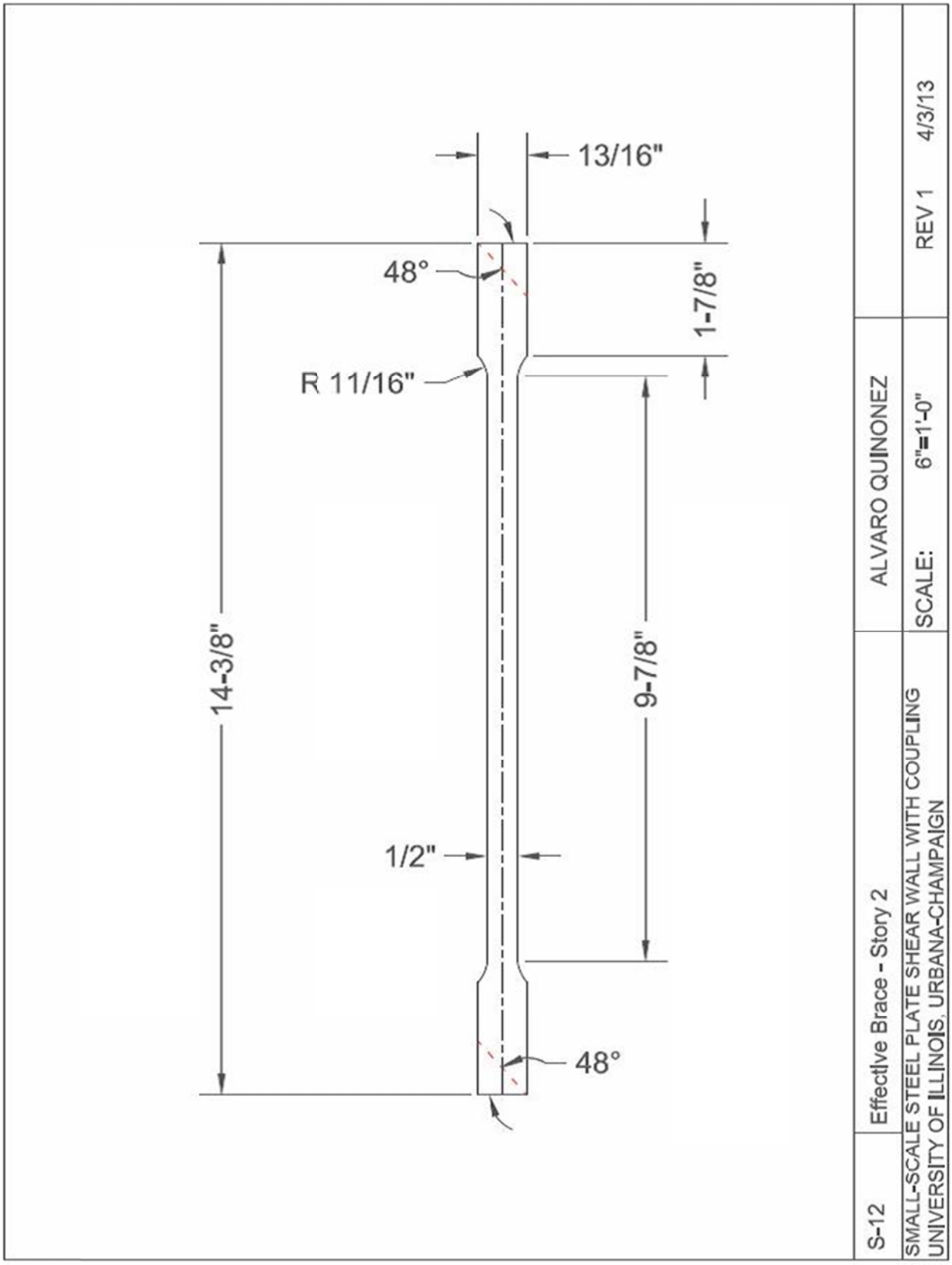
13/16"
48°
1-7/8"
R 11/16"
14-3/8"
9-7/8"
1/2"
48°
S-12
Effective Brace - Story 2
SMALL-SCALE STEEL PLATE SHEAR WALL WITH COUPLING
UNIVERSITY OF ILLINOIS, URBANA-CHAMPAIGN
ALVARO QUINONEZ
SCALE: 6"=1'-0"
REV 1 4/3/13

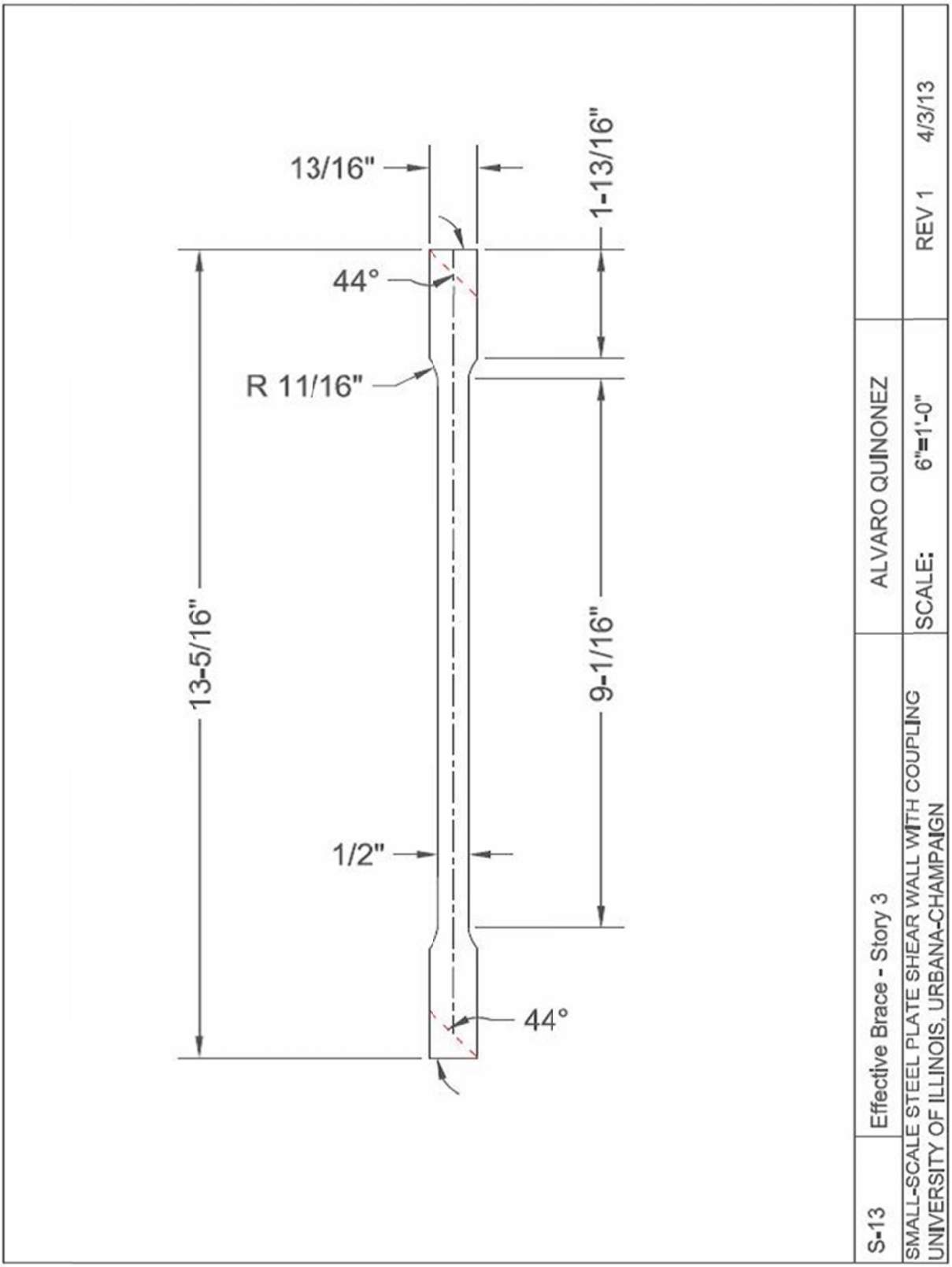
13/16"
1-13/16"
44°
R 11/16"
13-5/16"
9-1/16"
1/2"
44°
S-13
Effective Brace - Story 3
ALVARO QUINONEZ
SMALL-SCALE STEEL PLATE SHEAR WALL WITH COUPLING
UNIVERSITY OF ILLINOIS, URBANA-CHAMPAIGN
SCALE: 6"=1'-0"
REV 1 4/3/13

APPENDIX D

OPENSEES MATLAB SCRIPT

```
clear all
clc
close all

f = fopen('SmallScaleOS.tcl','w');

% OpenSees Model of Small-Scale SPSW-WC
% --------------------------------------

% Units are kip, inch, and second

% Static pushover analysis of small-scale specimen
% ------------------------------------------------------
fprintf(f,'wipe all\n');

% Create ModelBuilder (2 dimensions and 3 DOF/node)
fprintf(f,'model BasicBuilder -ndm 2 -ndf 3\n');

% -------------------
% Definition of Nodes
% -------------------
Nodes(  1   ,   :   ) = [0 0];
Nodes(  2   ,   :   ) = [9 0];
Nodes(  3   ,   :   ) = [15.5 0];
Nodes(  4   ,   :   ) = [24.5 0];
Nodes(  5   ,   :   ) = [0 1.68];
Nodes(  6   ,   :   ) = [9 1.68];
Nodes(  7   ,   :   ) = [15.5 1.68];
Nodes(  8   ,   :   ) = [24.5 1.68];
Nodes(  9   ,   :   ) = [  0.0     14.0625 ];
Nodes(  10  ,   :   ) = [ 9.0     14.0625 ];
Nodes(  11  ,   :   ) = [ 15.5     14.0625 ];
Nodes(  12  ,   :   ) = [ 24.5     14.0625 ];
Nodes(  13  ,   :   ) = [ 0.0     24.0625 ];
Nodes(  14  ,   :   ) = [ 9.0     24.0625 ];
Nodes(  15  ,   :   ) = [ 15.5     24.0625 ];
Nodes(  16  ,   :   ) = [ 24.5     24.0625 ];
Nodes(  17  ,   :   ) = [ 0.0     32.735 ];
Nodes(  18  ,   :   ) = [ 9.0     32.735 ];
Nodes(  19  ,   :   ) = [ 15.5     32.735 ];
Nodes(  20  ,   :   ) = [ 24.5     32.735 ];
Nodes(  21  ,   :   ) = [ 0.0     34.125 ];
```

```
Nodes(  22  ,   :   ) = [ 9.0     34.125 ];
Nodes(  23  ,   :   ) = [ 15.5    34.125 ];
Nodes(  24  ,   :   ) = [ 24.5    34.125 ];
Nodes(  25  ,   :   ) = [ 4.5    34.125 ];
Nodes(  26  ,   :   ) = [ 20.0    34.125 ];
Nodes(  27  ,   :   ) = [ 4.5    0.0];
Nodes(  28  ,   :   ) = [ 12.25     0.0 ];
Nodes(  29  ,   :   ) = [ 20.0  0.0 ];


for i = 1:size(Nodes,1);
   fprintf(f,'node %i %g %g\n',i,Nodes(i,1),Nodes(i,2));
end


% -------------------------
% Apply boundary conditions
% -------------------------

%   tag DX  DY  DZ
fprintf(f,'fix  1   1   1   1\n');
fprintf(f,'fix  2  1   1   1\n');
fprintf(f,'fix  3  1   1   1\n');
fprintf(f,'fix  4  1   1   1\n');
fprintf(f,'fix  27  1   1   1\n');
fprintf(f,'fix  28  1   1   1\n');
fprintf(f,'fix  29  1   1   1\n');


% -------------------------
% Define material properties
% -------------------------
% Define a UniaxialMaterial object represented uniaxial stress-strain behavior

% One material object for the VBEs, and another object for the HBEs and CBs

% Steel - Using Steel01 Material which is a uniaxial bilinear material object with kinematic
hardening

% Steel material object for VBEs
%                   mattag, Fy,     E,  strain-hardening ratio,
%                   (for Steel02 R0=10 to 20, cR1=0.925, cR2=0.15)
fprintf(f,'uniaxialMaterial Steel01 1        46.0   29000 0.001 \n');

% Steel material object for HBEs and CBs
fprintf(f,'uniaxialMaterial Steel01 2        36.0   29000 0.001 \n');
```

```
% Steel material object for braces
fprintf(f,'uniaxialMaterial Steel01 3        54.0   30612 0.0001 \n');


% ---------------
% Define sections
% ---------------

% VBE fibers
% ----------
fprintf(f,'section Fiber 1 {\n');
% top, bottom, left, right - use rectangular patch
% material tag, number of fibers in local y direction, number of fibers in local z direction, y and
z corrds of vertex I, y and z coords of vertex J

fprintf(f,'patch rect 1 10 1 0.384 -1.0 0.5 1.0\n');
fprintf(f,'patch rect 1 10 1 -0.5 -1.0 -0.384 1.0\n');
fprintf(f,'patch rect 1 5 1 -0.384 0.884 0.384 1.0\n');
fprintf(f,'patch rect 1 5 1 -0.384 -1.0 0.384 -0.884\n');
fprintf(f,'}\n');

% HBE and CB fibers
% -----------------
fprintf(f,'section Fiber 2 {\n');
% Use rectangular patch
% material tag, number of fibers in local y direction, number of fibers in local z direction, y and
z corrds of vertex I, y and z coords of vertex J
fprintf(f,'patch rect 2 10 1 -0.15625 -0.6875 0.15625 0.6875\n');
fprintf(f,'}\n');


% ------------------
% Element Definition
% ------------------

% Coordinate transformation object for VBEs
fprintf(f,'geomTransf Corotational 1\n');

% Coordinate transformation object for HBEs and CBs
fprintf(f,'geomTransf Corotational 2\n');

% Coordinate transformation object for braces
fprintf(f,'geomTransf Corotational 3\n');
```

```
% VBEs, HBEs, and CBs represented by force-based beam-columns that allow for the spread of plasticity along the element

% HBEs
% ------
% element_tag, node i, node j, number of integration points, section object ID, coord-transformation ID
fprintf(f,'element forceBeamColumn 1 9 10 5 2 2\n');
fprintf(f,'element forceBeamColumn 2 13 14 5 2 2\n');
fprintf(f,'element forceBeamColumn 3 11 12 5 2 2\n');
fprintf(f,'element forceBeamColumn 4 15 16 5 2 2\n');

% CBs
% ------
% element_tag, node i, node j, number of integration points, section object ID, coord-transformation ID
fprintf(f,'element forceBeamColumn 5 10 11 5 2 2\n');
fprintf(f,'element forceBeamColumn 6 14 15 5 2 2\n');

% VBEs
% -----
% element_tag, node i, node j, number of integration points, section object ID, coord-transformation ID
fprintf(f,'element forceBeamColumn 7 1 5 5 1 1\n');
fprintf(f,'element forceBeamColumn 8 5 9 5 1 1\n');
fprintf(f,'element forceBeamColumn 9 9 13 5 1 1\n');
fprintf(f,'element forceBeamColumn 10 13 17 5 1 1\n');
fprintf(f,'element forceBeamColumn 11 17 21 5 1 1\n');

fprintf(f,'element forceBeamColumn 12 2 6 5 1 1\n');
fprintf(f,'element forceBeamColumn 13 6 10 5 1 1\n');
fprintf(f,'element forceBeamColumn 14 10 14 5 1 1\n');
fprintf(f,'element forceBeamColumn 15 14 18 5 1 1\n');
fprintf(f,'element forceBeamColumn 16 18 22 5 1 1\n');

fprintf(f,'element forceBeamColumn 17 3 7 5 1 1\n');
fprintf(f,'element forceBeamColumn 18 7 11 5 1 1\n');
fprintf(f,'element forceBeamColumn 19 11 15 5 1 1\n');
fprintf(f,'element forceBeamColumn 20 15 19 5 1 1\n');
fprintf(f,'element forceBeamColumn 21 19 23 5 1 1\n');

fprintf(f,'element forceBeamColumn 22 4 8 5 1 1\n');
fprintf(f,'element forceBeamColumn 23 8 12 5 1 1\n');
fprintf(f,'element forceBeamColumn 24 12 16 5 1 1\n');
fprintf(f,'element forceBeamColumn 25 16 20 5 1 1\n');
fprintf(f,'element forceBeamColumn 26 20 24 5 1 1\n');
```

```
% Braces
% -------
% Use truss element
% ------------------------------------------------
% ------------------------------------------------
% First Story, Left Pier
% Front brace
fprintf(f,'element truss 27 5 10 0.03 3\n');

% ------------------------------------------------

% First Story. Right Pier
% Front brace
fprintf(f,'element truss 29 7 12 0.03 3\n');

% ------------------------------------------------
% ------------------------------------------------

% Second Story, Left Pier
% Front brace
fprintf(f,'element truss 31 9 14 0.03 3\n');

% ------------------------------------------------

% Second Story, Right Pier
% Front brace
fprintf(f,'element truss 33 11 16 0.03 3\n');


% ------------------------------------------------
% ------------------------------------------------

% Third Story, Left Pier
% Front brace
fprintf(f,'element truss 35 13 18 0.03 3 \n');


% ------------------------------------------------

% Third Story, Right Pier
% Front brace
fprintf(f,'element truss 37 15 20 0.03 3  \n');


% Top and bottom connecting plates - use elastic beam column elements
```

```
% -----------------------------------------------------------------
%% Top
% element elasticBeamColumn $eleTag $iNode $jNode $A $E $Iz $transfTag
% Pier 1
fprintf(f,'element elasticBeamColumn 39 21 25 4.5 29000 3.33 2\n');
fprintf(f,'element elasticBeamColumn 40 25 22 4.5 29000 3.33 2\n');

% Pier 2
fprintf(f,'element elasticBeamColumn 41 23 26 4.5 29000 3.33 2\n');
fprintf(f,'element elasticBeamColumn 42 26 24 4.5 29000 3.33 2\n');

%% Bottom
fprintf(f,'element elasticBeamColumn 43 1 27 70.0 29000 0.1458 2 \n');
fprintf(f,'element elasticBeamColumn 44 27 2 70.0 29000 0.1458 2\n');
fprintf(f,'element elasticBeamColumn 45 2 28 70.0 29000 0.1458 2 \n');
fprintf(f,'element elasticBeamColumn 46 28 3 70.0 29000 0.1458 2 \n');
fprintf(f,'element elasticBeamColumn 47 3 29 70.0 29000 0.1458 2\n');
fprintf(f,'element elasticBeamColumn 48 29 4 70.0 29000 0.1458 2 \n');

% ------------------------
% End of model generation
% ------------------------

% Create Gravity Load Pattern
% ---------------------------

% Gravity Load

% Define Time Series
fprintf(f,'timeSeries Constant 1\n');

% VBEs - convert distributed self-wight to nodal loads
fprintf(f,'pattern Plain 1 1 {\n');
%load $nodeTag (ndf $LoadValues)
% Pier 1 - Left VBE
fprintf(f,'load 21 0.0 -1.268e-4 0.0\n');
fprintf(f,'load 17 0.0 -9.18e-4 0.0\n');
fprintf(f,'load 13 0.0 -0.001704 0.0\n');
fprintf(f,'load 9 0.0 -0.002043 0.0\n');
fprintf(f,'load 5 0.0 -0.001283 0.0\n');
fprintf(f,'load 1 0.0 -1.533e-4 0.0\n');
% Pier 1 - Right VBE
fprintf(f,'load 22 0.0 -1.268e-4 0.0\n');
fprintf(f,'load 18 0.0 -9.18e-4 0.0\n');
fprintf(f,'load 14 0.0 -0.001704 0.0\n');
fprintf(f,'load 10 0.0 -0.002043 0.0\n');
```

```
fprintf(f,'load 6 0.0 -0.001283 0.0\n');
fprintf(f,'load 2 0.0 -1.533e-4 0.0\n');
% Pier 2 - Left VBE
fprintf(f,'load 23 0.0 -1.268e-4 0.0\n');
fprintf(f,'load 19 0.0 -9.18e-4 0.0\n');
fprintf(f,'load 15 0.0 -0.001704 0.0\n');
fprintf(f,'load 11 0.0 -0.002043 0.0\n');
fprintf(f,'load 7 0.0 -0.001283 0.0\n');
fprintf(f,'load 3 0.0 -1.533e-4 0.0\n');
% Pier 2 - Right VBE
fprintf(f,'load 24 0.0 -1.268e-4 0.0\n');
fprintf(f,'load 20 0.0 -9.18e-4 0.0\n');
fprintf(f,'load 16 0.0 -0.001704 0.0\n');
fprintf(f,'load 12 0.0 -0.002043 0.0\n');
fprintf(f,'load 8 0.0 -0.001283 0.0\n');
fprintf(f,'load 4 0.0 -1.533e-4 0.0\n');

% HBEs
% Pier 1
fprintf(f,'load 9 0.0 -4.88e-4 0.0\n');
fprintf(f,'load 10 0.0 -4.88e-4 0.0\n');
fprintf(f,'load 13 0.0 -4.88e-4 0.0\n');
fprintf(f,'load 14 0.0 -4.88e-4 0.0\n');
% Pier 2
fprintf(f,'load 11 0.0 -4.88e-4 0.0\n');
fprintf(f,'load 12 0.0 -4.88e-4 0.0\n');
fprintf(f,'load 15 0.0 -4.88e-4 0.0\n');
fprintf(f,'load 16 0.0 -4.88e-4 0.0\n');

%CBs
fprintf(f,'load 10 0.0 -3.36e-4 0.0\n');
fprintf(f,'load 11 0.0 -3.36e-4 0.0\n');
fprintf(f,'load 14 0.0 -3.36e-4 0.0\n');
fprintf(f,'load 15 0.0 -3.36e-4 0.0\n');

% Braces
% Pier 1
%Story 1
fprintf(f,'load 5 0.0 -6.52e-5 0.0\n');
fprintf(f,'load 10 0.0 -6.52e-5 0.0\n');

%Story 2
fprintf(f,'load 9 0.0 -5.73e-5 0.0\n');
fprintf(f,'load 14 0.0 -5.73e-5 0.0\n');

%Story 3
```

```
fprintf(f,'load 13 0.0 -5.33e-5 0.0\n');
fprintf(f,'load 18 0.0 -5.33e-5 0.0\n');

% ----------------------------------------
% Pier 2
%Story 1
fprintf(f,'load 7 0.0 -6.52e-5 0.0\n');
fprintf(f,'load 12 0.0 -6.52e-5 0.0\n');

%Story 2
fprintf(f,'load 11 0.0 -5.73e-5 0.0\n');
fprintf(f,'load 16 0.0 -5.73e-5 0.0\n');

%Story 3
fprintf(f,'load 15 0.0 -5.33e-5 0.0\n');
fprintf(f,'load 20 0.0 -5.33e-5 0.0\n');


% Top Plates and Bottom Plate
%Top Plate
% Pier 1
fprintf(f,'load 21 0.0 -0.0014 0.0\n');
fprintf(f,'load 25 0.0 -0.0029 0.0\n');
fprintf(f,'load 22 0.0 -0.0014 0.0\n');


% Pier 2
fprintf(f,'load 23 0.0 -0.0014 0.0\n');
fprintf(f,'load 26 0.0 -0.0029 0.0\n');
fprintf(f,'load 24 0.0 -0.0014 0.0\n');


%Bottom Plate
% Loads will not affect analysis

fprintf(f,'}\n');

% Gravity Load Analysis
% ----------------------
% Constraints command
fprintf(f,'constraints Plain\n');

% Numberer command
fprintf(f,'numberer RCM\n');

% System command
```

```
fprintf(f,'system ProfileSPD\n');

% Test command
fprintf(f,'test NormDispIncr 1e-5 6\n');

% Algorithm command
fprintf(f,'algorithm Newton\n');

% Integrator command - load increment of 1 applied at each analysis step
fprintf(f,'integrator LoadControl 1\n');

% Analysis command
fprintf(f,'analysis Static\n');

%  Eigen command - Gravity loads applied in 1 step
fprintf(f,'analyze 1\n');

% Maintain constant gravity loads and reset time to zero
fprintf(f,'loadConst -time 0.0\n');

% ------------------------
% Pushover Analysis
% ------------------------
fprintf(f,'recorder Node -file DispSmall.txt -time -node 25 -dof 1 2 disp\n');
fprintf(f,'recorder Node -file RexnSmall.txt -time -node 1 2 3 4 -dof 1 2 3 reaction\n');

%% Create recorders
% To record stress-strain in the HBEs and CBs
% HBEs
fprintf(f,'recorder Element -file stress_strain_HBE_1_1.txt -time -ele 1 section 1 fiber 0.03125
0.6875 stressStrain\n');
fprintf(f,'recorder Element -file stress_strain_HBE_1_5.txt -time -ele 1 section 5 fiber 0.03125
0.6875 stressStrain\n');
fprintf(f,'recorder Element -file stress_strain_HBE_2_1.txt -time -ele 2 section 1 fiber 0.03125
0.6875 stressStrain\n');
fprintf(f,'recorder Element -file stress_strain_HBE_2_5.txt -time -ele 2 section 5 fiber 0.03125
0.6875 stressStrain\n');
fprintf(f,'recorder Element -file stress_strain_HBE_3_1.txt -time -ele 3 section 1 fiber 0.03125
0.6875 stressStrain\n');
fprintf(f,'recorder Element -file stress_strain_HBE_3_5.txt -time -ele 3 section 5 fiber 0.03125
0.6875 stressStrain\n');
fprintf(f,'recorder Element -file stress_strain_HBE_4_1.txt -time -ele 4 section 1 fiber 0.03125
0.6875 stressStrain\n');
fprintf(f,'recorder Element -file stress_strain_HBE_4_5.txt -time -ele 4 section 5 fiber 0.03125
0.6875 stressStrain\n');
% CBs
```

```
fprintf(f,'recorder Element -file stress_strain_CB_5_1.txt -time -ele 5 section 1 fiber 0.03125
0.6875 stressStrain\n');
fprintf(f,'recorder Element -file stress_strain_CB_5_5.txt -time -ele 5 section 5 fiber 0.03125
0.6875 stressStrain\n');
fprintf(f,'recorder Element -file stress_strain_CB_6_1.txt -time -ele 6 section 1 fiber 0.03125
0.6875 stressStrain\n');
fprintf(f,'recorder Element -file stress_strain_CB_6_5.txt -time -ele 6 section 5 fiber 0.03125
0.6875 stressStrain\n');

% To record plastic deformation and rotation in the HBEs and CBs
% HBEs
fprintf(f,'recorder Element -file plasticdeform_HBE_1.txt -time -ele 1 plasticDeformation\n');
fprintf(f,'recorder Element -file plasticdeform_HBE_2.txt -time -ele 2 plasticDeformation\n');
fprintf(f,'recorder Element -file plasticdeform_HBE_3.txt -time -ele 3 plasticDeformation\n');
fprintf(f,'recorder Element -file plasticdeform_HBE_4.txt -time -ele 4 plasticDeformation\n');
% CBs
fprintf(f,'recorder Element -file plasticdeform_CB_5.txt -time -ele 5 plasticDeformation\n');
fprintf(f,'recorder Element -file plasticdeform_CB_6.txt -time -ele 6 plasticDeformation\n');

% To record axial force and deformation in braces
fprintf(f,'recorder Element -file Brace_axialF_27.txt -ele 27 axialForce\n');
fprintf(f,'recorder Element -file Brace_deform_27.txt -ele 27 deformations\n');

fprintf(f,'recorder Element -file Brace_axialF_29.txt -ele 29 axialForce\n');
fprintf(f,'recorder Element -file Brace_deform_29.txt -ele 29 deformations\n');

fprintf(f,'recorder Element -file Brace_axialF_31.txt -ele 31 axialForce\n');
fprintf(f,'recorder Element -file Brace_deform_31.txt -ele 31 deformations\n');

fprintf(f,'recorder Element -file Brace_axialF_33.txt -ele 33 axialForce\n');
fprintf(f,'recorder Element -file Brace_deform_33.txt -ele 33 deformations\n');

fprintf(f,'recorder Element -file Brace_axialF_35.txt -ele 35 axialForce\n');
fprintf(f,'recorder Element -file Brace_deform_35.txt -ele 35 deformations\n');

fprintf(f,'recorder Element -file Brace_axialF_37.txt -ele 37 axialForce\n');
fprintf(f,'recorder Element -file Brace_deform_37.txt -ele 37 deformations\n');

% To record forces in HBEs and CBs (global coordinates)
% HBEs
% Forces
fprintf(f,'recorder Element -file HBE_F_1.txt -time -ele 1 force\n');
fprintf(f,'recorder Element -file HBE_F_2.txt -time -ele 2 force\n');
fprintf(f,'recorder Element -file HBE_F_3.txt -time -ele 3 force\n');
fprintf(f,'recorder Element -file HBE_F_4.txt -time -ele 4 force\n');
% CBs
```

```
% Forces
fprintf(f,'recorder Element -file CB_F_5.txt -time -ele 5 force\n');
fprintf(f,'recorder Element -file CB_F_6.txt -time -ele 6 force\n');


% To record VBE element forces (Fel# = forces in element #) (In global
% coordinates)
% Pier 1 EVBE
fprintf(f,'recorder Element -file P1EVBE_Fel7.txt -time -ele 7 force\n');
fprintf(f,'recorder Element -file P1EVBE_Fel8.txt -time -ele 8 force\n');
fprintf(f,'recorder Element -file P1EVBE_Fel9.txt -time -ele 9 force\n');
fprintf(f,'recorder Element -file P1EVBE_Fel10.txt -time -ele 10 force\n');
fprintf(f,'recorder Element -file P1EVBE_Fel11.txt -time -ele 11 force\n');

% Pier 1 IVBE
fprintf(f,'recorder Element -file P1IVBE_Fel12.txt -time -ele 12 force\n');
fprintf(f,'recorder Element -file P1IVBE_Fel13.txt -time -ele 13 force\n');
fprintf(f,'recorder Element -file P1IVBE_Fel14.txt -time -ele 14 force\n');
fprintf(f,'recorder Element -file P1IVBE_Fel15.txt -time -ele 15 force\n');
fprintf(f,'recorder Element -file P1IVBE_Fel16.txt -time -ele 16 force\n');

% Pier 2 IVBE
fprintf(f,'recorder Element -file P2IVBE_Fel17.txt -time -ele 17 force\n');
fprintf(f,'recorder Element -file P2IVBE_Fel18.txt -time -ele 18 force\n');
fprintf(f,'recorder Element -file P2IVBE_Fel19.txt -time -ele 19 force\n');
fprintf(f,'recorder Element -file P2IVBE_Fel20.txt -time -ele 20 force\n');
fprintf(f,'recorder Element -file P2IVBE_Fel21.txt -time -ele 21 force\n');

% Pier 2 EVBE
fprintf(f,'recorder Element -file P2EVBE_Fel22.txt -time -ele 22 force\n');
fprintf(f,'recorder Element -file P2EVBE_Fel23.txt -time -ele 23 force\n');
fprintf(f,'recorder Element -file P2EVBE_Fel24.txt -time -ele 24 force\n');
fprintf(f,'recorder Element -file P2EVBE_Fel25.txt -time -ele 25 force\n');
fprintf(f,'recorder Element -file P2EVBE_Fel26.txt -time -ele 26 force\n');

% DRIFT RECORDERS
% recorder Drift <-file $fileName> <-xml $fileName> <-time> -iNode $inode1 $inode2 ... -
jNode $jnode1 $jnode2 ... -dof $dof1 $dof2 ... -perpDirn $perpDirn1 $perpDirn2 ...
fprintf(f,'recorder Drift -file P1_EVBE_S1.txt -time -iNode 1 -jNode 9 -dof 1 -perpDirn 2\n');
fprintf(f,'recorder Drift -file P1_EVBE_S2.txt -time -iNode 9 -jNode 13 -dof 1 -perpDirn 2\n');
fprintf(f,'recorder Drift -file P1_EVBE_S3.txt -time -iNode 13 -jNode 21 -dof 1 -perpDirn 2\n');
fprintf(f,'recorder Drift -file P1_IVBE_S1.txt -time -iNode 2 -jNode 10 -dof 1 -perpDirn 2\n');
fprintf(f,'recorder Drift -file P1_IVBE_S2.txt -time -iNode 10 -jNode 14 -dof 1 -perpDirn 2\n');
fprintf(f,'recorder Drift -file P1_IVBE_S3.txt -time -iNode 14 -jNode 22 -dof 1 -perpDirn 2\n');

fprintf(f,'recorder Drift -file P2_EVBE_S1.txt -time -iNode 4 -jNode 12 -dof 1 -perpDirn 2\n');
```

```
fprintf(f,'recorder Drift -file P2_EVBE_S2.txt -time -iNode 12 -jNode 16 -dof 1 -perpDirn 2\n');
fprintf(f,'recorder Drift -file P2_EVBE_S3.txt -time -iNode 16 -jNode 24 -dof 1 -perpDirn 2\n');
fprintf(f,'recorder Drift -file P2_IVBE_S1.txt -time -iNode 3 -jNode 11 -dof 1 -perpDirn 2\n');
fprintf(f,'recorder Drift -file P2_IVBE_S2.txt -time -iNode 11 -jNode 15 -dof 1 -perpDirn 2\n');
fprintf(f,'recorder Drift -file P2_IVBE_S3.txt -time -iNode 15 -jNode 23 -dof 1 -perpDirn 2\n');

% To record moment and curvature at end sections of HBEs and CBs
% HBEs
fprintf(f,'recorder Element -file HBE_M1L.txt -time -ele 1 section 1 forces\n');
fprintf(f,'recorder Element -file HBE_curv1L.txt -time -ele 1 section 1 deformations\n');
fprintf(f,'recorder Element -file HBE_M1R.txt -time -ele 1 section 5 forces\n');
fprintf(f,'recorder Element -file HBE_curv1R.txt -time -ele 1 section 5 deformations\n');

fprintf(f,'recorder Element -file HBE_M2L.txt -time -ele 2 section 1 forces\n');
fprintf(f,'recorder Element -file HBE_curv2L.txt -time -ele 2 section 1 deformations\n');
fprintf(f,'recorder Element -file HBE_M2R.txt -time -ele 2 section 5 forces\n');
fprintf(f,'recorder Element -file HBE_curv2R.txt -time -ele 2 section 5 deformations\n');

fprintf(f,'recorder Element -file HBE_M3L.txt -time -ele 3 section 1 forces\n');
fprintf(f,'recorder Element -file HBE_curv3L.txt -time -ele 3 section 1 deformations\n');
fprintf(f,'recorder Element -file HBE_M3R.txt -time -ele 3 section 5 forces\n');
fprintf(f,'recorder Element -file HBE_curv3R.txt -time -ele 3 section 5 deformations\n');

fprintf(f,'recorder Element -file HBE_M4L.txt -time -ele 4 section 1 forces\n');
fprintf(f,'recorder Element -file HBE_curv4L.txt -time -ele 4 section 1 deformations\n');
fprintf(f,'recorder Element -file HBE_M4R.txt -time -ele 4 section 5 forces\n');
fprintf(f,'recorder Element -file HBE_curv4R.txt -time -ele 4 section 5 deformations\n');

% CBs
fprintf(f,'recorder Element -file CB_M5L.txt -time -ele 5 section 1 forces\n');
fprintf(f,'recorder Element -file CB_curv5L.txt -time -ele 5 section 1 deformations\n');
fprintf(f,'recorder Element -file CB_M5R.txt -time -ele 5 section 5 forces\n');
fprintf(f,'recorder Element -file CB_curv5R.txt -time -ele 5 section 5 deformations\n');

fprintf(f,'recorder Element -file CB_M6L.txt -time -ele 6 section 1 forces\n');
fprintf(f,'recorder Element -file CB_curv6L.txt -time -ele 6 section 1 deformations\n');
fprintf(f,'recorder Element -file CB_M6R.txt -time -ele 6 section 5 forces\n');
fprintf(f,'recorder Element -file CB_curv6R.txt -time -ele 6 section 5 deformations\n');

%% Applied lateral load
% Define Time Series
fprintf(f,'timeSeries Linear 2\n');

% Load applied at nodes 25 and 26 in the x-direction
fprintf(f,'pattern Plain 2 2 {\n');
fprintf(f,'load 25 1.0 0.0 0.0\n');
```

```
fprintf(f,'load 26 1.0 0.0 0.0\n');
fprintf(f,'}\n');

fprintf(f,'puts "Pushover Analysis"\n');

% Pushover Analysis commands
% -------------------
% Constraints command
fprintf(f,'constraints Plain\n');

% Numberer command
fprintf(f,'numberer RCM\n');

% System command
fprintf(f,'system ProfileSPD\n');

% Test command
fprintf(f,'test EnergyIncr 1e-5 20 1\n');

% Algorithm command
fprintf(f,'algorithm NewtonLineSearch\n');

% Integrator command
%  Eigen command - A total displacment of 2 in. is applied, so 20 steps are
%  required
fprintf(f,'integrator DisplacementControl 25 1 0.1\n');
fprintf(f,'analyze 20\n');

% Analysis command
fprintf(f,'analysis Static\n');

fprintf(f,'wipe all\n');

fclose(f);

%%Run OpenSees
!OpenSees SmallScaleOS.tcl

%%Output files%%
disp = dlmread('DispSmall.txt');
react = dlmread('RexnSmall.txt');

% Braces
Brace_axialF_27 = dlmread('Brace_axialF_27.txt');
Brace_deform_27 = dlmread('Brace_deform_27.txt');
Brace_axialF_29 = dlmread('Brace_axialF_29.txt');
```

```
Brace_deform_29 = dlmread('Brace_deform_29.txt');
Brace_axialF_31 = dlmread('Brace_axialF_31.txt');
Brace_deform_31 = dlmread('Brace_deform_31.txt');
Brace_axialF_33 = dlmread('Brace_axialF_33.txt');
Brace_deform_33 = dlmread('Brace_deform_33.txt');
Brace_axialF_35 = dlmread('Brace_axialF_35.txt');
Brace_deform_35 = dlmread('Brace_deform_35.txt');
Brace_axialF_37 = dlmread('Brace_axialF_37.txt');
Brace_deform_37 = dlmread('Brace_deform_37.txt');

% Stress-Strain in HBEs and CBs
stress_strain_HBE_1_1 = dlmread('stress_strain_HBE_1_1.txt');
stress_strain_HBE_1_5 = dlmread('stress_strain_HBE_1_5.txt');
stress_strain_HBE_2_1 = dlmread('stress_strain_HBE_2_1.txt');
stress_strain_HBE_2_5 = dlmread('stress_strain_HBE_2_5.txt');
stress_strain_HBE_3_1 = dlmread('stress_strain_HBE_3_1.txt');
stress_strain_HBE_3_5 = dlmread('stress_strain_HBE_1_5.txt');
stress_strain_HBE_4_1 = dlmread('stress_strain_HBE_4_1.txt');
stress_strain_HBE_4_5 = dlmread('stress_strain_HBE_4_5.txt');

stress_strain_CB_5_1 = dlmread('stress_strain_CB_5_1.txt');
stress_strain_CB_5_5 = dlmread('stress_strain_CB_5_5.txt');
stress_strain_CB_6_1 = dlmread('stress_strain_CB_6_1.txt');
stress_strain_CB_6_5 = dlmread('stress_strain_CB_6_5.txt');

% Plastic deformation and rotation in the HBEs and CBs
% HBEs
plasticdeform_HBE_1 = dlmread('plasticdeform_HBE_1.txt');
plasticdeform_HBE_2 = dlmread('plasticdeform_HBE_2.txt');
plasticdeform_HBE_3 = dlmread('plasticdeform_HBE_3.txt');
plasticdeform_HBE_4 = dlmread('plasticdeform_HBE_4.txt');
% CBs
plasticdeform_CB_5 = dlmread('plasticdeform_CB_5.txt');
plasticdeform_CB_6 = dlmread('plasticdeform_CB_6.txt');


% HBE ELEMENT Forces

HBE_F_1 = dlmread('HBE_F_1.txt');
HBE_F_2 = dlmread('HBE_F_2.txt');
HBE_F_3 = dlmread('HBE_F_3.txt');
HBE_F_4 = dlmread('HBE_F_4.txt');


% CB ELEMENT FORCES
```

```
CB_F_5 = dlmread('CB_F_5.txt');
CB_F_6 = dlmread('CB_F_6.txt');

% HBE Section Information
HBE_M1L = dlmread('HBE_M1L.txt');
HBE_curv1L = dlmread('HBE_curv1L.txt');
HBE_M1R = dlmread('HBE_M1R.txt');
HBE_curv1R = dlmread('HBE_curv1R.txt');

HBE_M2L = dlmread('HBE_M2L.txt');
HBE_curv2L = dlmread('HBE_curv2L.txt');
HBE_M2R = dlmread('HBE_M2R.txt');
HBE_curv2R = dlmread('HBE_curv2R.txt');

HBE_M3L = dlmread('HBE_M3L.txt');
HBE_curv3L = dlmread('HBE_curv3L.txt');
HBE_M3R = dlmread('HBE_M3R.txt');
HBE_curv3R = dlmread('HBE_curv3R.txt');

HBE_M4L = dlmread('HBE_M4L.txt');
HBE_curv4L = dlmread('HBE_curv4L.txt');
HBE_M4R = dlmread('HBE_M4R.txt');
HBE_curv4R = dlmread('HBE_curv4R.txt');

% CB Section Information
CB_M5L = dlmread('CB_M5L.txt');
CB_curv5L = dlmread('CB_curv5L.txt');
CB_M5R = dlmread('CB_M5R.txt');
CB_curv5R = dlmread('CB_curv5R.txt');

CB_M6L = dlmread('CB_M6L.txt');
CB_curv6L = dlmread('CB_curv6L.txt');
CB_M6R = dlmread('CB_M6R.txt');
CB_curv6R = dlmread('CB_curv6R.txt');

% VBE element forces in global coordinates
P1EVBE_Fel7 = dlmread('P1EVBE_Fel7.txt');
P1EVBE_Fel8 = dlmread('P1EVBE_Fel8.txt');
P1EVBE_Fel9 = dlmread('P1EVBE_Fel9.txt');
P1EVBE_Fel10 = dlmread('P1EVBE_Fel10.txt');
P1EVBE_Fel11 = dlmread('P1EVBE_Fel11.txt');

P1IVBE_Fel12 = dlmread('P1IVBE_Fel12.txt');
P1IVBE_Fel13 = dlmread('P1IVBE_Fel13.txt');
P1IVBE_Fel14 = dlmread('P1IVBE_Fel14.txt');
P1IVBE_Fel15 = dlmread('P1IVBE_Fel15.txt');
```

```
P1IVBE_Fel16 = dlmread('P1IVBE_Fel16.txt');

P2IVBE_Fel17 = dlmread('P2IVBE_Fel17.txt');
P2IVBE_Fel18 = dlmread('P2IVBE_Fel18.txt');
P2IVBE_Fel19 = dlmread('P2IVBE_Fel19.txt');
P2IVBE_Fel20 = dlmread('P2IVBE_Fel20.txt');
P2IVBE_Fel21 = dlmread('P2IVBE_Fel21.txt');

P2EVBE_Fel22 = dlmread('P2EVBE_Fel22.txt');
P2EVBE_Fel23 = dlmread('P2EVBE_Fel23.txt');
P2EVBE_Fel24 = dlmread('P2EVBE_Fel24.txt');
P2EVBE_Fel25 = dlmread('P2EVBE_Fel25.txt');
P2EVBE_Fel26 = dlmread('P2EVBE_Fel26.txt');

% DRIFT RECORDER OUTPUT
P1_EVBE_S1 = dlmread('P1_EVBE_S1.txt');
P1_EVBE_S2 = dlmread('P1_EVBE_S2.txt');
P1_EVBE_S3 = dlmread('P1_EVBE_S3.txt');
P1_IVBE_S1 = dlmread('P1_IVBE_S1.txt');
P1_IVBE_S2 = dlmread('P1_IVBE_S2.txt');
P1_IVBE_S3 = dlmread('P1_IVBE_S3.txt');

P2_EVBE_S1 = dlmread('P2_EVBE_S1.txt');
P2_EVBE_S2 = dlmread('P2_EVBE_S2.txt');
P2_EVBE_S3 = dlmread('P2_EVBE_S3.txt');
P2_IVBE_S1 = dlmread('P2_IVBE_S1.txt');
P2_IVBE_S2 = dlmread('P2_IVBE_S2.txt');
P2_IVBE_S3 = dlmread('P2_IVBE_S3.txt');


%% Post Processing
ReactX = [react(:,1), react(:,2)+react(:,5)+react(:,8)+react(:,11)]; %1st column is time, 2nd
column is total base shear

%% Plot push-over curve
figure(); clf;
plot(disp(:,2), -ReactX(:,2),'LineWidth',2);
title('Pushover Analysis of Small-Scale SPSW-WC')
xlabel('Top Lateral Displacement (in.)');
ylabel('Base Shear (kips)');

%% Plot F-deformation for braces
Fy_calc = (zeros(20,1)+1.62)/(.06*.5);

BD27 = Brace_deform_27(:,1)/15.31;
BF27 = Brace_axialF_27(:,1)/(.5*.06);
```

```
figure();
subplot(3,2,1);
plot(BD27, BF27,BD27,Fy_calc,'--','LineWidth',2)
title('Stress-Strain (Brace - Pier 1, First Story)');
xlabel('Strain (in./in.)');
ylabel('Stress (ksi)');
legend('OpenSees','Fy=54 ksi','Location','SouthEast');
ylim([40 55]);


BD29 = Brace_deform_29(:,1)/15.31;
BF29 = Brace_axialF_29(:,1)/(.5*.06);
subplot(3,2,2);
plot(BD29, BF29,BD29,Fy_calc,'--','LineWidth',2)
title('Stress-Strain (Brace - Pier 2, First Story)');
xlabel('Strain (in./in.)');
ylabel('Stress (ksi)');
legend('OpenSees','Fy=54 ksi','Location','SouthEast');
ylim([40 55]);


BD31 = Brace_deform_31(:,1)/13.45;
BF31 = Brace_axialF_31(:,1)/(.5*.06);
subplot(3,2,3);
plot(BD31, BF31,BD31,Fy_calc,'--','LineWidth',2)
title('Stress-Strain (Brace - Pier 1, Second Story)');
xlabel('Strain (in./in.)');
ylabel('Stress (ksi)');
legend('OpenSees','Fy=54 ksi','Location','SouthEast');
ylim([46 55]);


BD33 = Brace_deform_33(:,1)/13.45;
BF33 = Brace_axialF_33(:,1)/(.5*.06);
subplot(3,2,4);
plot(BD33, BF33,BD33,Fy_calc,'--','LineWidth',2)
title('Stress-Strain (Brace - Pier 2, Second Story)');
xlabel('Strain (in./in.)');
ylabel('Stress (ksi)');
legend('OpenSees','Fy=54 ksi','Location','SouthEast');
ylim([46 55]);


BD35 = Brace_deform_35(:,1)/12.5;
BF35 = Brace_axialF_35(:,1)/(.5*.06);
subplot(3,2,5);
```

```
plot(BD35, BF35,BD35,Fy_calc,'--','LineWidth',2)
title('Stress-Strain (Brace - Pier 1, Third Story)');
xlabel('Strain (in./in.)');
ylabel('Stress (ksi)');
legend('OpenSees','Fy=54 ksi','Location','SouthEast');
ylim([32 55]);

BD37 = Brace_deform_37(:,1)/12.5;
BF37 = Brace_axialF_37(:,1)/(.5*.06);
subplot(3,2,6);
plot(BD37, BF37,BD37,Fy_calc,'--','LineWidth',2)
title('Stress-Strain (Brace - Pier 2, Third Story)');
xlabel('Strain (in./in.)');
ylabel('Stress (ksi)');
legend('OpenSees','Fy=54 ksi','Location','SouthEast');
ylim([32 55]);


%% Plot M-curvature for HBEs
% First want to plot calculated Mp
Mp_calc = zeros(20,1)+1.21;

figure();
subplot(4,2,1);
plot(-HBE_curv1L(:,2), HBE_M1L(:,3), -HBE_curv1L(:,2), Mp_calc ,'--','LineWidth',2);
title('Moment-Curvature, HBE 1, Left');
xlabel('Curvature (1/in.)');
ylabel('Moment (k-in)');
legend('OpenSees','Mp','Location','SouthEast');
subplot(4,2,2);
plot(-HBE_curv1R(:,2), -HBE_M1R(:,3),-HBE_curv1R(:,2),Mp_calc,'--', 'LineWidth',2);
title('Moment-Curvature, HBE 1, Right');
xlabel('Curvature (1/in.)');
ylabel('Moment (k-in)');
legend('OpenSees','Mp','Location','SouthEast');
subplot(4,2,3);
plot(-HBE_curv2L(:,2), HBE_M2L(:,3),-HBE_curv2L(:,2),Mp_calc,'--','LineWidth',2);
title('Moment-Curvature, HBE 2, Left');
xlabel('Curvature (1/in.)');
ylabel('Moment (k-in)');
legend('OpenSees','Mp','Location','SouthEast');
subplot(4,2,4);
plot(-HBE_curv2R(:,2), -HBE_M2R(:,3),-HBE_curv2R(:,2),Mp_calc,'--','LineWidth',2);
title('Moment-Curvature, HBE 2, Right');
xlabel('Curvature (1/in.)');
ylabel('Moment (k-in)');
```

```
legend('OpenSees','Mp','Location','SouthEast');
subplot(4,2,5);
plot(-HBE_curv3L(:,2), HBE_M3L(:,3),-HBE_curv3L(:,2),Mp_calc,'--','LineWidth',2);
title('Moment-Curvature, HBE 3, Left');
xlabel('Curvature (1/in.)');
ylabel('Moment (k-in)');
legend('OpenSees','Mp','Location','SouthEast');
subplot(4,2,6);
plot(-HBE_curv3R(:,2), -HBE_M3R(:,3),-HBE_curv3R(:,2),Mp_calc,'--','LineWidth',2);
title('Moment-Curvature, HBE 3, Right');
xlabel('Curvature (1/in.)');
ylabel('Moment (k-in)');
legend('OpenSees','Mp','Location','SouthEast');
subplot(4,2,7);
plot(-HBE_curv4L(:,2), HBE_M4L(:,3),-HBE_curv4L(:,2),Mp_calc,'--','LineWidth',2);
title('Moment-Curvature, HBE 4, Left');
xlabel('Curvature (1/in.)');
ylabel('Moment (k-in)');
legend('OpenSees','Mp','Location','SouthEast');
subplot(4,2,8);
plot(-HBE_curv4R(:,2), -HBE_M4R(:,3),-HBE_curv4R(:,2),Mp_calc,'--','LineWidth',2);
title('Moment-Curvature, HBE 4, Right');
xlabel('Curvature (1/in.)');
ylabel('Moment (k-in)');
legend('OpenSees','Mp','Location','SouthEast');

%% Plot M-curvature for CBs
figure();

subplot(2,2,1);
plot(CB_curv5L(:,2), CB_M5L(:,3),CB_curv5L(:,2),Mp_calc,'--','LineWidth',2);
title('Moment-Curvature, CB 5, Left');
xlabel('Curvature (1/in.)');
ylabel('Moment (k-in)');
legend('OpenSees','Mp','Location','SouthEast');
subplot(2,2,2);
plot(CB_curv5R(:,2), -CB_M5R(:,3),CB_curv5R(:,2),Mp_calc,'--','LineWidth',2);
title('Moment-Curvature, CB 5, Right');
xlabel('Curvature (1/in.)');
ylabel('Moment (k-in)');
legend('OpenSees','Mp','Location','SouthEast');
subplot(2,2,3);
plot(CB_curv6L(:,2), CB_M6L(:,3),CB_curv6L(:,2),Mp_calc,'--','LineWidth',2);
title('Moment-Curvature, CB 6, Left');
xlabel('Curvature (1/in.)');
ylabel('Moment (k-in)');
```

```
legend('OpenSees','Mp','Location','SouthEast');
xlim([0 15e-4]);
subplot(2,2,4);
plot(CB_curv6R(:,2), -CB_M6R(:,3),CB_curv6R(:,2),Mp_calc,'--','LineWidth',2);
title('Moment-Curvature, CB 6, Right');
xlabel('Curvature (1/in.)');
ylabel('Moment (k-in)');
legend('OpenSees','Mp','Location','SouthEast');
xlim([0 15e-4]);
```

APPENDIX E
SPECIMEN INSTRUMENTATION PLAN

E.1 Instrumentation Plan

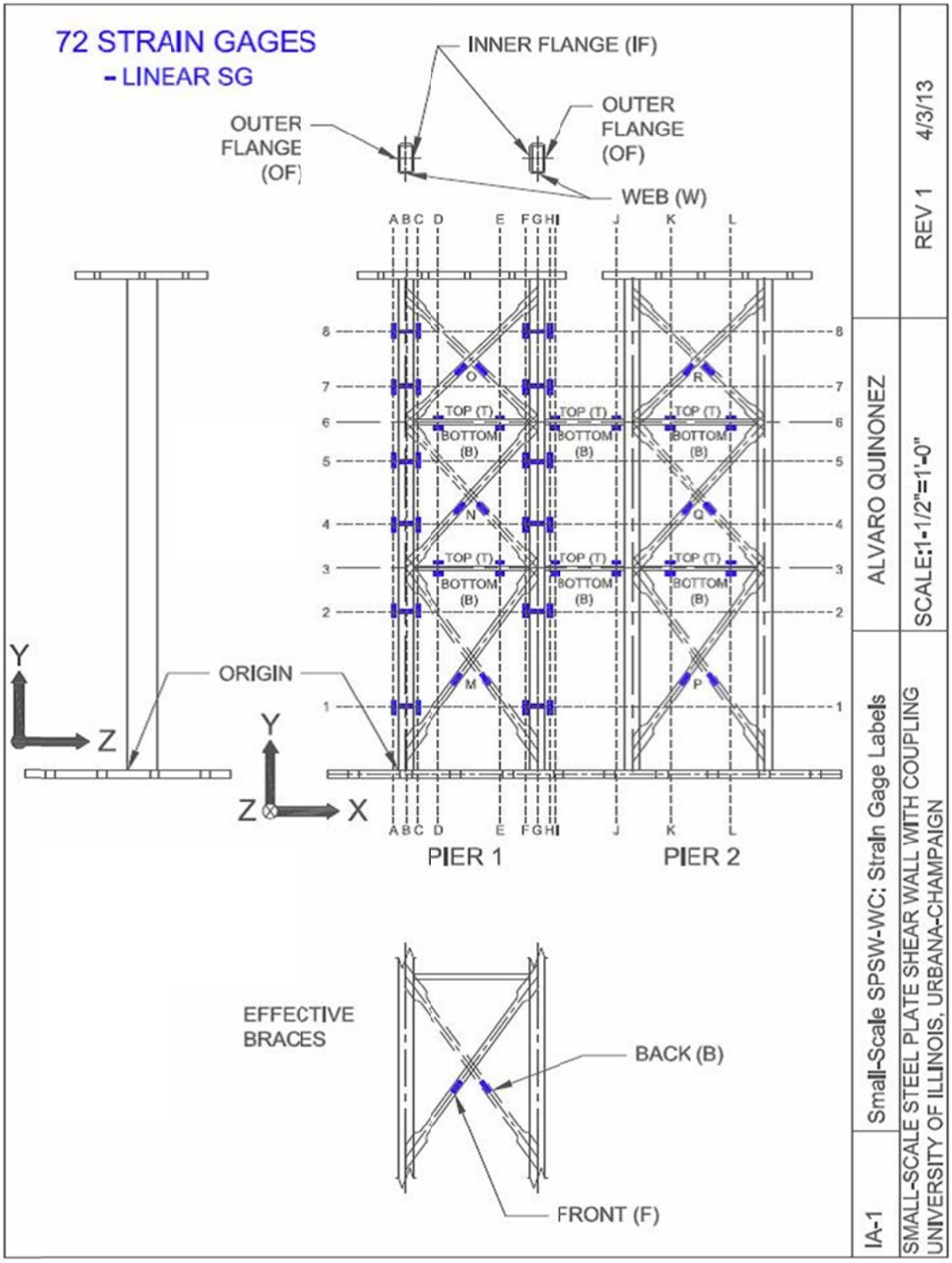

E.2 Strain Gage Information

General Location	Quick Label	Channel Name	Initial Coordinates (Origin at Back Left Corner at Base of Pier 1 EVBE)		
			x (in.)	y (in.)	z (in.)
Pier 1	A1	SG_EVBE-OF_F1_A1	0	4.5625	1.1875
	A2	SG_EVBE-OF_F1_A2	0	10.875	1
	A4	SG_EVBE-OF_F2_A4	0	16.9375	0.9375
	A5	SG_EVBE-OF_F2_A5	0	21.125	1
	A7	SG_EVBE-OF_F3_A7	0	26.3125	0.9375
	A8	SG_EVBE-OF_F3_A8	0	30.125	0.9375
	B1	SG_EVBE-W_F1_B1	0.5625	4.4375	2
	B2	SG_EVBE-W_F1_B2	0.5	10.875	2
	B4	SG_EVBE-W_F2_B4	0.5	16.8125	2
	B5	SG_EVBE-W_F2_B5	0.625	21.125	2
	B7	SG_EVBE-W_F3_B7	0.4375	26.375	2
	B8	SG_EVBE-W_F3_B8	0.5625	30	2
	C1	SG_EVBE-IF_F1_C1	1	4.4375	1
	C2	SG_EVBE-IF_F1_C2	1	10.5625	1.1875
	C4	SG_EVBE-IF_F2_C4	1	16.9375	1
	C5	SG_EVBE-IF_F2_C5	1	21.0625	0.9375
	C7	SG_EVBE-IF_F3_C7	1	26.25	1
	C8	SG_EVBE-IF_F3_C8	1	29.9375	0.9375
	D3T	SG_HBE_F2_D3T	3.125	14.1875	1.25
	D3B	SG_HBE_F2_D3B	2.625	13.9375	1.1875
	D6T	SG_HBE_F3_D6T	2.8125	24.1875	1.0625
	D6B	SG_HBE_F3_D6B	2.75	23.9375	1.125
	E3T	SG_HBE_F2_E3T	7.4375	14.1875	1.1875
	E3B	SG_HBE_F2_E3B	7.3125	13.9375	1.1875
	E6T	SG_HBE_F3_E6T	7.1875	24.1875	1.0625
	E6B	SG_HBE_F3_E6B	7.25	23.875	1.125
	F1	SG_IVBE-IF_F1_F1	9	4.375	0.9375
	F2	SG_IVBE-IF_F1_F2	9	10.75	0.875
	F4	SG_IVBE-IF_F2_F4	9	16.8125	0.875
	F5	SG_IVBE-IF_F2_F5	9	21.0625	1.0625
	F7	SG_IVBE-IF_F3_F7	9	26.1875	0.875
	F8	SG_IVBE-IF_F3_F8	9	30	0.9375
	G1	SG_IVBE-W_F1_G1	9.5625	4.4375	2
	G2	SG_IVBE-W_F1_G2	9.5625	10.875	2

General Location	Quick Label	Channel Name	Initial Coordinates (Origin at Back Left Corner at Base of Pier 1 EVBE)		
			x (in.)	y (in.)	z (in.)
Pier 1	G4	SG_IVBE-W_F2_G4	9.5625	17.125	2
	G5	SG_IVBE-W_F2_G5	9.5	21.125	2
	G7	SG_IVBE-W_F3_G7	9.5	26.375	2
	G8	SG_IVBE-W_F3_G8	9.4375	29.9375	2
	H1	SG_IVBE-OF_F1_H1	10	4.5625	1.0625
	H2	SG_IVBE-OF_F1_H2	10	10.875	1.0625
	H4	SG_IVBE-OF_F2_H4	10	16.625	1.0625
	H5	SG_IVBE-OF_F2_H5	10	21.125	0.9375
	H7	SG_IVBE-OF_F3_H7	10	26.375	1.0625
	H8	SG_IVBE-OF_F3_H8	10	29.5625	1.125
Coupling Beams	I3T	SG_CB_F2_I3T	11.375	14.1875	1.1875
	I3B	SG_CB_F2_I3B	11.5	13.9375	1.0625
	I6T	SG_CB_F3_I6T	11.4375	24.1875	1.0625
	I6B	SG_CB_F3_I6B	11.5	23.9375	1.0625
	J3T	SG_CB_F2_J3T	14	14.1875	1.0625
	J3B	SG_CB_F2_J3B	14.125	13.9375	1
	J6T	SG_CB_F3_J6T	14	24.1875	1.0625
	J6B	SG_CB_F3_J6B	14.0625	23.9375	1.0625
Pier 2	K3T	SG_HBE_F2_K3T	18.1875	14.1875	1
	K3B	SG_HBE_F2_K3B	18.375	13.9375	1
	K6T	SG_HBE_F3_K6T	18.25	24.1875	1
	K6B	SG_HBE_F3_K6B	18.3125	23.875	1.125
	L3T	SG_HBE_F2_L3T	22.8125	14.1875	1
	L3B	SG_HBE_F2_L3B	22.6875	13.9375	1.1875
	L6T	SG_HBE_F3_L6T	22.6875	24.1875	1
	L6B	SG_HBE_F3_L6B	22.6875	23.9375	1.0625
Effective Braces - Pier 1	MF	SG_DB_F1_MF	5.375	8.125	2
	MB	SG_DB_F1_MB	5.125	7.625	0
	NF	SG_DB_F2_NF	5.4375	19.625	2

General Location	Quick Label	Channel Name	Initial Coordinates (Origin at Back Left Corner at Base of Pier 1 EVBE)		
			x (in.)	y (in.)	z (in.)
Effective Braces - Pier 1	NB	SG_DB_F2_NB	5	19.0625	0
	OF	SG_DB_F3_OF	5.25	28.625	2
	OB	SG_DB_F3_OB	5	28.4375	0
Effective Braces - Pier 2	PF	SG_DB_F1_PF	20.8125	7.9375	2
	PB	SG_DB_F1_PB	20.5	7.875	0
	QF	SG_DB_F2_QF	20.6875	19.25	2
	QB	SG_DB_F2_QB	20.3125	19.3125	0
	RF	SG_DB_F3_RF	20.6875	28.625	2
	RB	SG_DB_F3_RB	20.4375	28.4375	0